Chapter 1 Introduction

1.1 General Background

With the tendency toward miniaturization of consumer electrical and optical products, nano-scaled solders for tiny bonding with enhanced and desired properties are required. Small size and low dimensionality in materials become the critical factors in defining their properties which are often unforeseen to bulk materials [1]. Thus, one-dimensional electric materials have attracted much interest and have been investigated extensively for their unique size effects [2]. Understanding the solidification behavior and the formation of nano-materials helps to recognize the mechanical properties of products and to gain expected ones through particular processes.

Numerous researchers have devoted to synthesize one-dimensional or dimensionless materials with their typical methods, such as chemical reduction, CVD, PVD, heating in chunks, mechanical alloying, and various template-assisted processes [3-15]. Following the achievement of our laboratory[12, 16-22], the vacuum hydraulic pressure injection method possesses the experience of metals and alloys casting processes, which has been studies and applied practically for several centuries. Unlike vapor deposition processes or chemosynthesis, when a stoichiometric bulk material was produced, the following casting would not change the composite ratio of alloys until the vacuum injection process ended. This stable, easy and efficient method is suitable for the fundamental researches.

In the history of the electronic industry, the lead-tin has been widely used throughout the electronic industry all the time due to its favorable physical and mechanical properties, and well-developed production process [23-28]. Nevertheless, concerns to the harm of Pb to the environment and human health [29] have reminded the electronic industry seeking lead-free solutions. Lots of efforts have been devoted to various tin-containing binary and ternary

lead-free alloys [29-34]. Among those substitution materials for Pb-based solders, the eutectic Bi43-Sn57 alloy was regarded as a potential one on fuse products and low temperature applications. Bi43-Sn57 alloy also performs some advantages [35, 36], such as its net eutectic texture, superior wettability, and almost void-free bonding [37, 38]; therefore, Bi-Sn system is always the popular topic no matter in solid or liquid phase from 1940s to the present.

In this study, the vacuum hydraulic pressure injection method [39] was utilized to fabricate the eutectic Bi-Sn alloy nanowires. A Bi-Sn eutectic bulk alloy is a lamellar structure; that is, the interfaces of two different phases are perpendicular to the solid/liquid interface and parallel to the growth direction [40]. As the Bi-Sn eutectic melt was injected into the AAO (Anodic Aluminum Oxide) nanochannels, the lamellar microstructure forms along the wire axes in a confined space during the solidification process.

Hunt, an author of the JH model [41], reported that "in the physical sciences, the details of pattern formation are not well understood [42]." The observed solidification structures are never perfectly regular, and only a small range of spacing is always present on a directionally grown lamellar structure because of the fluctuation in growth conditions. This article has also attempted to present a model to explain a particular solidification condition during the injection process. To gather more information on the axial-arranged eutectic nanostructure, the re-melting and solidification procedures were investigated by in situ high-resolution transmission electron microscopy (TEM). The size effects including the differences in solidification and diffusion behaviors are investigated.

Finally, the eutectic Bi-Sn nanowires were applied to fabricate bismuth oxide-tin oxide (BiO_x-SnO_x) nanowires by directly being oxidized in an air furnace. The as-injected nanowires have a regular structure; thus, the BiO_x-SnO_x nanowires are simultaneously obtained through a thermal oxidation process; and retain the segmental microstructure. It is deserved to be mentioned that tin oxide (SnO_2) and bismuth oxide (Bi_2O_3) are two important strategic materials in modern solid-state technology. As semiconductors with large and wide

energy band gaps, they are widely applied to gas sensors [43, 44], optoelectronic devices [45, 46], photovoltaic cells [47, 48], and transparent conduction electrodes [49]. This practical methodology provides a simpler, cheaper, and more stable process for fabrication of one-dimensional functional nano-oxides.

1.2 Organization of the Dissertation

This dissertation is divided into seven chapters.

In chapter 2, the literatures are reviewed, including the properties of eutectic bismuth-tin alloy and nanowires, the fabrication methods of nanowires, the characteristics of AAO, fluid mechanics principles of melting alloys within nanowires, solidification of eutectic, and the features of one-dimensional bismuth oxide (Bi_2O_3) and tin oxide (SnO_2).

In chapter 3, for the first time this study reports the fabrication of nanowires using this eutectic Bi-43Sn solder material, and characterize the nanowire metallurgical microstructure as compared to the bulk sample in details. Eutectic Bi-43Sn (in weight percent) nanowires with diameters of 20 nm, 70 nm and 220 nm respectively, were fabricated by a hydraulic pressure injection process using anodic aluminum oxide (AAO) as templates. Novel eutectic microstructure was found within the fabricated nanowires, which composed of alternating Bi and Sn segments along their wire axes. Within the segments, the electron diffraction analysis revealed single crystalline structures of Bi and Sn elements respectively. Moreover, parameters that control the nanowire fabrication process were discussed. It was found that the as the wire diameter reduced, longer Bi and Sn segments formed.

In chapter 4, a model of solidification process was addressed to explain how the development of the microstructure occurred. A Bi-Sn eutectic nanowire of 200 nm diameter and several tens of μm in length is taken as an example. In addition, the distribution

coefficient and lever rule are also utilized to clarify this phenomenon differing greatly from bulk eutectic Bi-Sn alloy.

In chapter 5, this study reported the size effects on solidification and the formation mechanism of the segmented eutectic Bi-43Sn nanowires during in situ reheating. A model to explain a particular solidification condition during the injection process has also been presented. Understanding the solidification behavior and the formation of alloys can help us to recognize the mechanical properties of cast products and to gain the expected properties through particular processes. Furthermore, to gather more information on the axial-arranged eutectic nanostructure, the re-melting and solidification procedures were investigated by *in situ* high-resolution transmission electron microscopy (TEM). The size effects including the differences in solidification and diffusion behaviors are investigated.

In chapter 6, an application of above-mentioned one-dimensional Bi-Sn eutectic nanowires was presented. The BiO_x-SnO_x nanowires were fabricated by directly oxidizing Bi-Sn eutectic nanowires in an air furnace. As-injected nanowires have a regular structure; thus, the BiO_x-SnO_x nanowires are obtained by a thermal oxidation process to retain their segmental microstructure. The optical properties are evaluated to derive evidence of the existence of both oxides.

Finally, a summary of the results in this dissertation is given in chapter 7.

References

[1] A.P. Alivisatos, *Science* **1996**, 271, 933.

[2] M. Law, J. Goldberger, P.D. Yang, *Annu. Rev. Mater. Res.* **2004**, 34, 83.

[3] Z.B. Zhang, J.Y. Ying, M.S. Dresselhaus, *J. Mater. Res.* **1998**, 13, 1745.

[4] S.B. Cronin, Y.M. Lin, O. Rabin, M.R. Black, G. Dresselhaus, M.S. Dresselhaus, P.L. Gai, *Microsc. Microanaly.* **2002**, 8, 58.

[5] J.G. Wen, J.Y. Lao, D.Z. Wang, T.M. Kyaw, Y.L. Foo, Z.F. Ren, *Chem. Phys. Lett.* **2003**, 372, 717.

[6] Y.J. Zhang, H. Ago, J. Liu, M. Yumura, K. Uchida, S. Ohshima, S. Iijima, J. Zhu, X.Z. Zhang, *J. Crystal Growth* **2004**, 264, 363.

[7] S.T. Kao, J.G. Duh, *J Electron Mater.* **2004**, 33, 1445.

[8] L.Y. Hsiao, J.G Duh, *J. Electrochem. Soc.* **2005**, 152, J105.

[9] W. Zhang, Z.Q. Liu, K. Furuya, *Nanotechnology* **2008**, 19, 135302.

[10] N.I. Kovtyukhov, B.R. Martin, *Mater. Sci. Eng. C* **2002**, 19, 255.

[11] Z. Zhibo, Y.Y. Jackie, *J. Mater. Res.* **1998**, 13, 1745.

[12] C.C. Chen, C.G. Kuo, J.H. Chen, C.G. Chao, *Jpn. J. Appl. Phys.* **2004**, 43, 8354.

[13] J.W. Elam, D. Routkevitch, P.P. Mardilovich, S.M. George, *Chem. Mater.* **2003**, 15, 3507.

[14] C.A. Huber, T.E. Huber, M. Sadoqi, J.A. Lubin, S. Manalis, C.B. Prater, *Science* **1994**, 263, 800.

[15] A.B.F. Martinson, J.W. Elam, J. Liu, M.J. Pellin, T.J. Marks, J.T. Hupp, *Nano Lett.* **2008**, 8, 2862.

[16] C.C. Chen, C.G. Kuo, J.H. Chen, C.G. Chao, *Jpn. J. of Appl. Phys.* **2004**, 43, 8354.

[17] C.C. Chen, Y. Bisrat, Z.P. Luo, R.E. Schaak, C.G. Chao, D.C. Lagoudas, *Nanotechnology* **2006**, 17, 367.

[18] C.C. Chen, C.G. Kuo, C.G. Chao, *Jpn. J. Appl. Phys.* **2005**, 44, 1524.

[19] J.H. Chen, C.G. Chao, J.C. Ou, T.F. Liu, *Surface Science* **2007**, 601, 5142.

[20] J.H. Chen, S.C. Lo, C.G. Chao, T.F. Liu, *J. Nanosci. Nanotechnol.* **2008**, 8, 967.

[21] S.H. Chen, C.C. Chen, Z.P. Luo, C.G. Chao, *Materials Letters* **2009**, 63, 1165.

[22] S.H Chen, C.C. Chen, C.G. Chao, *Journal of Alloys and Compounds* **2009**, 481, 270.

[23] H.D. Soloman, *J. Electron. Packaging* **1989**, 111, 75.

[24] S. Knecht, L.R. Fox, *IEEE Trans. Comp., Hybrids, Manuf. Technol.* **1990**, 13, 424.

[25] Z. Mei, D. Grivas, M.C. Shine, J.W. Morris Jr., *J. Electron. Mater.* **1990**, 19, 1273.

[26] A.W. Worcester, J.T. O'Reilly, "*Metal Handbook 10th Edition*", Materials Park, Ohio: ASM International, **1990**, 2, 543.

[27] S. Jin, *JOM* **1993** (July), 13.

[28] S.S. Kang, A.K. Sarkhel, *J. Elec. Mater.* **1994**, 23**,** 701.

[29] J. Cannis, *Advanced Packaging* **2001**, 8, 33.
[30] S.K. Kang, *JOM* **2001**(June), 16.
[31] D.R. Frear, J.W. Jang, J.K. Lin, C. Zhang, *JOM* **2001**(June), 53, 28.
[32] F.W. Gayle, G. Becka, A. Syed, J. Badgett, G. Whitten, T.Y. Pan, A. Grusd, B. Bauer, R. Lathtop, J. Slattery, I. Anderson, J. Foley, A. Gickler, D. Napp, J. Mather, C. Oslon, *JOM* **2001**(June), 53, 17.
[33] M. Li, K.Y. Lee, D.R. Olsen, W.T. Chen, B.T.C. Tan, S. Mhaisalkar, *IEEE Trans. Electron. Packag. Manuf.* **2002**, 25, 185.
[34] Y.D. Jeon, S. Nieland, A. Ostman, H. Reichl, K.W. Paik, *J. Electron. Mater.* **2003**, 32, 1203.
[35] J.Y. Lao, J.G. Wen, Z.F. Ren, *Nano Lett.* **2002**, 2, 1287.
[36] D. Banerjee, J.Y. Lao, D.Z. Wang, J.Y. Huang, Z.F. Ren, D. Steeves, B. Kimball, M. Sennett, *Appl. Phys. Lett.* **2003**, 83, 2061.
[37] R.W. Chuang, C.C. Lee, *Thin Solid Film* **2002**, 414, 175.
[38] C.A. MacKay, W.D. Von Voss, *Mater. Sci. and Technol.* **1985**, 1, 240.
[39] C. Xu, G. Xu, Y. Liu, G. Wang, *Solid State Commun.* **2002**, 122, 175.
[40] W. Kurz, D.J. Fisher, "*Fundamentals of Solidification*", Trans Tech Publication, **1992**.
[41] K.A. Jackson, J.D. Hunt, *Trans. Met. Soc. AIME* **1996**, *236*, 1129.
[42] J.D. Hunt, *Science and Technology of Advanced Materials* **2001**, *2*,147.
[43] A. Khanna, R. Kumar, S.S. Bhatti, *Appl. Phys. Lett*. **2003**, 82, 4388.
[44] E. Kanazawa, G. Sakai, K. Shimanoe, Y. Kanmura, Y. Teraoka, N. Miura, N. Yamazoe, *Sensors Actuators B* **2001**, 77, 72.
[45] C. Tatsuyama,S. Ichimura, *Jpn. J. Appl. Phys.* **1976**,15, 843.
[46] L. Leontie, M. Caraman, A. Visinoiu, G.I. Rusu, *Thin Solid Films* **2005**, 473, 230.
[47] M. Turrion, J. Bisquert, P. Salvador, *J. Phys. Chem. B* **2003**, 107, 9397.
[48] J. George, B. Pradeep, K.S. Joseph, *Phys. Stat. Sol. (a)* **1987**, 100, 513.
[49] Y.S. He, J.C. Campbell, R.C. Murphy, M.F. Arendt, J.S. Swinnea, *J. Mater. Res.* **1993**, 8, 3131.

Chapter 2 Literature Review

2.1 Characteristics of Eutectic Bismuth-Tin (Bi-Sn) alloy

The major character of eutectic 57 wt% Bi-43 wt% Sn alloy is its low melting point, 139 ℃. In the second-level packing, any solders at the lower end of the temperature range should be advantageous in reducing processing cost [1]. The low processing temperature also allows more materials for low temperature performing well. As a low melting alloy Bi-Sn alloys are used in temperature overload devices and as solders in cases where the Pb-Sn solders are not suitable. In addition, the cost of bismuth is lower than the indium (In) element, even the melting point of Sn-In solder is only 120 ℃. Because of these advantages, Bi-Sn eutectic alloy is widely used in the electronic packing industry.

Figure 2.1 shows the phase diagram of Bi-Sn system. This system is a classic binary eutectic system and is a good example of a system which exhibits limited solid solubility and no intermediate compounds. At room temperature Sn will dissolve some of the Bi, but no Sn can be dissolved in Bi. The solubility of Bi in Sn will continue increasing to 21% as the temperature rises to the eutectic point. While the melting eutectic alloy solidifies, the excess Bi will be precipitated from Sn. The cooling rate influences only the grain sizes; that is, to hold the solidification at high temperature longer makes the grain size coarser, and doping Cu can restrain the coarsening phenomenon. In other words, a higher cooling rate results in a fine eutectic microstructure, which performs the better mechanic properties [3].

At room temperature, the eutectic Bi-Sn alloy, composed of the bct Sn (body-centered tetragonal, so-called β-Sn) and rhombohedral Bi, represents a lamellar microstructure, as shown in Fig. 2.2. The continuous and bright phase is rhombohedral Bi; moreover, rich-Sn phases present the dark and discontinuous regions. The volumetric ratio of β-Sn to Bi is about 49 to 51.

Unlike other metals, Bi increases 3.87% volume when solidifying, yet Sn shrinks slightly, which totally results in a 0.77% volumetric increase. Hare et al. [4] reported that the lattice constants of both Sn and Bi would rise as the aging time increased at the cooling rate of $50Ks^{-1}$. Another study shows that after a natural aging of 200 hours the lattice constant and hardness reach the maximum [5].

Adding Bi into solders improves the wettability but causes unnecessary reactions with the substrate and the copper. To increase the cooling rate would avoid or reduce that. In addition, the strain rates influence the mechanics properties of Bi-Sn series. A high strain rate causes the higher strength and the lower ductility; oppositely, the poor strength and the higher ductility result from a lower strain rate.

The important properties of eutectic Bi-Sn alloy are summarized as below:

1. Low melting point : 139 ℃ (Sn-37Pb : 183 ℃)
2. Volume expansion with solidifying : 0.77vol%
3. Low surface tension (good wettablility) : 319 N/m (Sn-37Pb : 417 N/m)
4. Low thermal expansion coefficient : 21 W/mK at 85 ℃
5. Low electronic resistance : 30-34.4 μΩ-cm (pure Bi = 115 μΩ-cm)
6. The mechanic properties are strongly influenced by the strain rate.

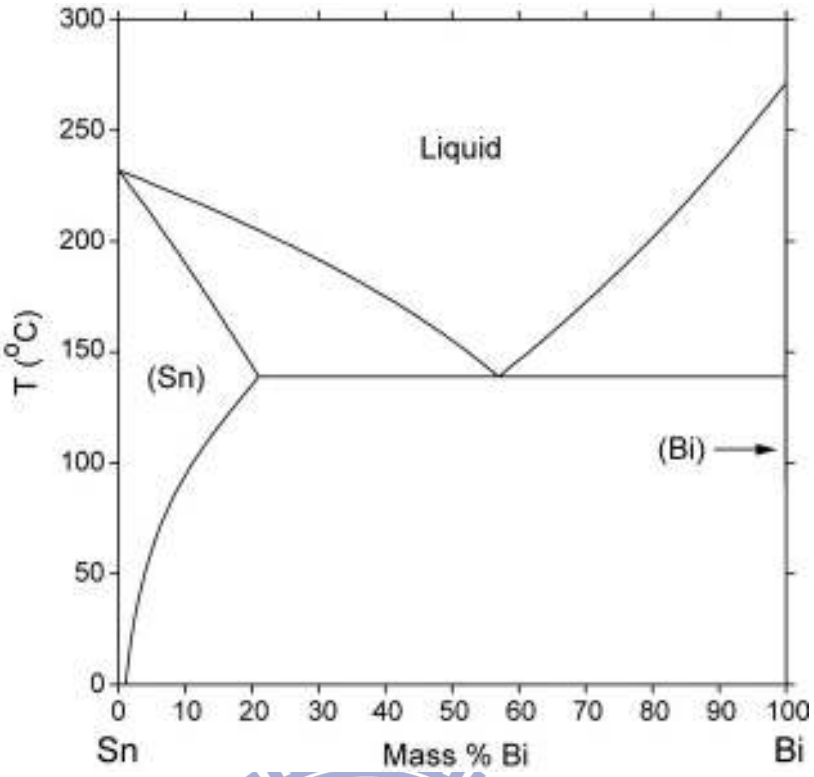

Figure 2.1 Phase diagram of Bi-Sn alloy [2].

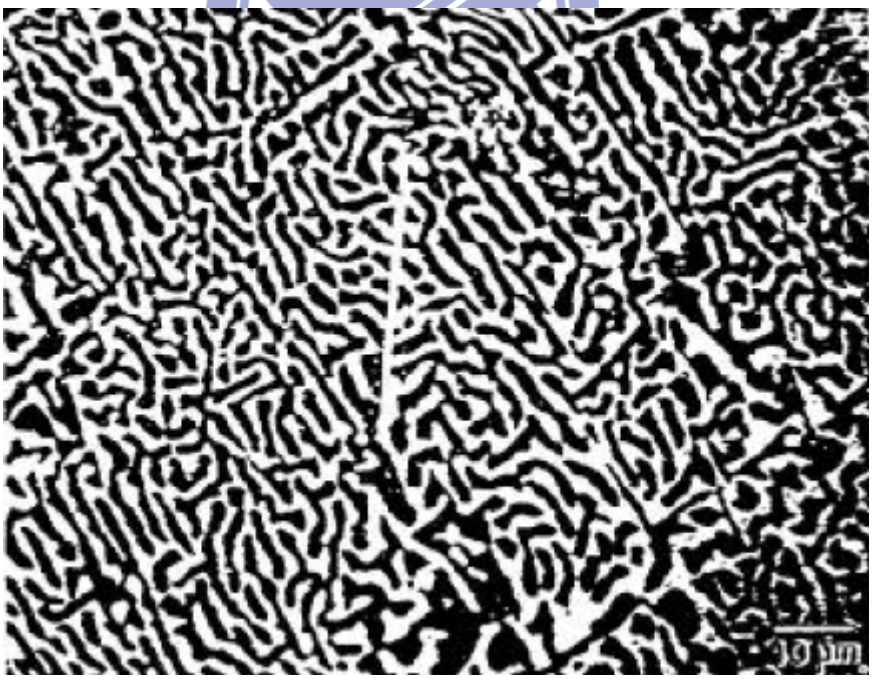

Figure 2.2 Microstructure of eutectic Bi-Sn alloy [3].

2.2 Fabrication of Nano-materials by Nonlithographic Methods

As the developments of modern science and technology, nano-science has become the main stream leading the progress of researches and industries since 1990s. Nanoscaled materials own the various novel characteristics, including the photonic [6], thermoelectric [7], magnetic [8, 9], electronic [10], and biological aspects [11]; therefore, the unique and fascinating properties have pushed scientists to explore the fundamental physical concepts and the possible usage in industrial applications.

Since Iijima has successfully produced carbon nanotubes [12] on 1991, the low-dimensioned nanoscale materials, such as nanotubes [13, 14], nanowires [15, 16], and nanorods [17, 18], have attracted much attention because of their interesting properties and potential to allow exploration of fundamental physical concepts and technological revolutions. Especially, nanowires are considered as ideal systems for investigating the dependence of electrical transport, optical and mechanical properties on size and dimensionality. In addition, they are expected to play an important role as both interconnects and functional components in the fabrication of nanoscale electronic and optoelectronic devices. The different properties of physical and chemical under nanoscale are due to size effect [19], quantum effect [20], and surface effect [21].

The techniques of synthesizing nanomaterials are getting mature, yet to array such small objects is still a challenge for researches and engineers. If the conventional lithography methods are applied to fabricate the structures with feature sizes smaller than 100nm, the experienced way will become an expensive and technically daunting task [22]. Therefore, the development turns to seek other possible nonlithographic fabrication methods [23]. While there are technological as well as economical limitation in lithography for ultra large scale integrated (ULSI) circuits fabrication in the forthcoming stage of sub-100 nm scale, much effort has been focused on nanostructure formation combined with self-assembly methods.

This offers a promising route to synthesize a large-area, ordered nanomaterial with high quality products, which is quite difficult to form by conventional lithographic process; thus, the template-assisted synthesis methods are gradually getting progressing.

"If we can use a template composed of well-arrayed patterns, the following formation process on it will prefer to begin at the preferred sites" that is the main concept of template-assisted fabrication methods. The common methods of fabricating nano-patterned templates include bottom-up self-assembly processes of AAO [24, 25], scanning probe technology, and direct-write electron-beam lithography [26, 27]. In using templates to produce nanostructures, one must take into account the template's chemical, mechanical, and thermal stability, insulating properties, the minimal diameter and uniformity of the pores, and the pore density. Aluminum anodization is one of the most controllable self-assembly processes. Anodic aluminum oxide (AAO) has received much attention, because of its high aspect ratio, uniform pore size, and ordering nanopores dispersion. Additionally, it is stable in the chemical and thermal surrounding, and an inexpensive process for fabrication. Detail on the structure and preparation of alumina templates can be found elsewhere [28-31].

A template-assisted synthesis is an elegant chemical or thermal approach for the fabrications of nanomaterials. Several processes have been proposed and introduced to the produce of nanostructure materials by using anodic aluminum oxide (AAO) as a template, such as the electrodeposition [32], the high-injection process [33], and chemical vapor deposition [34].

2.3 Vacuum Hydraulic Pressure Injection Process

To fabricate one-dimensional nano-materials via the template-assisted methods was widely combined with various synthesizing processes. Among them, the pressure injection method possessed the experience of metals and alloys casting processes, which has been studies and applied practically for several centuries. When casting was introduced to a new field, the former efforts could help us to clarify the formation mechanism and shorten the blurred stage basing on numerous literatures. In our laboratory, the anodic aluminum oxide (AAO) template-assisted casting process has been developed for several years [35-38], especially the hydraulic pressure injection method in recent [39-41]. Unlike vapor deposition processes or chemosynthesis, when a stoichiometric bulk material was produced, the following casting would not change the composite ratio of alloys until the injection process ended.

Recently, a high temperature gas pressure chamber has enabled the injection of bismuth (Bi) melt into AAO template as small as 13 nm in diameter [33]. Unlike most electrodeposition methods the injection process does not require a conducting substrate or catalyst, and develop another way to nanomaterials. It should be noted that the main constraint in this process is the high external pressure required to overcome the surface tension of the liquid metal melt to fill nanochannels. Thus, the smallest nanochannel that could be filled was compromised by the maximum pressure limit the gas chamber could sustain and operate safely. In case of higher pressure, wetting agent was added into Bi metal to lower the surface tension and hence reduce the required pressure to within the limit of the equipment. In Zhibo's group [33, 42], gas pressure injection process, the template was first dried and stabilized at 350 ℃ for 2 hrs and degassed at 250 ℃ for 8 hrs before injection. Their injection process lasted 5hr. They have stated that after injection, cooling the chamber to room temperature over a period longer than 12 hrs was crucial for achieving single crystal

Bi nanowires. Since the equipment they used could only sustain pressures up to 345 bars, the wetting agents were utilized to lower the contact angle and the required pressure. By doing so, for an average channel diameter of 56 nm, the filling ratio was improved to more than 90% since it was only 10% without using any surfactant. Bi melt was injected into the AAO successfully by gas injecting. However, the high pressure depends on the gas compressor, and the positive pressure chamber is expensive and dangerous to be operated. A vacuum hydraulic pressure injection process retains the advantages of gas injection, and reduces the high-pressure risks. The vacuum environment also prevents raw materials to be oxidized.

The vacuum hydraulic force injecting equipment, showed as Fig. 2.3, was used to fabricate the metal nanowires. The vacuum chamber and mold were made from 316L stainless steel (316L S.S.). For the process, the applied force was supplied by hydraulic force, and the argon gas was used to clean the chamber. Then, a piece of alloy was on the surface of AAO and both were in the vacuum chamber where vacuum was under 10^{-3} torr controlled by a rotary pump. When the chamber was superheated over the melting temperature of the alloy, the melt spread over the AAO surface. In the meantime, a hydraulic force was applied on the liquid melt and the melt was injected into AAO. Then, dip the injection chamber into cooling water base. After the molten alloy solidified in AAO, the alloy nanowires formed. The typical top-view and cross section images of Sn in AAO were showed as Fig. 2.4(a) and Fig. 2.4(b) [36].

The demanded force for melt to permeate into AAO template is proportional to the surface tension of melt; moreover, that can be calculated by the formula [43]:

$$P = F/A = 2\gamma\cos\theta/r \quad (1)$$

where F is the normal force, A is the area of the specimen, γ is the surface tension of melt, θ is the contact angle between AAO and melt, and r is the radius of nanochannel. While the equipment for gas injection can only bear a thrust pressure of 345 bars, that is able to take a compressive pressure of thousands bars. Thus, the vacuum hydraulic pressure injection not

only takes advantages of casting and template-assisted injection methods, but also performs a cheap, low-risk, and widespread-used technique.

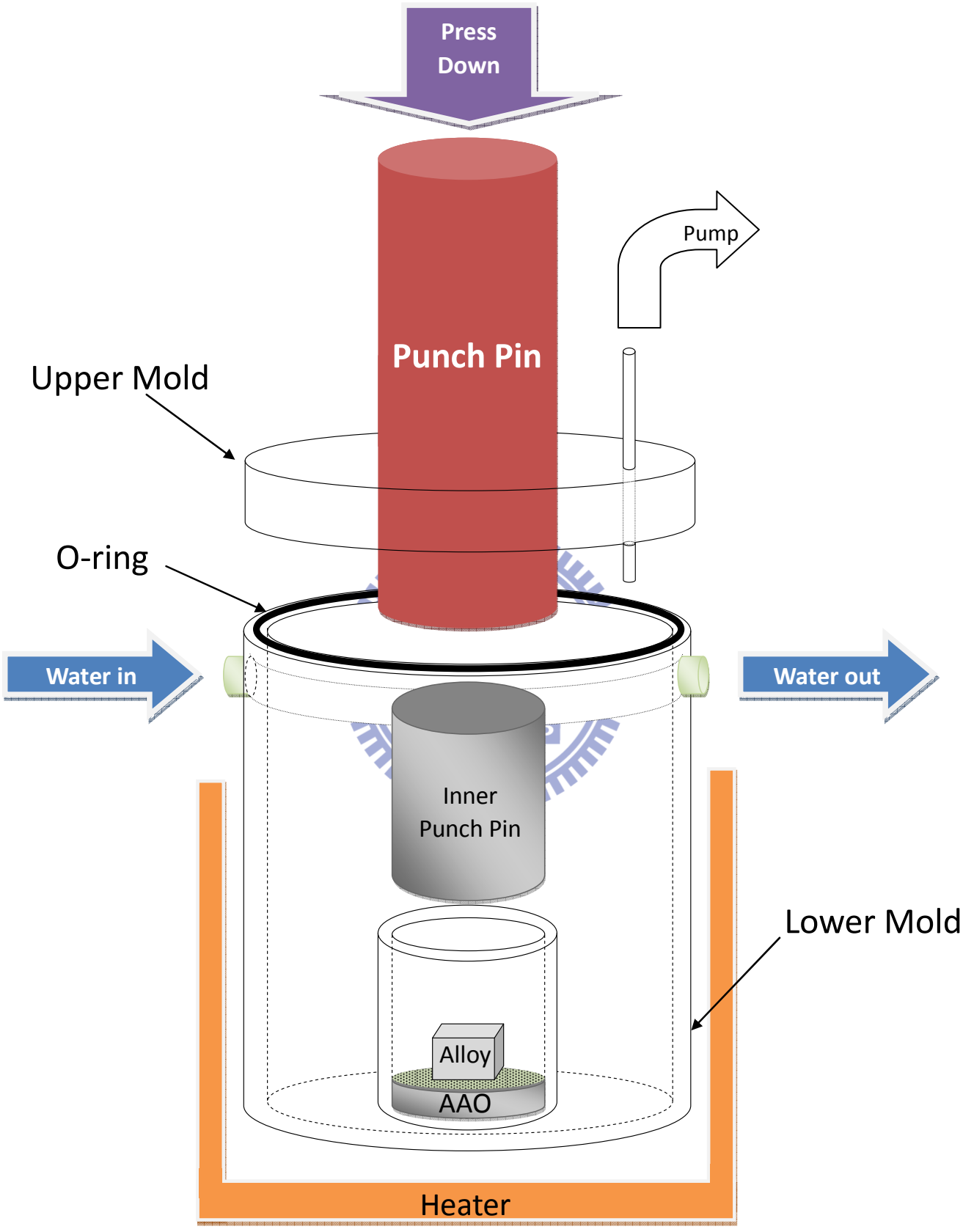

Figure 2.3 Schematic apparatus of vacuum hydraulic pressure injection process.

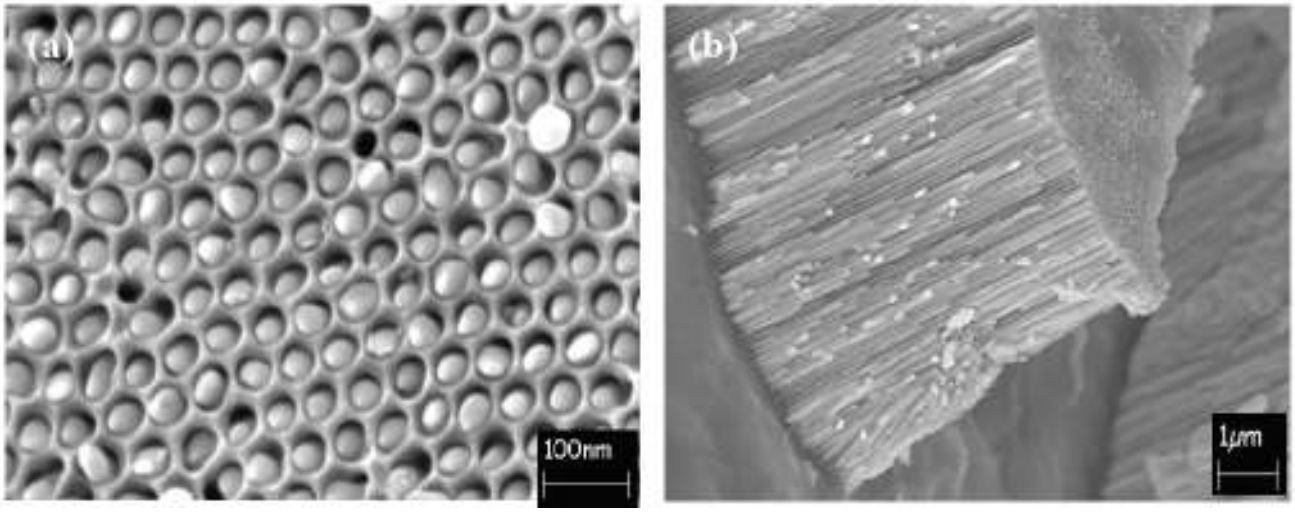

Figure 2.4 SEM image of Sn melt inside AAO, which formed Sn nanowires: (a) top view, (b) cross-section view [36].

2.4 Anodic Aluminum Oxide (AAO)

2.4.1 Introduction to AAO

In general, a bulk material call “template (or membrane)” must have well-controlled pattern on it, so it is able to fabricate other function devices according to the bulk’s model by particular processes. The existence of templates has already provides the solutions for many scientific and researching problems, such as the quantum effect, the limitation of light lithograph, biosensors on polymeric capsules and so on. Because of such popular applications in biology and science, many materials have been made into templates, inclusive of porous silicon, anodic aluminum oxide, artificial opals, polycarbonate, and electronically conductive polymers polypyrrole [44, 45].

That which kind of template is the best and useful exactly is really hard to be defined. Different templates satisfy the desires of different users. In our lab, we are interested in developing applications for the nano-materials by the template-assisted fabrications. The method we choose to synthesize nano-scaled materials is a melting injection process. Therefore, AAO is chosen in terms of its well-controlled patterns, high thermal stability, high aspect ratio and pore density, strong resistance against most chemicals, and the unique pore structure. In addition, AAO forming via the electrochemical process is also a low-cost way, and really eligible for experimental goals and limitations.

2.4.2 Electropolishing of Aluminum

In order to obtain a scrape free and fairly smooth surface for fabricating nano-scaled template, the substrate of aluminum surface must be electro-polished (EP) before the AAO-forming process. Electropolishing was invented by Pierre Jacquet in 1929 and was first successfully applied to the preparation of metallographic samples in 1935 [46]. However, it is most suitable for pure metals and single-phase alloys. On the contrary, multiphase alloys are

often quite difficult because of differences in the polishing rates of the constituents. There are some important variables for the EP. Those variables include the initial surface roughness, the electrolytic compositions, the electrolytic temperatures, the stirring rates of electrolyte, the applied voltages, the current density, and the polishing time. For example, if the roughness of initial surface is too coarse, EP time will be long, with excessive removal and waviness of bulks. For the voltage, the applied voltage is determined by the curves of voltage vs. current density (I-V curve), showed as Fig. 2.5. In the curve the plateau area is the suitable parameter for the EP. Focusing on the electrolytes, it must be rigorously controlled within very narrow limits to obtain satisfactory results. It always consists of a solvent, an attacking-ions solution, and a viscous solution. The solvent can be methanol (CH_3OH) or ethanol (C_2H_6O), the attacking-ions solution can be perchloric acid ($HClO_4$), hydrochloric acid (HCl), sulphuric acid (H_2SO_4), or phosphoric acid (H_3PO_4), and the viscous solution can be glycol monobutylether ($(CH_3(CH_2)_3OCH_2CH_2OH$) or glycerin ($C_3H_5(CH_3)_2$). As to the electrolyte temperature and stirring rates, when the bath temperature or stirring rate rises, the resistance of the bath decreases and the potential to the plateau current density decreases. In addition, if the viscosity of solution decreases, a viscous anode layer would become difficult to be maintained.

For reasons of economy the voltage is kept as low as possible. But the lower current density is applied, the longer time is consumed. Therefore, viscosity is important and its optimum value is in inverse proportion to the current density. During our experiments, a comparative higher voltage was chosen for saving time, and a dilute electrolyte was in propose of decreasing heat releasing from this reaction.

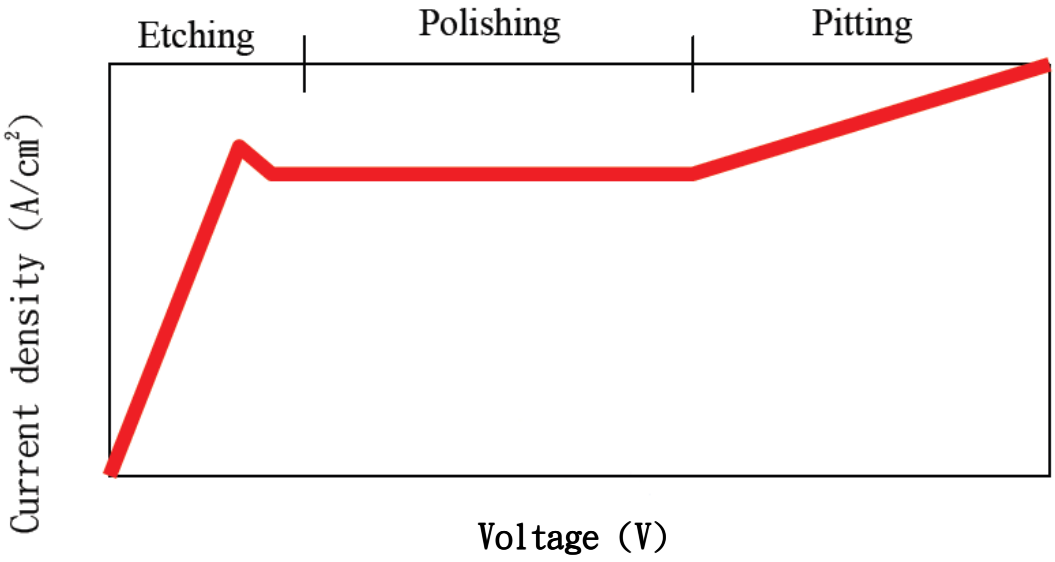

Figure 2.5 The I-V curve of etching, polishing and pitting sections.

2.4.3 Anodizing of Aluminum

When anodized in an acidic electrolyte and controlled in the suitable conditions, aluminum forms a porous oxide layer with uniform and parallel cell pores. Each cell contains an elongated cylindrical sub-micron or nano-pore normal to the aluminum surface, extending from the surface of the oxide to the oxide/metal interface, where it is sealed by a thin barrier oxide layer with approximately hemispherical geometry. Its structure is described as a close-packed array of columnar cells. The pore diameters and pore densities of anodic alumina film can be finely controlled by appropriately carrying out the electrochemical process parameters [47, 48]. Unstable metals, such as Al, Ti, Mg, Zr, Si …etc., dissolve by active corrosion in many solutions and become passive. This behavior is resulted from the inhibition of active dissolution by forming a dense passive film to block the ionic conductivity. Passive films are formed from the metal itself and the corrosive factors of environment, usually in water or in air. Anodic treatments of aluminum were intensively investigated to obtain protective or decorative film on its surface [49, 50].

When aluminum is anodizing in an acid, such as sulfuric acid (H_2SO_4), oxalic acid

($H_2C_2O_4$) or phosphoric acid (H_3PO_4), the formed pore array has the diameters between 5 nm to 300 nm and lengths of several microns. Setoh and Miyata [51] report that the anodic oxide film consists of two layers: the porous thick outer layer (porous type) that grows on an inner layer (barrier type), which is thin, dense and dielectrically compact, and called the barrier layer, the active layer or the dielectric layer. The barrier layer is very thin, typically with a thickness of between 0.1 and 2% of that of the entire film. The nanoporous layer builds on a columnar structure, and the pores' diameter depends on pH values, anodizing voltage, and the choice of acid. Generally, the structure is called "nanopores", "nanotubes" or "nanochannels".

Figure 2.6 shows the schematic illustration of an ideal ordered anodic aluminum oxide. The close-packed array of columnar hexagonal cells contains hollow tubes, corresponding to each pore. The bottom of pores is covered with a thin oxide layer, the barrier layer. If the residual aluminum substrate and barrier layer are removed, the pores become through channels. Figure 2.7 plots the relationship in three types of electrolytes about interpore distances and applied voltages for AAO forming process [52]. The optima self-organized ordered structures occur at 25 V in sulfuric acid, 40 V in oxalic acid and 195 V in phosphoric acid, corresponding to cell sizes of 65, 100 and 500 nm, respectively [53-55].

Figure 2.8 shows the SEM images of fabricated AAO pores with the size of 20 nm, 70 nm, and 220 nm respectively [40]. The fabrication using 10 vol-% sulfuric acid as electrolyte results AAO with uniform distribution of pores, 20 nm in diameter, as shown in Fig. 2.8 (a). The AAO template, with pores of 70 nm in diameter, is fabricated by using 3 vol-% oxalic acid as electrolyte, as shown in Fig. 2.8 (b). Finally, the largest pores with 220 nm in diameter, are produced by 1 vol-% phosphoric acid, as shown in Fig. 2.8 (c).

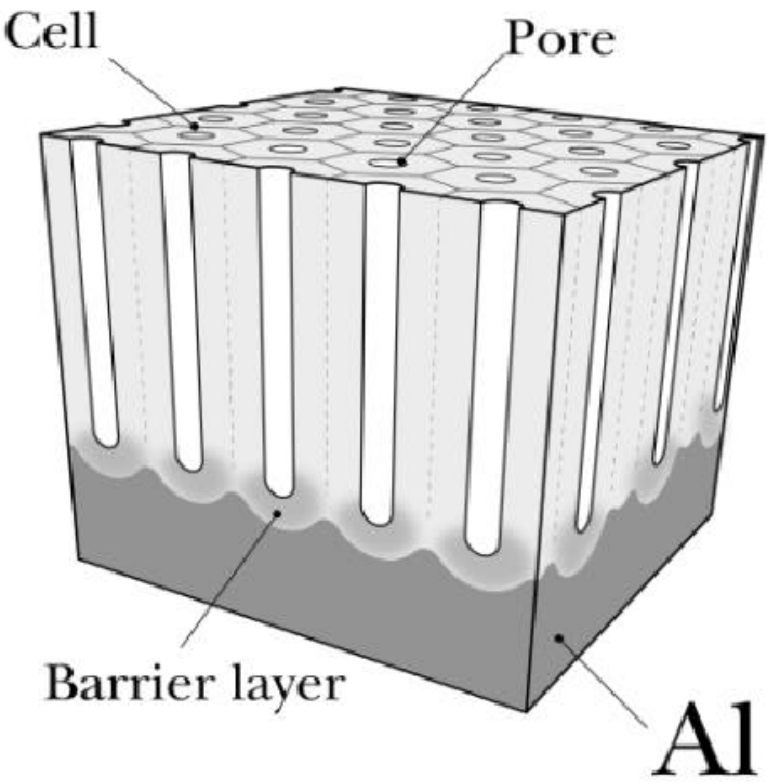

Figure 2.6 Schematic image of an ideal ordered anodic porous alumina.

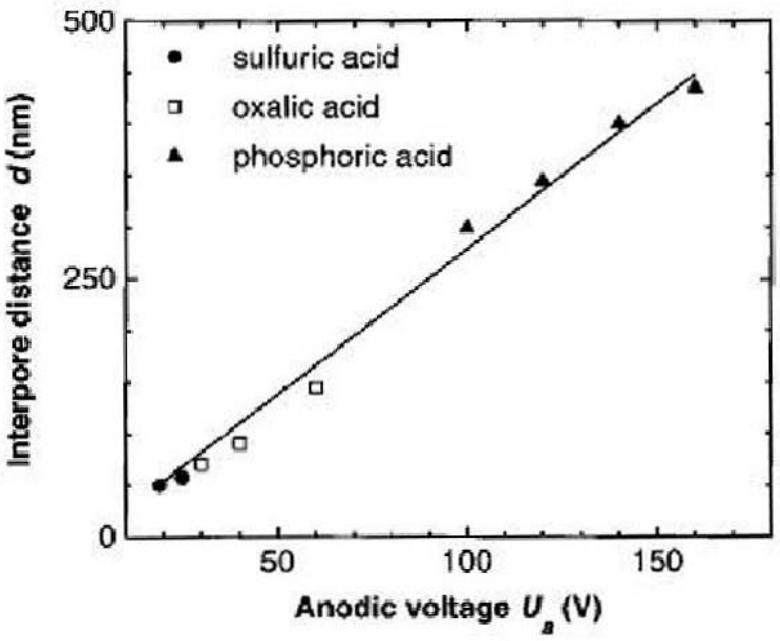

Figure 2.7 Relationship between interpore distances and anodic voltages for AAO forming process in sulfuric acid, oxalic acid, and phosphoric acid, respectively [52].

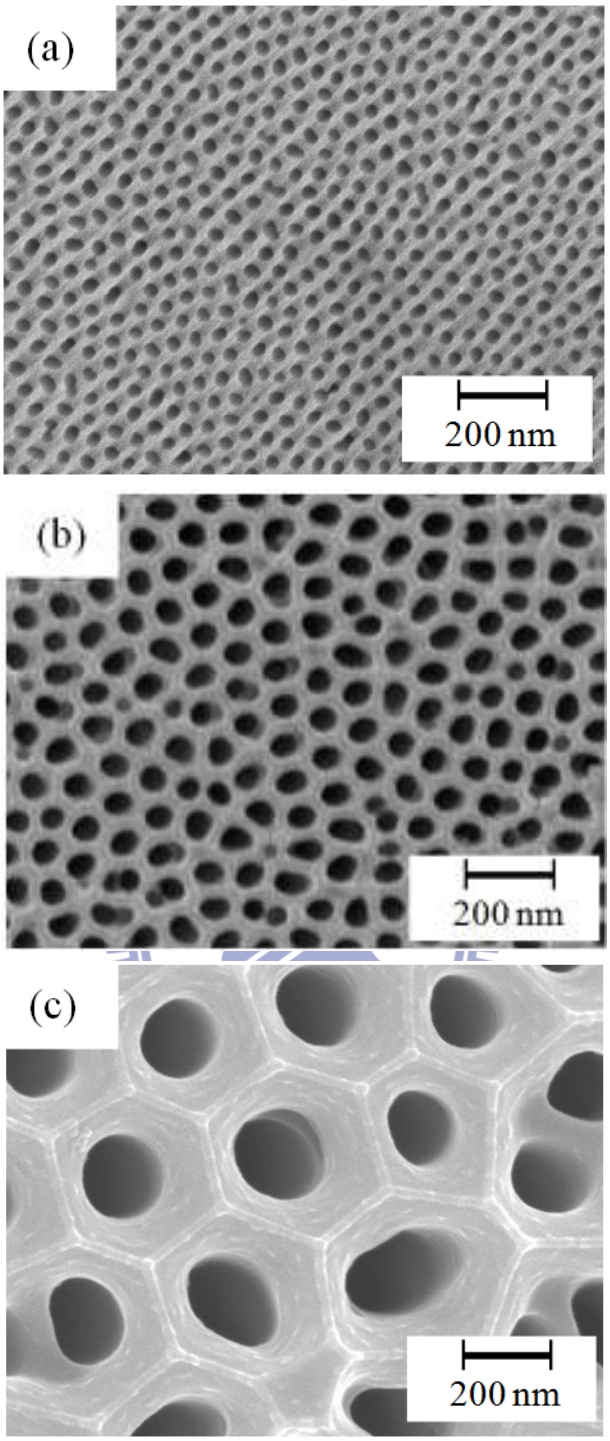

Figure 2.8 SEM images of AAO pores with the size of (a) 20 nm, (b) 70 nm, and (c) 220 nm respectively [40].

2.5 Fluid Mechanics principles of Melting Alloys within nanowires

The nanostructure materials that were synthesized by this injection process formed an oxide shell after the removal of AAO template. This spontaneous oxide shell was stable and served as a container to preserve the alloys inside for following applications, especially at high temperature. If the temperature is higher than the melting point of alloy, the molten material is like a fluid in pipes. The behavior of this liquid would be governed and predicted by the fluid-mechanics principles. Therefore, some common concepts of the fluid mechanics are reviewed for the applications of nanowires.

Like applications ranging from large, man-made Alaskan pipeline that carries crude oil almost 800 miles across Alaska, to the more complex natural system of "pipes" that carry blood throughout our body and air into and out our lung, the melting alloys solidified in AAOs and the re-melting metal fluid in core-shell nanotubes are also the common examples governed by the fluid-mechanics. The transport of a fluid (liquid or gas) in a closed conduit (commonly called a pipe if it is of round cross section or a duct if it is not round) is extremely in our daily operations. A brief consideration of the world around us will indicate that there is a wide variety of application of pipe flow. Although all of systems are different, the fluid-mechanics principles governing the fluid motions are common. Here, only a simple case is considered, and assumed that the conduit is round and the pipe is completely filled with the fluid being transported.

Before starting with the fluid in pipe, the characteristics of fluid should be determined first. The flow of a fluid in a pipe may be *laminar* flow or *turbulent* flow, as illustrated in Fig. 2.9. For pipe flow the most important dimensionless parameter is the Reynolds number, Re – the ratio of the inertia to viscous effects in the flow [56].

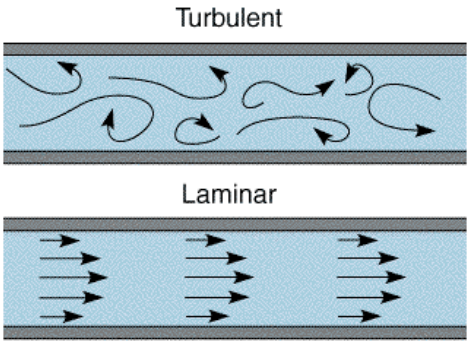

Figure 2.9 Illustration of types of flow inside a pipe.

Reynolds number, Re = $\rho VD/\mu$, where ρ is the fluid density, V is the average velocity, D is the pipe diameter, and μ is the fluid viscosity. Typically, fluid flows are laminar for Reynolds Numbers up to 2000. Beyond a Reynolds Number of 4000, the flow is completely turbulent. Between 2000 and 4000, the flow may switch between laminar and turbulent conditions in an apparently random fashion (transitional flow). For nanowires, the diameters of them are approximately 10^{-5} to 10^{-7} cm and the viscosity of molten alloy is usually higher than most liquids. So their Reynolds numbers are always much less than 2000, and the fluid within a nanowire can be considered as a *laminar* flow.

To evaluate the properties of the laminar flow in a straight pipe, some assumptions should be satisfied [56]:

(1) The fluid is an **incompressible flow**; that is, its density is a constant value.

(2) **A steady flow**. The fluid velocity would not vary with time.

(3) The fluid field is **axially symmetry**. The velocity is the highest at the center of axis and the lowest at boundary, and is symmetric along its axis.

(4) **Fully developed laminar fluid**. The velocity distribution is a parabolic curve.

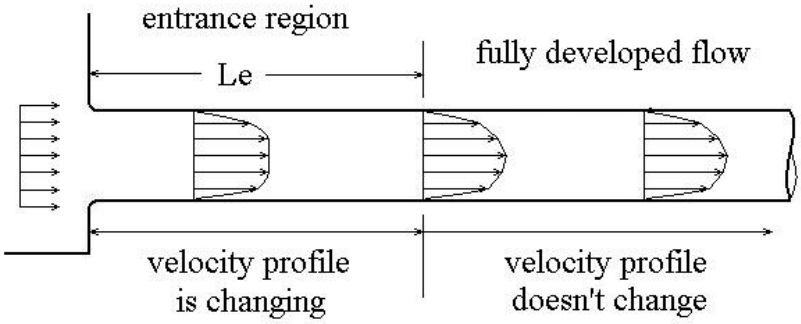

Figure 2.10 Illustration of developing stages of the flow in a pipe.

According to those assumptions, the fluid can be evaluated by Poiseuille's law:

$$Q = \frac{\pi D^4 \Delta P}{128 \mu l} \quad \text{..... (1)}$$

where Q is the flow rate, $\triangle P$ is the pressure difference, and l is the pipe length. In addition, $Q = V/A$ and $A = \pi D^2/4$, so

$$V = \frac{D^2 \Delta P}{32 \mu l} \quad \text{..... (2)}$$

In the case of nanowires of a fixed composition, the pressure difference and the fluid viscosity could be assumed constants. The environment and fluid are fixed, so the velocity is only proportional to the square of the nanotube diameter. For example, when Bi-Sn eutectic nanowires of 200 nm are annealed over its melting point, the fluid velocity of 200 nm nanowire is about 8 times higher than that in a 70 nm.

2.6 Solidification of Eutectic

Eutectic alloys are extremely important in the industrial fields such as metallurgical, material, welding and soldering, owing to their peculiar characteristics: lower melting point, excellent flow properties and the formation possibility of in-situ composites [57]. Up to now, the growth of eutectic has still received considerable theoretical, experimental, and simulative attention [58–62]. Figure 2.11 shows that eutectic structure forms when the temperature and solute composition are at eutectic point.

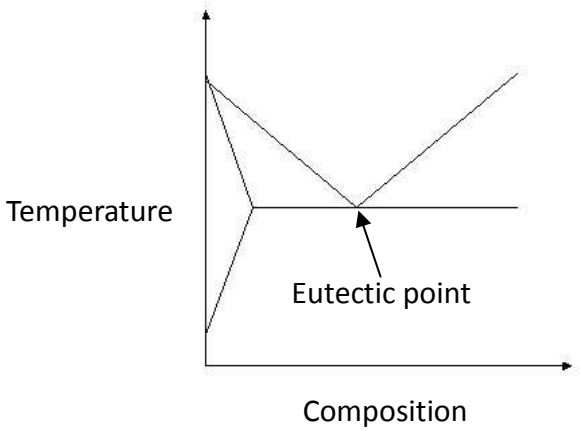

Figure 2.11 Eutectic point at binary phase diagram.

From the viewpoint of technology, two characteristic parameters of eutectic microstructures: the volume fractions of the eutectic phases and the lamellar spacing, which can be controlled experimentally, are most important. The former is controlled to some extent by the composition of the alloy [63], whereas the latter is mainly controlled by the growth rate or the cooling rate. In other words, the crystal distribution within eutectic alloys is controlled by solidification.

Solidification of a eutectic alloy from the melt or liquid phase produces two composite solid phases, in contrast to the simpler case when the liquid phase solidifies into a single solid phase. The two solid phases are characterized by differing solute concentrations; the equilibrium concentrations in each phase are given by the phase diagram for the eutectic

system, which gives the relations between temperature and solute concentration for each of the thermodynamic phases in the system. A number of different geometrical arrangements of the two solid phases are possible, depending on the alloy system and on the processing conditions. For example, the solid phases can form in adjacent layers or lamellae, or one phase can form rods that are embedded in the other phase. Both grow continuously from the melt. Since a large number of important binary alloy systems have eutectic phase diagrams, such systems have been studied extensively. It is desirable to be able to predict the geometrical patterns of growth and their associated length scales in order to better understand and possibly control the processing of eutectic materials.

The eutectic growth in metal-metal system does not depend on the crystal orientation because the solid-liquid interface is rough. Therefore, the heat and mass transfers determine the eutectic growth. Figure 2.12 demonstrates the eutectic growth model. When α-phase grows, the solute composition in front of α-phase is suitable to grow β-phase. And the solute composition in front of the β-phase is suitable to grow α-phase. Solute diffuses transverse to the growing interface so that α and β phases grow alternatively. Because of the growth mechanism, the eutectic spacing, λ, is very small. Images in Fig. 2.13 are the typical eutectic microstructures.

For regular binary eutectics, most of the steady state eutectic growth theories are based on the classical work of Jackson and Hunt [64] published five decades ago. Referring to the theoretical work by Zener [65] and Brandt [66] in the pearlite growth, they introduced the minimum undercooling principle suggested by Tiller [67] to determine the selection of lamellar spacing, and built the relationship between the lamellar spacing and the processing parameters.

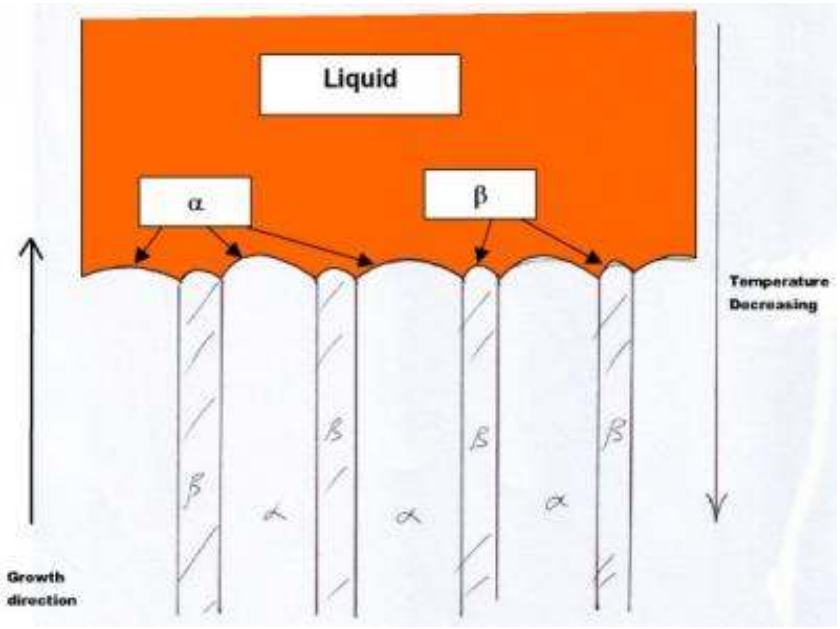

Figure 2.12 Illustration of eutectic solidification.

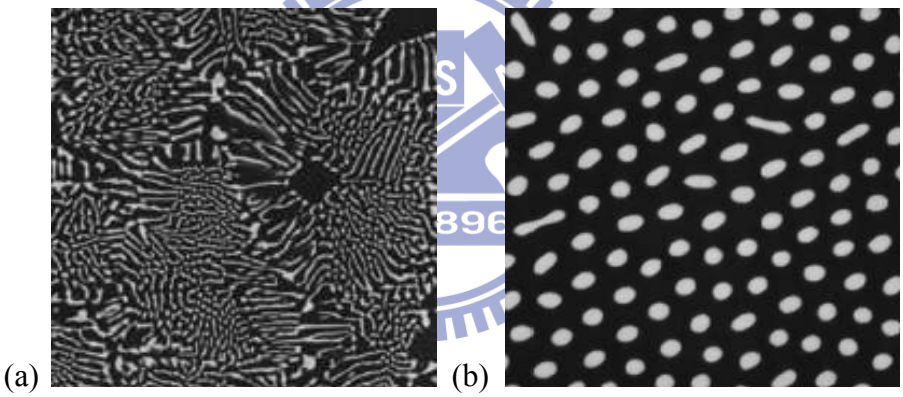

Figure 2.13 Typical eutectic microstructures. [68]

As pointed out by Jackson and Hunt, there is experimental evidence that only a finite range of spacing will be stable with respect to fluctuations in the shape of the interface[69–71], and the minimum undercooling principle only determines the lower limit of selection range of eutectic spacing. Thus, the solidification behavior of eutectic Bi-Sn nanowires is presented according to the assumption of equilibrium at the interface during growth in Chapter 4.

2.7 One-Dimensional Bismuth Oxide (Bi_2O_3) and Tin Oxide (SnO_2)

2.7.1 Bismuth oxide

Bismuth oxide (Bi_2O_3) is an interesting material and very important in modern solid-state technology. It is fascinating to scientists owing to its unique structures and physical properties, such as a large energy band gap, high refractive index, dielectric permittivity and high oxygen-ion conductivity, as well as marked photoconductivity and photoluminescence (PL) [72–75]. These special features of Bi_2O_3 make it suitable for a large range of applications, such as sensors, optical coatings, photovoltaic cells and microwave integrated circuits [76–79]. These features explain the great effort devoted to the investigation of Bi_2O_3 polymorphs over the past few years.

Bi_2O_3 has five polymorphic forms that are denoted by α-Bi_2O_3 (monoclinic), β-Bi_2O_3 (tetragonal), γ -Bi_2O_3 (body centred cubic), δ-Bi_2O_3 (cubic), and ε-Bi_2O_3 (orthorhombic) [80, 81]. Among them, the low-temperature α-phase and the high-temperature δ-phases are stable, but the others are high-temperature metastable phases [82]. The tetragonal β-Bi_2O_3, which has a distorted defect-fluorite structure, is a metastable phase at ambient conditions and usually transforms into the stable monoclinic α-Bi_2O_3 at about 870 K. Each polymorph possesses distinct crystalline structures and physical properties (electrical, optical, mechanical, etc). Figure 2.14 shows the transformation temperatures and structures of various Bi_2O_3.

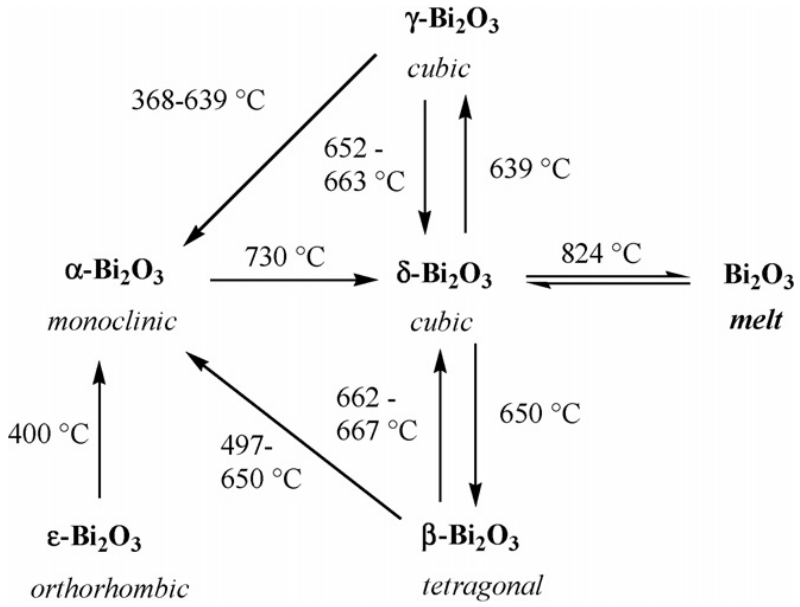

Figure 2.14 Transformation temperatures for α-, β-, γ-, δ- and ε-Bi_2O_3 [83].

2.7.2 Tin oxide

SnO_2 is an n-type semiconductor crystal with direct band gap (3.7 eV at 300 K) having high excitonic binding energy (130eV). SnO_2 has been applied in many applications such as transparent conducting coating of glass, gas sensors, solar cell, and heat mirror [84–86]. However, the bandgap of SnO_2 is too large to utilize the visible portion of the solar spectrum, but its low lying conduction band makes it possible to efficiently accept photogenerated electrons from other semiconductors when used in multi-component systems (i.e. SnO_2/ZnO, SnO_2/TiO_2), which can significantly reduce the rate of electron-hole recombination [87].

The synthesis and gas sensing properties of semiconducting SnO_2 nano-materials have become one of important research issues since the first synthesis of SnO_2 nanobelts by Pan et al. [84]. Yamazeo and Miura [88] studied the effect of grain size on the sensitivity of SnO_2 gas sensors and concluded that the sensitivity to both CO and H_2 increased considerably as grain size was reduced. Li and Kawi [89] synthesized high surface area SnO_2 using a surfactant templating method and found that the sensitivity to H_2 increased linearly with the

surface area of SnO_2. When particle size is reduced to nanometers, especially when the dimension of the crystallite is on the order of the thickness of the charge depletion layer, energy band bending is no longer restricted to the surface region, but extends into the bulk of the grains. In other words, the properties of the whole grain, not just the surface, may change completely due to solid–gas interaction. Accordingly, nanostructure is expected to have a dramatic influence on sensor performance.

References

[1] E.P. Wood, K.L. Kimmo, *Journal of Electronic Materials* **1994**, 23, 709.

[2] Metallurgy Division, National Institute of Standards and Technology (http://www.metallurgy.nist.gov/phase/solder/bisn.html)

[3] J. Glazer, *Int. Mater. Rev.* **1995**, 40, 65.

[4] E.W. Hare, R. Corwin, E.K. Riemer, *in Proc. "ASM. International electronic packaging materials and process conf."* **1985**, 109.

[5] W.G. Moffatt, G.W. Pearsall, J. Wulff, *"The structure and properties of materials: Vol. 1, structure"*, New York, Wiley. **1964.**

[6] C.P. Collier, R.J. Saykally, *Science* **1997**, 277, 26.

[7] J.G. Lee, H. Mori, *Phys Rev. B* **2002**, 65, 1.

[8] S. Sun, C.B. Murray, *Science* **2000**, 287, 198.

[9] A. Moroz, *Phys. Rev. Lett.* **1999**, 83, 5274.

[10] A.M. Morals, C.M. Lieber, *Science* **1998**, 279, 208.

[11] D.M. Hartmann, M. Heller, *J. Mater. Res.* **2000**, 17, 473.

[12] S. Iijima, *Nature* **1991**, 354, 56.

[13] Y.C. Sui, R. Skomski, K.D. Sorge, D.J. Sellmyer, *Appl. Phys. Lett.* **2004**, 84 1525.

[14] A. Wei, X.W. Sun, C.X. Xu, Z.L. Dong, M.B. Yu, W. Huang, *Appl. Phys. Lett.* **2006**, 88 213102-1.

[15] W. Ensinger, P. Vater, *Mater. Sci. Eng. C* **2005**, 25, 609.

[16] Q. Hu, G. Li, H. Suzuki, H. Araki, N. Ishikawa, W. Yang, T. Noda, *J. Crystal Growth* **2002**, 246, 64.

[17] S. B. Qadri, M. A. Imam, C. R. Feng, B. B. Rath, M. Yousuf, and S. K. Singh, *Appl. Phys. Lett.* **2003**, 83, 548.

[18] Y. Liu, Y. Dong, G. Wang, *Appl. Phys. Lett.* **2003**, 82, 260.

[19] Y.F. Zhang, Z. Tang, T.Z. Han, X.C. Ma, J.F. Jia, Q.K. Xue, K. Xun, S.C. Wu, *Appl. Phys. Lett.* **2007**, 90, 093120.

[20] Y.M. Wan, H.T. Lin, C.L. Sung, S.F. Hu, *Appl. Phys. Lett.* **2005**, 87, 123506.

[21] G.F. Wang, T.J. Wang, X.Q. Feng, *Appl. Phys. Lett.* **2006**, 89, 231923.

[22] F. Burmeister, C. Schaffe, *Adv. Mater.* **1998**, 10, 495.

[23] R. Notzel, Semicond. *Sci. Technol.* **1996**, 11, 1365.

[24] G.E. Thompson, G.C. Wood, *Nature* **1981**, 290, 230.

[25] Ying, United States Patent, **2001** Patent No. 6231744.

[26] S.Y. Chou, P.R. Krauess, *J. Appl. Phys.* **1996**, 79, 6101.

[27] S.Y. Chou, P.R. Krauess, *Scr. Metall. Mater.* **1995**, 33, 1537.

[28] G.E. Thompson, R.C. Furneaux, *Corrosion Sci.* **1978**, 10, 481.

[29] G.E. Thompson, G.C. Wood, *Nature* **1981**, 290, 230.

[30] K. Ebihara, H. Takahashi, *J. Met. Finish. Soc. Jap.* **1983**, 34,, 548.
[31] J. Li, C. Papadopoulos, *Nature*, **1999**, 402, 253.
[32] N.I. Kovtyukhov, B.R. Martin, *Mater. Sci. Eng. C* **2002**, 19, 255.
[33] Z. Zhibo and Y.Y. Jackie, *J. Mater. Res.* **1998**, 13, 1745
[34] A. Govyadinov, P. Mardilovich, *Electrochem. Soc. Porceedings* **2000**, 28, 74.
[35] C.C. Chen, C.G. Kuo, J.H. Chen, C.G. Chao, *Jpn. J. of Appl. Phys.* **2004**, 43, 8354.
[36] C.C. Chen, Y. Bisrat, Z.P. Luo, R.E. Schaak, C.G. Chao, D.C. Lagoudas, *Nanotechnology* **2006**, 17, 367.
[37] C.C. Chen, C.G. Kuo, C.G. Chao, *Jpn. J. Appl. Phys.* **2005**, 44, 1524.
[38] J.H. Chen, C.G. Chao, J.C. Ou, T.F. Liu, *Surface Science* **2007**, 601, 5142.
[39] J.H. Chen, S.C. Lo, C.G. Chao, T.F. Liu, *J. Nanosci. Nanotechnol.* **2008**, 8, 967.
[40] S.H. Chen, C.C. Chen, Z.P. Luo, C.G. Chao, *Materials Letters* **2009**, 63, 1165.
[41] S.H Chen, C.C. Chen, C.G. Chao, *Journal of Alloys and Compounds* **2009**, 481, 270.
[42] Z. Zhang, D. Gekhtman, *Chem. Mater.* **1996,** 11, 1659.
[43] A.P. Alivisatos, *Science* **1996**, 271, 933.
[44] D. Gong, C.A. Grimes, *J. Mater. Res.* **2001**, 16, 3331.
[45] N.V. Gaponenko, *Synthetic Metals* **2001**, 124, 125.
[46] G.F. Vander Voort, "Metallography Principles and Practice ", *McGraw-Hill book company*, **1984**.
[47] C.A. Huber, T.E. Huber, *Science* **1994**, 263, 800.
[48] D. Routkevitch, J.M. Xu, *Trans. Electron. Dev.* **1996**, 43, 1646.
[49] L. Young, "Anodic oxide films", *Academic Press*, New York, **1961**.
[50] S. Tajima, *Adv. Corros. Sci. Tech.* **1970**, 1, 229.
[51] S. Setoh, A. Miyata, *Sci. Inst. Phys. Chem. Res.*, Tokyo, **1932**, 2772.
[52] A.P. Li, *J. Appl. Phys.* **1998**, 84, 6023.
[53] H. Masuda, K. Fukuda, *Science* **1995**, 268, 1466.
[54] H. Masuda, F. Hasegwa, S. Ono, *J. Electrochem. Soc.* **1997**, 144, L127.
[55] H. Masuda, K. Yada, A. Osaka, *Jpn. J. Appl. Phys.* **1998**, 37, 1340.
[56] B.R. Munson, D.F. Young, T.H. Okiishi, "Fundamentals of Fluid Mechanics, 3rd ed.", *John Wiley*, New York ,**2003**.
[57] W. Kurz, D.J. Fisher, *Int. Metal. Rev.* **1979**, 24, 177.
[58] W. Kurz, *Adv. Eng. Mater.* **2001**, 3(7), 443.
[59] A. Karma, M.Plapp, *JOM* **2004**, 56(4), 28.
[60] Y.J. Chen, S.H.Davis, *Acta Mater.* **2001**, 49(8), 1363.
[61] W.M. Wang, J.M. Liu, Z.G. Liu, *J. Mater. Sci. Technol.* **2002**, 18(4), 322.
[62] K.W. Huai, J.T. Guo, Z.R. Ren, Q. Gao, R. Yang, *J. Mater. Sci. Technol.* **2006**, 22(2), 164.
[63] F.R. Mollard, M.C. Flemings, *Trans. Met. Soc. AIME* **1967**, 239, 1526.

[64] K.A. Jackson, J.D.Hunt, *Trans. Met. Soc. AIME* **1966**, 236, 1129.
[65] C. Zener, *Trans. Met. Soc. AIME* **1946**, 167, 550.
[66] W.H. Brandt, *J. Appl. Phys.* **1945**, 16, 139.
[67] W.A. Tiller, "*Liquid Metals and Solidification, ASM,*" Metals Park, OH, **1958**.
[68] W.S. Chang, B.C. Muddle, *Metall. Mater. Trans.* **1997**, 28A, 1543.
[69] R.M. Jordan, J.D. Hunt, *Metall. Trans.* **1971**, 2, 3401.
[70] R. Trivedi, J.T. Mason, J.D. Verhoeven, W. Kurz, *Metall. Trans.* **1991**, 22A, 2523.
[71] V. Seetharaman, R.Trivedi, *Metall. Trans.* **1988**, 19A, 2955.

[72] L. Leontie, M. Caraman, M. Alexe, C. Harnagea, *Surf. Sci.* **2002**, 507, 480.
[73] V. Fruth, M. Popa, D. Berger, R. Ramer, M. Gartner, A. Ciulei, M. Zaharescu, *J. Eur. Ceram. Soc.* **2005**, 25, 2171.
[74] H.T. Fan, X.M. Teng, S.S. Pan, C. Ye, G.H. Li, L.D. Zhang, *Appl. Phys. Lett.* **2005**, 87, 231916.
[75] R.L. Thayer, C.A. Randall, S. Trolier-McKinstry, *J. Appl. Phys.* **2003**, 94, 1941.
[76] E. Kanazawa, G. Sakai, K. Shimanoe, Y. Kanmura, Y. Teraoka, N. Miura, N. Yamazoe, *Sensors Actuators B* **2001**, 77, 72.
[77] J. Fu, *J. Mater. Sci. Lett.* **1997**, 16, 1433.
[78] J. George, B. Pradeep, K.S. Joseph, *Phys. Status Solidi a* **1987**, 100, 513.
[79] K.L. Chopra, S.R. Das, "Thin Film Solar Cells", *Plenum,* New York **1983**.
[80] S.K. Blower, C. Greaves, *Acta Crystallogr. C* **1998**, 44, 587.
[81] A.F. Gualtieri, S. Immovilli, M. Prudenziati, *Powder Diffract.* **1997**, 12, 90.
[82] P. Shuk, H.D. Wiemhőfer, U. Guth, W. Gőpel, M. Greenblatt, *Solid State Ion.* **1996**, 89, 179.
[83] M. Michael, *Coord. Chem. Rev.* **2007**, 251, 974.
[84] Z.W. Pan, Z.R. Dai, Z.L. Wang, *Science* **2001**, 291, 1947.
[85] N. Kudo, Y. Shimazaki, H. Ohkita, M. Ohoka, S. Ito, *Solar Energy Mater. Solar Cells* **2007**, 91, 1243.
[86] C. Choudhury, H.K. Sehgal, *Energy Convers. Manage.* **1989**, 29, 265.
[87] K. Vinodgopal, I. Bedja, P.V. Kamat, *Chem. Mater.* **1996**, 8, 2180.
[88] N. Yamazeo, N. Miura, *Chem. Sensor Tech.* **1992**, 4, 19.
[89] G.J. Li, S. Kawi, *Mater. Lett.* **1998**, 34, 99.

PART I: Fabrication –

Chapter 3 Fabrication and Characterization of Eutectic Bismuth-Tin (Bi-Sn) nanowires

3.1 Background and Motivation

In the history of the electronic industry, lead-tin solders have been widely used due to their favorable physical and mechanical properties, and well-developed production process [1-6]. However, concerns on the harm of Pb to the environment and human health [7] challenge the electronic industry seek for lead-free solutions. Great efforts have been made to various tin-containing binary and ternary alloys with the absence of Pb. [7-12]. Among them, an eutectic Bi-43Sn (in weight percent) alloy was recognized for its net eutectic texture, lower melting temperature (~ 138 °C), superior wettability, and almost void-free bonding [13, 14].

Towards the miniaturization of consumer electrics and optical products, nano-scaled solders for tiny bonding with enhanced desired properties are highly demanded. It is generally accepted that reduced size and dimensionality are the critical factors in defining the properties of a material, which are often unforeseen in the bulk materials [15]. Especially, one-dimensional electric materials have attracted great interest and have been extensively investigated for their unique size effects [16], typically fabricated using chemical reduction, chemical vapor deposition, heating in chunks, mechanical alloying, and gas pressure injection [17-28]. Recently, a vacuum injecting process was developed, which was an easy and reproducible way to prepare metal nanowires with high efficiency [29, 30]. As compared with the gas pressure injection method [18], this technique applies hydraulic pressure instead of gas compressor, and thus no surfactant is impregnated into the AAO templates along with the metal melt.

So far, limited efforts were made on the system with multiple components, particularly, the eutectic system. Fig. 1 is the Bi-Sn binary phase diagram [31], which presents a typical example of the eutectic reaction during the solidification process, *i.e.* at the Bi-43.03 wt-% Sn composition, *L* (liquid) → Bi (solid) + Sn (solid) which occurs at 138.8 ºC temperature. In this study, for the first time nanowires are fabricated using this eutectic Bi-43Sn solder material, and characterize the nanowire metallurgical microstructure as compared to the bulk sample in details.

3.2 Experimental Procedures

The anodic aluminum oxide (AAO) templates were fabricated by the anodization process. Using this method, a commercial purity aluminum foil (Al, 99.7%) was initially anodized to AAO templates, with average pore diameters of 20 nm, 70 nm and 220 nm, by using 10 vol-% sulfuric acid (H_2SO_4) at 20 V, 3 vol-% oxalic acid ($H_2C_2O_4$) at 40 V, and 1 vol-% phosphoric acid (H_3PO_4) at 160 V respectively. The pore depth was about 10 μm. More experimental details about the anodization process are found in our previous research [32]. After the processes, the remaining extra Al substrate served as a support base for the brittle porous AAO template through the following injection process.

The bismuth-tin (Bi-Sn) eutectic bulk alloy, the starting material for the nanowires, was produced by using a vacuum smelting process. Based on the Bi-Sn phase diagram (Fig. 3.1), the eutectic point at the composition of 57 wt-% Bi and 43 wt-% Sn was selected as the experimental material composition. Raw materials of Bi and Sn in this ratio were sealed into a glass tube and then pumped down to a high vacuum (~ 10^{-5} torr). Afterward, the materials inside the tube were heated over their melting points to ensure both of them completely melt and well mixed into each other, and then slowly cooled down to room temperature. The obtained bulk sample was placed into the injection apparatus, and heated up above 200 ºC to

melt again, and then injected into the AAO pores by a hydraulic force. Through solidification to room temperature, the eutectic Bi-Sn nanowires were formed inside the AAO template. The vacuum hydraulic pressure injection apparatus was disclosed previously [29].

Characterizations of AAO and Bi-Sn nanowires were performed by scanning electron microscopy (SEM, JEOL 6500F FESEM and FEI Quanta 600 FESEM), X-ray energy dispersive spectroscopy (EDS), X-ray diffraction (XRD, Bruker D8), differential scanning calorimeter (DSC, Perkin-Elmer Pyris 1), transmission electron microscopy (TEM, JEOL 2010 at 200 kV), and scanning TEM (STEM, FEI Tecnai G^2 F20 at 200 kV). The TEM/STEM images were calibrated using standards of 6*H* SiC single-crystal lattice fringes [33] and a cross-line grating replica.

3.3 Results and discussion

The prepared starting material, bulk Bi-Sn eutectic alloy, exhibits a lamellar microstructure. A back-scattered SEM image of the bulk sample is shown in Fig. 3.2(a); in such an imaging mode the contrast is prepositional to the atomic number *Z*. The X-ray EDS analysis shows that the bright area in Fig. 3.2(a) is Bi (heavier), and the dark area, Sn (lighter). The EDS mapping of Bi and Sn are shown in Figs. 3.2(b) and (c) respectively, where the elements chosen for mapping exhibit higher intensities over the rest dark areas. The XRD pattern in Fig. 3.2(d) reveals that this sample composes of single Bi and Sn elements only, without any binary compounds. In addition, the DSC spectrum, as shown in Fig. 3.2(e), indicates the melting point of the Bi-Sn bulk sample as 138 °C, which is consistent to the eutectic point in the Bi-Sn phase diagram in Fig. 1. All these results indicate that this vacuum smelting process produced a stoichiometric Bi-Sn eutectic alloy.

The fabrication using 10 vol-% sulfuric acid as electrolyte results AAO with uniform distribution of pores, 20 nm in diameter, as shown in the SEM image in Fig. 3.3(a). The wall

thickness is measured as 7 nm, and the pore density*, ~ 8×10^{11} pore · cm^{-2}. Using this AAO as template, Bi-Sn eutectic nanowires are obtained, as shown in Fig. 3.3(b). The size of nanowires is apparently controlled by the small AAO size. Furthermore, after dissolving the AAO using 2 wt-% sodium hydroxide (NaOH) solution for 30 min, the nanowires are freed from the AAO, as shown in Fig. 3.3(c).

Another AAO template, with pores of 70 nm in diameter, is fabricated by using 3 vol-% oxalic acid as electrolyte, as shown in Fig. 3.4(a). The pore wall thickness is found to be near 20 nm, and pore density, ~ 3×10^{10} pore · cm^{-2}. Fig. 3.4(b) shows some nanowires fabricated by this AAO template, which are bundled with AAO. After dissolving the AAO, freed wires are shown in Fig. 3.4(c).

The largest pores, 220 nm in diameter, are produced by 1 vol-% phosphoric acid, as shown in Fig. 3.5(a). The pore-wall thickness is about 100 nm, and the pore density, ~ 1×10^{9} pore · cm^{-2}. The nanowire bundles and freed nanowires are shown in Figs. 3.5(b) and (c) respectively.

Since AAO has a high depth-to-width ratio, the melt barely enters the pores unless a strong force is applied. The applied force may be estimated as the repulsive force exerted by the nanotube [18]:

$$P = -2\gamma\cos\theta / r \tag{1}$$

where P is the applied pressure exerted to the AAO tube; r is the radius of the AAO tube; γ is the surface tension; θ is the contact angle between the melt and the AAO. In our experiment, when the Bi-Sn eutectic melt solidifies on the AAO, the contact angle is 130º. The molar volume of Bi-Sn eutectic is expressed as:

$$V_{\text{Bi-Sn}} = V_{\text{Bi}} \cdot X_{\text{Bi}} + V_{\text{Sn}} \cdot X_{\text{Sn}}, \tag{2}$$

where V and X stand for molar volume and molar fraction respectively. Hence, the Bi-Sn

* To measure the pore density, a large area is selected first, and the count the number of pores within this area. Dividing the pore number to the selected area defines the pore density.

eutectic surface tension γ is expressed as:

$$\gamma_{Bi\text{-}Sn} = \gamma_{Bi} \cdot X_{Bi} + \gamma_{Sn} \cdot X_{Sn}. \quad (3)$$

In the equation, X_{Sn}=0.57, X_{Bi}=0.43, γ_{Sn}= 0.544 N/m, γ_{Bi}= 0.378 N/m. Therefore, $\gamma_{Bi\text{-}Sn}$ is calculated as 0.4726 N/m. According to these parameters, the relationship between the applied pressure (P) and pore diameter r (nm) is plotted in Fig. 3.6. In this work, the AAO sample area is 4 cm^2 and pore diameters are 20 nm, 70 nm and 220 nm respectively. Consequently, if the applied pressure exceeds to 1.5× 10^5 N (37.98 bar), 4.34× 10^4 N (10.85 bar) and 1.38× 10^4 N (3.45 bar), the Bi-Sn melt may be injected into the AAO to form nanowires.

After thoroughly dissolving the AAO template, individual nanowires are deposited onto Cu grids coated with carbon film for TEM studies. The TEM image of typical nanowires, with 220 nm in diameter, is presented in Fig. 3.7. It exhibits alternating darker and lighter contrast. The EDS analysis reveals that the darker area belongs to Bi, and the lighter area belongs to Sn. The image contrast is the scattering absorption contrast, so that the heavier element scatters electrons at larger angles that are filtered out by the objective aperture, and thus it shows a darker contrast. Further, the selected-area electron diffraction (SAED) patterns from the segments, as shown in Fig. 3.7, reveal that within the segments, the Bi and Sn are single crystals.

To ensure our observation, elemental mapping in the STEM model with drift correction is also performed. A high-resolution STEM image of the 220 nm diameter nanowires are shown in Fig. 3.8 (top). An area is selected for the mapping Bi and Sn elements, as shown in the bottom two images in Fig. 3.8. It is evident that alternating segments within the wire are Bi and Sn separately. When the wire diameter is reduced to 70 nm, the STEM images and elemental mapping exhibit similar feature of alternating Bi and Sn pattern but the sections are longer than those found in the 20 nm nanowires, as shown in Fig. 3.9. The STEM image and elemental mapping of the smallest 20 nm nanowires are shown in Fig. 3.10. It is seen that each wire, with length longer than 3 μm, includes only one or two segments within length.

Therefore, these studies have demonstrated that the Bi-43Sn melt injected into the AAO nanochannels still produce the eutectic microstructure during the solidification process, but in a refined size along the wire axis.

3.4 Summary

The nanowires has successfully been fabricated using the eutectic Bi-43Sn alloy, an excellent Pb-free solder material which is currently used in the electronic industry. The Bi-43 wt-% Sn nanowires, with diameters of 20 nm, 70 nm and 220 nm respectively, were fabricated by the hydraulic pressure injection process using anodic aluminum oxide (AAO) as templates. The 20 nm AAO template, with 7 nm pore wall thickness and ~ 8×10^{11} pore · cm^{-2} density, was fabricated by using 10 vol-% sulfuric acid; and the 70 nm diameter AAO, with 20 nm pore wall thickness and ~ 3×10^{10} pore · cm^{-2} density, was fabricated by using 3 vol-% oxalic acid; and finally the 220 nm AAO, with 100 nm pore wall thickness and ~ 1×10^{9} pore · cm^{-2} density, was fabricated by using 1 vol-% phosphoric acid. The samples were characterized by electron microscopy in details. It is found that the nanowires fabricated from this eutectic alloy exhibited novel eutectic microstructure, which composed of alternating segments of single crystalline Bi and Sn along the wire axes. With reducing the nanowire diameter, the segment length increased.

References

[1] H.D. Soloman, *J. Electron. Packaging* **1989**, 111, 75.

[2] S. Knecht, L.R. Fox, *IEEE Trans. Comp., Hybrids, Manuf. Technol.* **1990**, 13, 424.

[3] Z. Mei, D. Grivas, M.C. Shine, J.W. Morris Jr., *J. Electron. Mater.* **1990**, 19, 1273.

[4] A.W. Worcester, J.T. O'Reilly, "*Metal Handbook 10th Edition",* Materials Park, Ohio: ASM International, **1990**, 2, 543.

[5] S. Jin, *JOM* **1993** (July), 13.

[6] S.S. Kang, A.K. Sarkhel, *J. Elec. Mater.* **1994**, 23, 701,

[7] J. Cannis, *Advanced Packaging* **2001**, 8, 33.

[8] S.K. Kang, *JOM* **2001** (June), 16.

[9] D.R. Frear, J.W. Jang, J.K. Lin, C. Zhang, *JOM* **2001**(June), 53, 28.

[10] F.W. Gayle, G. Becka, A. Syed, J. Badgett, G. Whitten, T.Y. Pan, A. Grusd, B. Bauer, R. Lathtop, J. Slattery, I. Anderson, J. Foley, A. Gickler, D. Napp, J. Mather, C. Oslon, *JOM* **2001**(June), 53, 17.

[11] M. Li, K.Y. Lee, D.R. Olsen, W.T. Chen, B.T.C. Tan, S. Mhaisalkar, *IEEE Trans. Electron. Packag. Manuf.* **2002**, 25, 185.

[12] Y.D. Jeon, S. Nieland, A. Ostman, H. Reichl, K.W. Paik, *J. Electron. Mater.* **2003**, 32, 1203.

[13] R.W Chuang, C.C. Lee, *Thin Solid Film* **2002**, 414, 175.

[14] C.A. MacKay, W.D. Von Voss, *Mater. Sci. and Technol.* **1985**, 1, 240.

[15] A.P. Alivisatos, *Science* **1996**, 271, 933.

[16] M. Law, J. Goldberger, P.D. Yang, *Annu. Rev. Mater. Res.* **2004**, 34, 83.

[17] C.A. Huber, T.E. Huber, M. Sadoqi, J.A. Lubin, S. Manalis, C.B. Prater, *Science* **1994**, 263, 800.

[18] Z.B. Zhang, J.Y. Ying, M.S. Dresselhaus, *J. Mater. Res.* **1998**, 13, 1745.

[19] S.B. Cronin, Y.M. Lin, O. Rabin, M.R. Black, J.Y. Ying, M.S. Dresselhaus, P.L. Gai, J.P. Minet, J.P. Issi, *Nanotechnology* **2002**, 13, 653.

[20] G. Sauer, G. Brehm, S. Schneider, K. Nielsch, R.B. Wehrspohn, J. Choi, H. Hofmeister, U. Gosele, *J. Appl. Phys.* **2002**, 91, 3243.

[21] S.B. Cronin, Y.M. Lin, O. Rabin, M.R. Black, G. Dresselhaus, M.S. Dresselhaus, P.L. Gai, *Microsc. Microanaly.* **2002**, 8, 58.

[22] J.G. Wen, J.Y. Lao, D.Z. Wang, T.M. Kyaw, Y.L. Foo, Z.F. Ren, *Chem. Phys. Lett.* **2003**, 372, 717.

[23] Y.J. Zhang, H. Ago, J. Liu, M. Yumura, K. Uchida, S. Ohshima, S. Iijima, J. Zhu, X.Z. Zhang, *J. Crystal Growth* **2004**, 264, 363.

[24] S.T. Kao, J.G. Duh, *J Electron Mater.* **2004**, 33, 1445.

[25]L.Y. Hsiao J.G. Duh, *J. Electrochem. Soc.* **2005**, 152, J105.

[26] Z.X. Ye, H. Zhang, H.D. Liu, W.H. Wu, Z.P. Luo, *Nanotechnology* **2008**, 19, 085709.
[27] W. Zhang, Z.Q. Liu, K. Furuya, *Nanotechnology* **2008**, 19, 135302.
[28] L. Liu, W. Lee, Z. Huang, R. Scholz, U. Gosele, *Nanotechnology* **2008**, 19, 335604.
[29] C.C. Chen, Y. Bisrat, Z.P. Luo, R.E. Schaak, C.G. Chao, D.C. Lagoudas, *Nanotechnology* **2006**, 17, 367.
[30] Y. Bisrat, Z.P. Luo, D. Davis, D. Lagoudas, *Nanotechnology* **2007**, 18, 395601.
[31] Metallurgy Division, National Institute of Standards and Technology (http://www.metallurgy.nist.gov/phase/solder/bisn.html)
[32] C.C. Chen, J.H. Chen, C.G. Chao, *Jpn. J. Appl. Phys.* **2005**, 44, 1529.
[33] Z.P. Luo, *Acta Mater.* **2006**, 54, 47.

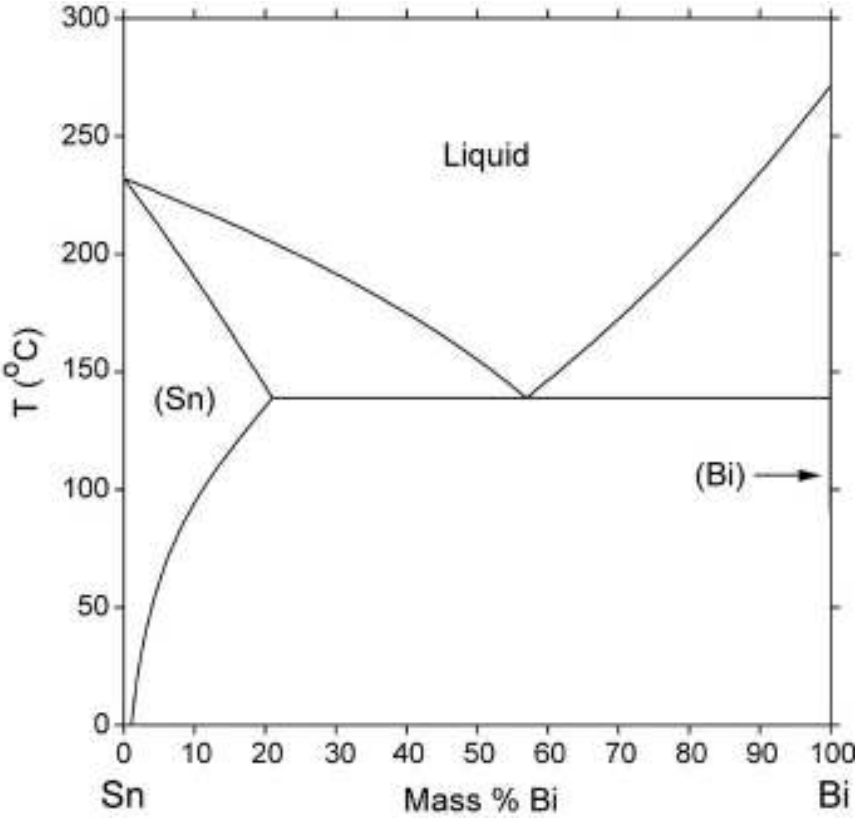

Figure 3.1 Binary Bi-Sn phase diagram [31].

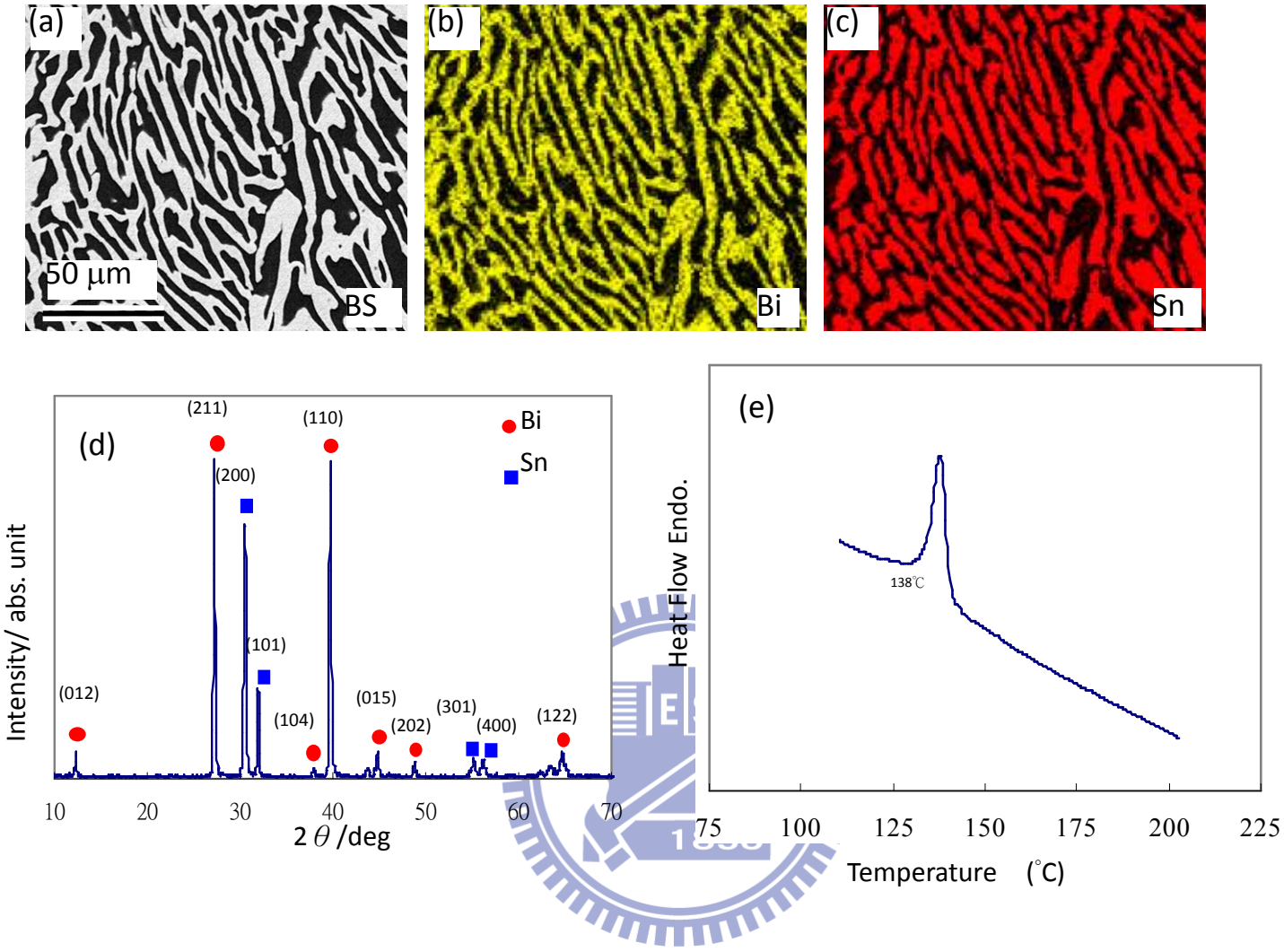

Figure 3.2 Characterization of starting material, the Bi-Sn bulk eutectic alloy. (a) Back-scattered SEM image of lamellar structure; (b) EDS mapping of Bi; (c) EDS mapping of Sn; (d) XRD spectrum showing purely Bi and Sn peaks; (e) DSC spectrum.

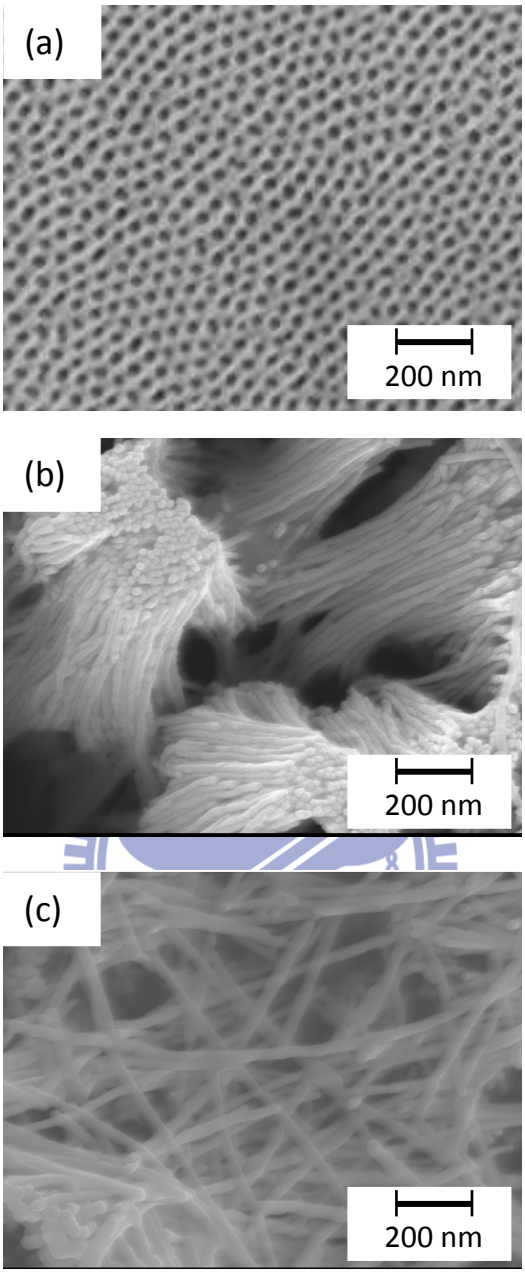

Figure 3.3 SEM images of (a) AAO template with 20 nm pore size, (b) 20 nm Bi-Sn nanowires bundles, and (c) freed 20 nm nanowires.

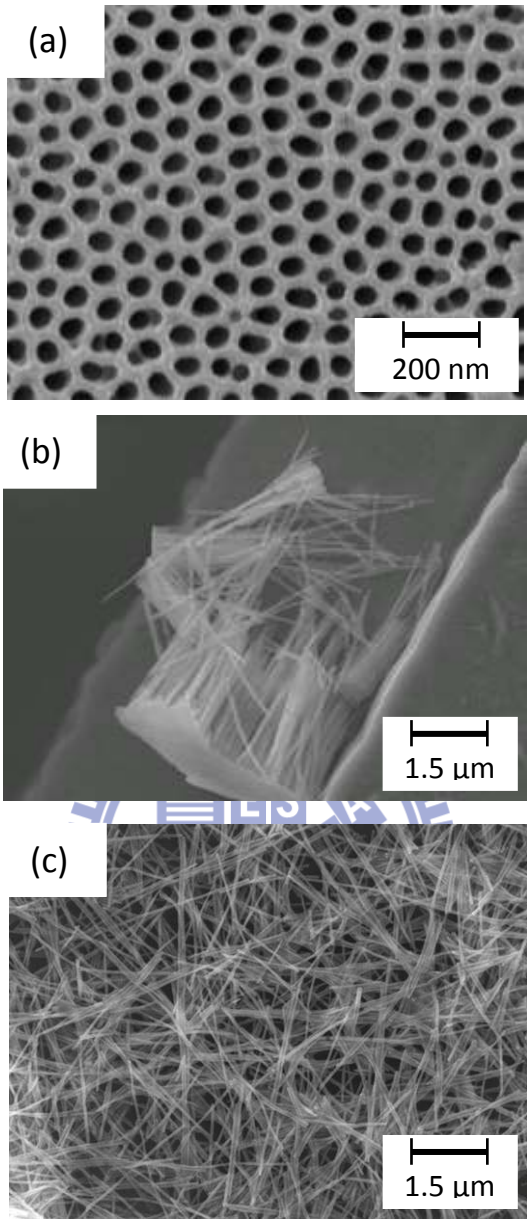

Figure 3.4 SEM images of (a) AAO template with 70 nm pore size, (b) 70 nm Bi-Sn nanowires bundles, and (c) freed 70 nm nanowires.

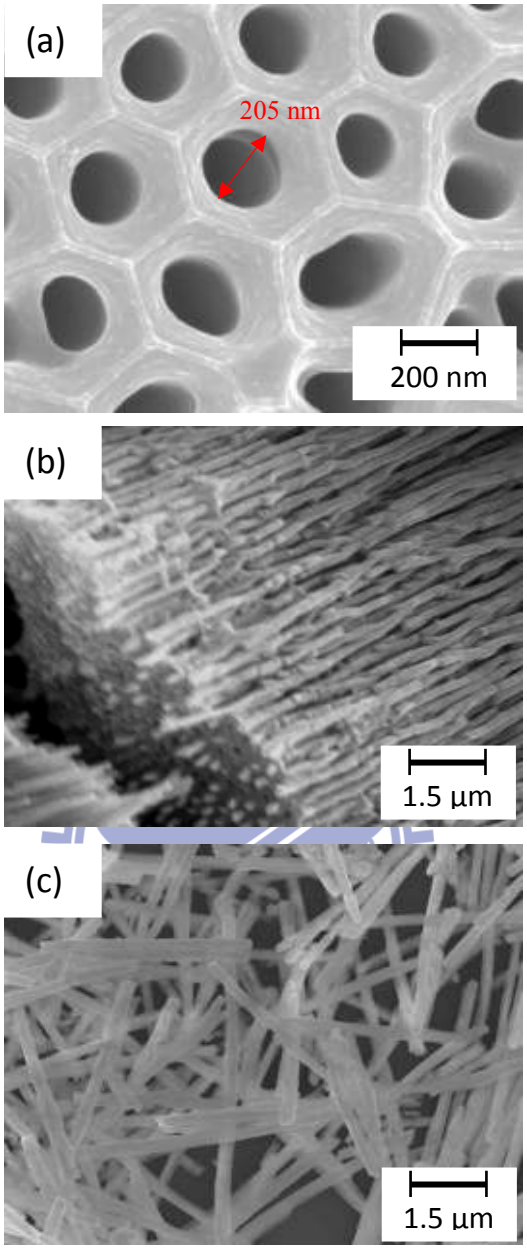

Figure 3.5 SEM images of (a) AAO template with 220 nm pore size, (b) 220 nm Bi-Sn nanowires bundles, and (b) freed 220nm nanowires.

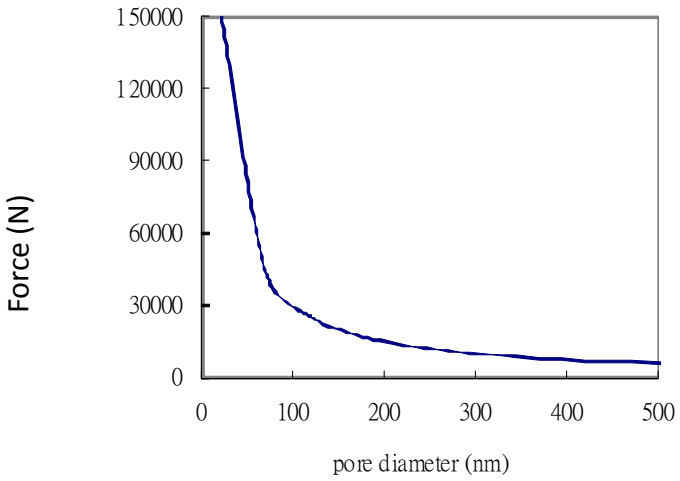

Figure 3.6 Calculation of the applied pressure as a function of the pore diameter of AAO for the experimental alloy.

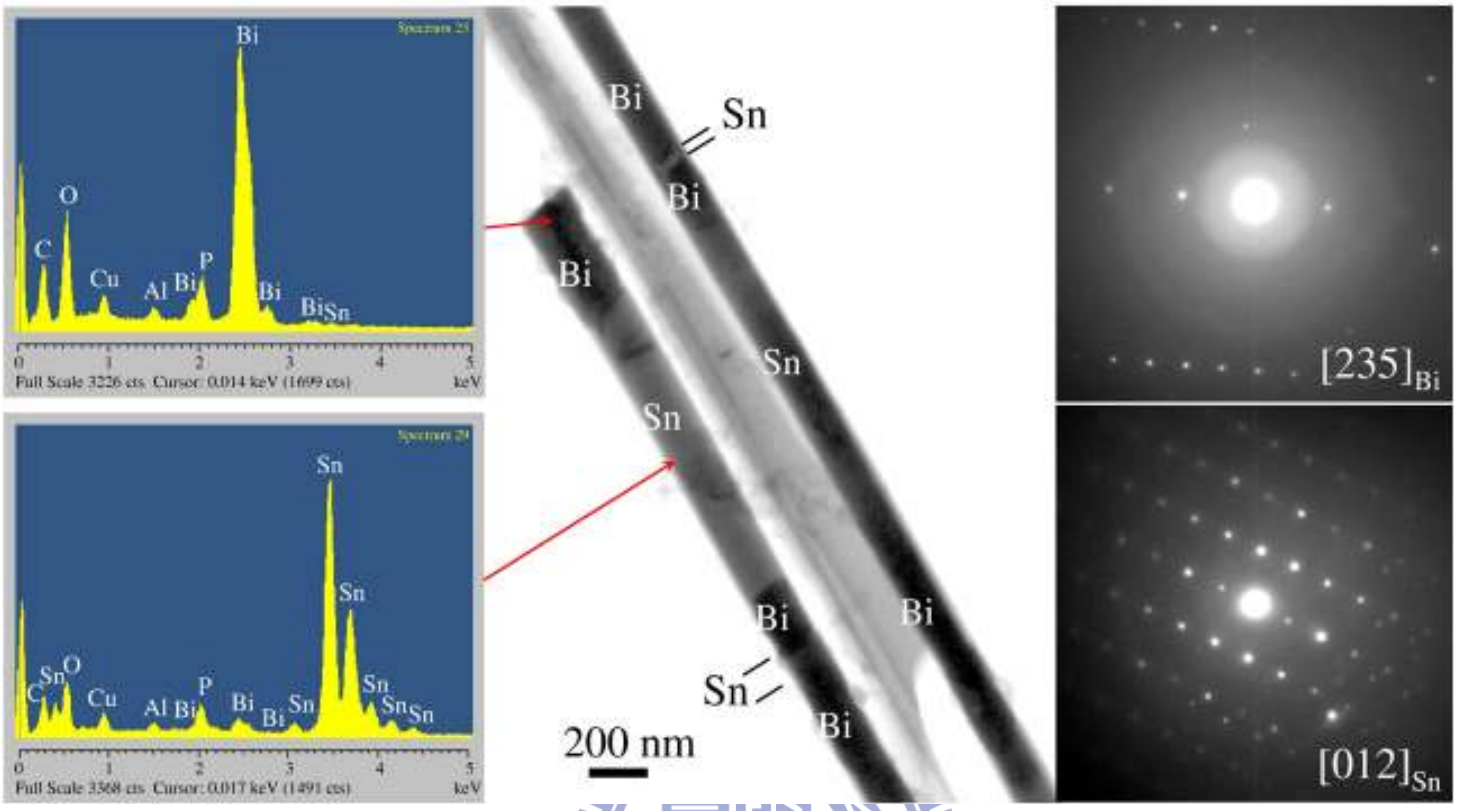

Figure 3.7 TEM image and analyses of the 220 nm Bi–Sn eutectic nanowire.

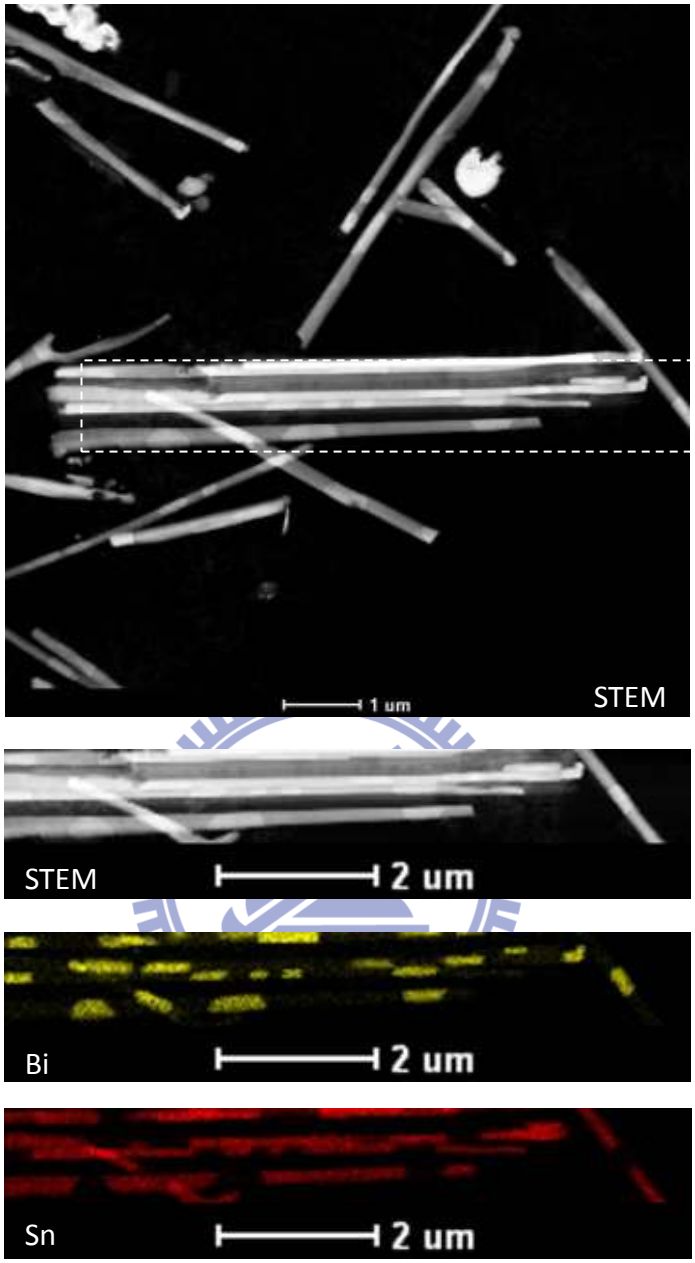

Figure 3.8STEM image and the elemental mapping from the framed area of the 220 nm Bi-Sn eutectic nanowire.

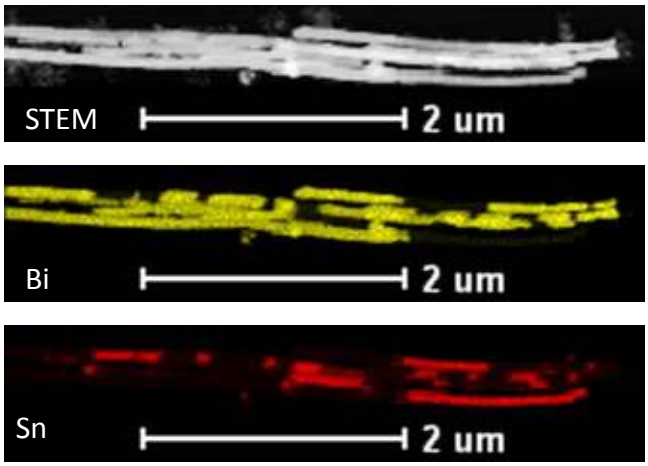

Figure 3.9STEM image and elemental mapping of the 70 nm Bi-Sn eutectic nanowire.

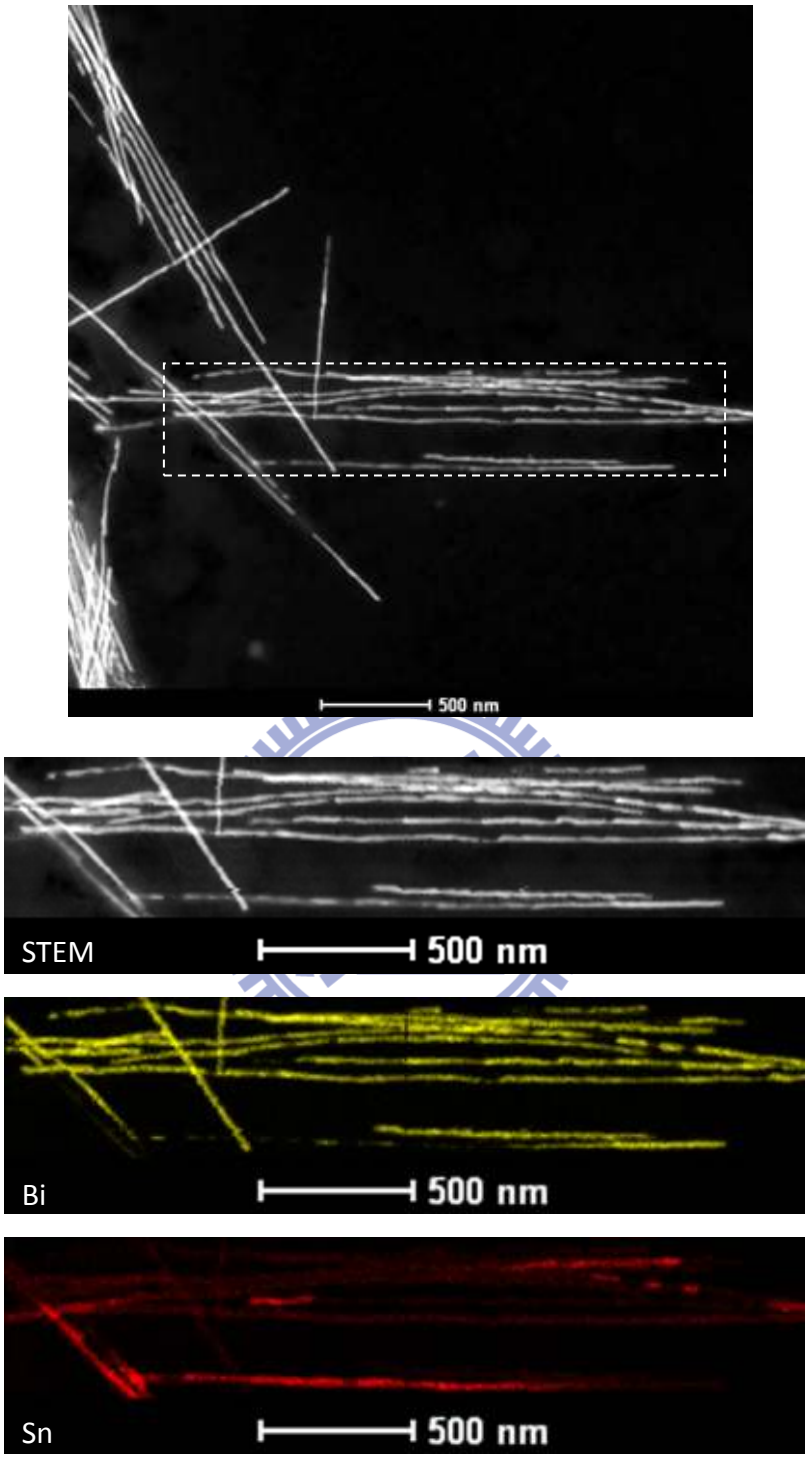

Figure 3.10 STEM image and elemental mapping from the framed area of the 20 nm Bi-Sn eutectic nanowire.

PART II: Solidification –

Chapter 4 Novel Morphology and Solidification Behaviors of Eutectic Bismuth-Tin (Bi-Sn) Nanowires

4.1 Background and Motivation

Solid metallic nanowire is a one-dimensional material. It has been exploited for a wide range of applications that take advantage of their large aspect ratio (length/diameter). Recently, fabricating nanowires by ion deposition or non-lightgraphic methods are emphasized in literature [1-5]. The ion deposition methods such as, electrodeposition [6], metalorganic vapor-phase epitaxy [7], thermal evaporation [8-10], thermal decomposition [11], physical vapor deposition (PVD) [12], and chemical vapor deposition (CVD) [13] are famous for nanowires fabrication. However, there are some problems in nanowires formed from ion deposition. For example, high cost of instrument; low efficiency of forming nanowires; the conditions should be controlled carefully; difficult to control the nanowires composition in the stoichiometry; difficult to make alloy nanowires; and the catalyst always reduced the purity of nanowires. Metal casting has been used in industry for thousands in the world. The database of experiences and conditions on casting were created completely. Therefore, combine the traditional process with nano-technology is helpful for cutting down the cost down of nanowire fabrication.

Understanding the solidification behavior and the formation of alloys can help to recognize the mechanical properties of cast products and to gain expected ones through particular processes. Since 1940s, much effort was constantly invested in establishing this fundamental knowledge [14, 15]. As the development of industry progressed toward

semiconductors, such basic researches did not suspend; on the contrary, they extent to the solders and even the arresting lead-free issue [16-22]. Seeking substitution solders with various elements for specific purposes continued another research trend [23, 24].

Among those substitution materials for Pb-based solders, the eutectic Bi43-Sn57 alloy was regarded as a potential one on fuse products and low temperature applications. Bi43-Sn57 alloy also performs some more advantages [25-27] except for low temperature; therefore, Bi-Sn system is always the popular topic no matter in solid or liquid phase from 1940s to the present. Reviewing those literatures, most investigations referred to its macro-properties or procedures of bulk Bi-Sn alloy, and only a small number was focused on submicron- or nano-scaled behaviors or theories. Here, a template-assisted method [28] was utilized to fabricate the eutectic Bi43-Sn57 alloy nanowire, which might retain more characters of bulk material than those common Bottom-Up processes; as expected an unusual and novel microstructure was observed. This phenomenon differs greatly from bulk eutectic Bi-Sn alloy; thus, a model of solidification process is cited to explain how the microstructure occurred.

To talk about the crystal structure of an alloy, we might look back upon the solidification processes to clarify its causes. The most convenient approach to the understanding of solidification phenomena is to consider them in terms of the macroscopic properties of materials, such as temperature, latent heat, composition, and surface free energy, and to consider their influences separately [29-31]. In most engineering alloys solidify over a range of temperature rather than at a discrete melting point. Therefore, a uniform liquid alloy under constant cooling rate could just be thought of the effects caused by the fractional variation of compositions through the entire solidification.

Solidification of most substances from their melt is closely approximated by the assumption of equilibrium at the interface during growth. That is, there may be large concentration gradients in the solid and liquid during solidification and the transporting barrier of atoms across the interface must be negligible. When solidification is occurring at

temperature T, the condition of equilibrium at the interface defines the liquid and solid compositions at the interface C_L and C_S. Figure 4.1 shows the solidification of an alloy with equilibrium at the interface, which Fig. 4.1(a) and Fig. 4.1(b) are the phase diagram and composition profile. In addition, the equilibrium partition ratio, K, is defined as [32]:

$$K = C_S / C_L \quad (1)$$

In most particular cases, the solute distribution within the solid is assumed that no diffusion occurs. Another critical assumption under rapid solidification process is that diffusion is limited in the liquid and there is no convection. For these two terms, the composition profile can be redrawn as Fig. 4.2.

Here, the fabrication of Sn-Bi alloy nanowire by die-casting process is reported. Nanowires of alloy were fabricated using hydraulic force process. The nanowires were formed from melt of alloy, directly. The composition of nanowires can be controlled. Additionally, for the instrument, it is cheaper than the ion depositions. Also, nanowires with well-defined morphology and high surface area were fabricated and the micro-structures were discussed.

4.2 Experimental Procedures

The eutectic bismuth-tin (Bi-Sn) nanowires used for this study were synthesized by a template-assisted vacuum hydraulic pressure injection process, and more details about that apparatus could refer to the literature of our laboratory [28]. Bi-Sn eutectic bulk alloy was prepared using the vacuum melting method firstly. The anodic aluminum oxide (AAO) with an average pore diameter of 220 nm, which was fabricated through anodizing an aluminum foil in phosphoric acid, served as the mold for the injection procedure. Then, remove the ceramic template, and the nano-structured Bi-Sn eutectic alloy was gained.

The characterizations of Bi-Sn nanowires were examined by scanning electron

microscopy (SEM, JEOL 6500F FESEM and FEI Quanta 600 FESEM), energy dispersive spectroscopy (EDS), transmission electron microscopy (TEM, JEOL 2010), and scanning TEM (STEM, FEI Tecnai G^2 F20). Standards of 6*H* SiC single-crystal lattice fringes [33] and a cross-line grating replica were used to calibrate the TEM/STEM images.

4.3 Results and Discussion

A bulk Bi-Sn material of eutectic stoichiometric composition was fabricated by a vacuum smelting process; moreover, the examinations reported its characteristic melting point of 139℃ and the lamellar microstructure, as shown in Fig. 4.3. In our results, the alloy was confirmed with its properties, and then was injected into AAO template to synthesize submicron-scaled Bi-Sn eutectic wires. And then remove AAO by a chemical dissolved process which the eutectic Bi-Sn nanowires could be obtained. Figure 4.4 is the SEM images of Bi-Sn nanowire bundle; a slightly segmental appearance could be observed in the insert image. In Fig. 4.5, the high-resolution back-scattered SEM images (BEI), a global segmental structure was presented, and the magnified image showed a banded composition distribution in Fig. 4.5(b). A TEM was utilized to analyze what caused this variation. Figure 4.6 shows the TEM morphology and mapping images of submicron-wires bundle. According to the mapping information, the banded appearance was resulted from distinct compositions. In addition, a tendency is that the Bi segment occupied a shorted fraction and Sn did longer relatively. This sequence of eutectic microstructure along its growth direction is different form the typical Bi-Sn eutectic, which is arranged perpendicularly to the liquid-solid interface.

The interlamellar interface was approximately normal to the mean solid-liquid interface could be explained through the solidification behavior of bulk eutectic alloys, which was shown experimentally by Straumanis and Braaks [34, 35] and confirmed by Winegard et al. [36]. When the solidification was restricted within nanoscale, solutes would not diffuse to the

adjacent liquid perpendicularly to form lamellar structure as usual. This one-dimension nanostructure restrained the diffusion and forced it to organize along wire axis; thus, the segmental order was observed as shown in Fig. 4.5.

The solute-ejecting behavior and distribution coefficient, k_o, can be used to describe further. Tammann [37] reported that while one phase is forming from a eutectic liquid, the adjacent liquid is enriched in the other component and whenever this enrichment reaches a critical value, the other phase forms as a layer over the first one. That is, the two phases of a lamellar eutectic were separated out alternatively, and such phenomenon also could be discovered in this study. In other words, while the concentration enrichment alternated between Bi and Sn, the character of liquid also switched between hypereutectic and hypoeutectic. Reviews the Fig. 4.5(b) again, Sn sections are several times longer than Bi ones. In a uniform eutectic system, the critical enrichment values of two specific components could be assumed the equal. The shorter precipitate formed, the faster critical enrichment reached. Therefore, the solute-ejecting rate of Sn from the Bi solid is several times faster than the opposite solidification does.

The equilibrium distribution coefficient, so-called partition coefficient, is the ratio of concentrations of the solid and the liquid in equilibrium, and is convenient to describe the salient feature of these solid-liquid equilibrium relationships. Take the solidification at eutectic Bi-Sn composition as an example, as points A and B in Fig. 4.7. Solidification might begin from some phase on a temperature below its melting point and above the eutectic point; thus, the starting point is assumed as 200℃, suitable for both cases, and the cooling rate is uniform. If the temperature cooled down to 170℃, the distribution coefficients of Bi and Sn were 0.1 and 0.33 respectively, which indicates once more that under the same solidification conditions Bi phase segregation would consume fewer solute and eject more into the adjacent liquid. That is, the Bi solidification would cause the adjacent liquid enrichment easily. Because of the alternate enrichments and the difference in distribution coefficient, the

variation in segmental lengths was observed.

From the lever rule, the liquid-to-solid ratios of A and B points are 2 and 0.45. While Bi proceeded solidification, just one third compositions were transformed to solid and others were ejected into the neighboring liquid. Tin solidification comparatively utilized an approximate double in solidification.

4.4 Summary

A novel segmental appearance was observed in 200 nm eutectic Bi-Sn nanowires which fabricated by a template-assisted vacuum hydraulic pressure injection process. The one-dimension submicron-structure of AAO template limited the banded wire morphology to arrange along its axis that might result from the alternate enrichments between bismuth and tin in liquid phase. The distribution coefficient and lever rule were utilized to describe the approximately triple difference of length. Consequently, when the binary lamellar eutectic was trapped in a submicron-scaled structure, the different solidification behavior and the enrichment alternations between hypereutectic and hypoeutectic would bring about this particular appearance.

Referencs

[1] X.F. Wang, L.D. Zhang, J. Zhang, H.Z. Shi, X.S. Peng, M.J. Zheng, J. Fang, J.L. Chen, B.J. Gao, *J. Phys. D* **2001**, 34, 418.

[2] H. Yu, P.C. Gibbons, W.E. Buhro, *J. mater. Chem.* **2004**, 14, 595.

[3] T. Hirata, N. Satake, G.H. Jeong, T. Kato, R. Hatakeyama, K. Motomiya, K. Tohji , *Appl. Phys. Lett.* **2003**, 83, 1119.

[4] Mi. Tian, J. Wang, J. Snyder, J. Kurtz, Y. Liu, P. Schiffer, T.E. Mallouk, M.H.W. Chan, *Appl. Phys. Lett.* **2003**, 83, 1620.

[5] S.H. Jo, J.Y. Lao, Z.F. Ren, R.A. Farrer, T. Baldacchini, J.T. Fourkas, *Appl. Phys. Lett.* **2003**, 83, 4821.

[6] C. Ji, P.C. Season, *Appl. Phys. Lett.* **2002**, 81, 4437.

[7] W.I. Park, D.H. Kim, S.W. Jung, G.C. Yi, *Appl. Phys. Lett.* **2002**, 80, 4232.

[8] B.D. Yao, Y.F. Chan, N. Wang, *Appl. Phys. Lett.* **2002**, 81, 757.

[9] J.Y. Lao, J.G. Wen, Z.F. Ren, *Nano Lett.* **2002**, 2, 1287.

[10] D. Banerjee, J.Y. Lao, D.Z. Wang, J.Y. Huang, Z.F. Ren, D. Steeves, B. Kimball, M. Sennett, *Appl. Phys. Lett.* **2003**, 83, 2061.

[11] C. Xu, G. Xu, Y. Liu, G. Wang, *Solid State Commun.* **2002**, 122, 175.

[12] A. Moroz, *Phys. Rev. Lett.* **1999**, 83, 5274.

[13] Z.Q. Liu, Z.W. Pan, L.F. Sun, D.S. Tang, W.Y. Zhou, G. Wang, L.X. Qian, S.S. Xie, *J. phys. Chem. solids* **2000**, 61, 1171.

[14] E. Scheil, *Z. Metallk.* **1942**, 34, 70.

[15] W. G. Pfann, *Trans. AIME* **1952**, 194, 747.

[16] W. Yang, R.W. Messler, *J. Electron. Mater.* **1994**, 23, 765.

[17] J. Wanqi, M. Dong, *J. Cryst. Growth* **1995**, 156, 467.

[18] C.C. Lee, R.W. Chuang, D.W. Kim, *Mater. Sci. Eng. A* **2004**, 374, 280.

[19] O.G. Shpyrko, A. Grigoriev, R. Streitel, *Phys. Rev. Lett.* **2005**, 95, 106103.

[20] V. Bhattacharya, K. Chattopadhyay, *Mater. Sci. Eng. A* **2007**, 449-451, 1003.

[21] F.Y. Hung, C.J. Wang, S.M. Huang, L.H. Chen, T.S. Lui, *J. Alloys Compd.* **2006**, 420, 193.

[22] J. Zhou, Y. Sun, F. Xue, *J. Alloys Compd.* **2005**, 397, 260.

[23] K . Suganuma, *Current Opinion in Solid State and Materials Science* **2001**, 5, 55.

[24] R.A. Islam, B.Y. Wu, M.O. Alam, Y.C. Chen, W. Jillek, *J. Alloys Compd.* **2005**, 392, 149.

[25] S.A. Cho, J.L. Ochoa, *Metall.Mater. Trans. B* **1997**, 28, 1081.

[26] C.C. Lee, C.J. Wang, G.S. Matijasevic, *IEEE Trans. Components, Hybrids, Manuf. Technol.* **1991**, 14, 407.

[27] H. Chen, Z. Li, Z. Wu, Z. Zhaung, *J. Alloys Compd.* **2004**, 394, 282.

[28] C.C. Chen, Y. Bisrat, Z.P. Luo, R.E. Schaak, C.G. Chao, D.C. Lagoudas, *Nanotechnolygy* **2006**, 17, 367.

[29] M.C. Flemings: "*Solidification Processing,*" International Edition, McGraw-Hill Book Company, Singapore, **1974**.
[30] E. Cadirli, H. Kaya, M. Gunduz, *J. Alloys Compd.* **2007**, 431, 171.
[31] J.M. Song, T.S. Lui, Y.L. Chang, L.H. Chen, *J. Alloys Compd.* **2005**, 403, 191.
[32] B. Chalmers : "*Principles of Solidification,*" John Wiley & Sons Inc., New York, **1964**.
[33] Z.P. Luo, *Acta Mater.* **2006**, 54, 47.
[34] M. Straumanis, N. Braaks, *Z. Phys. Chem.* **1935**, 29, 30.
[35] M. Straumanis, N. Braaks, *Z. Phys. Chem.* **1937**, 37, 38.
[36] W.D. Winegard, S. Majka, B.M. Thall, B. Chalmers, *Can. J. Chem.* **1957**, 29, 320.
[37] G. Tammann, Text book of Metallography, Chemical Catalogue Co., New York, **1925.**
[38] Metallurgy Division, National Institute of Standards and Technology (http://www.metallurgy.nist.gov/phase/solder/bisn.html)

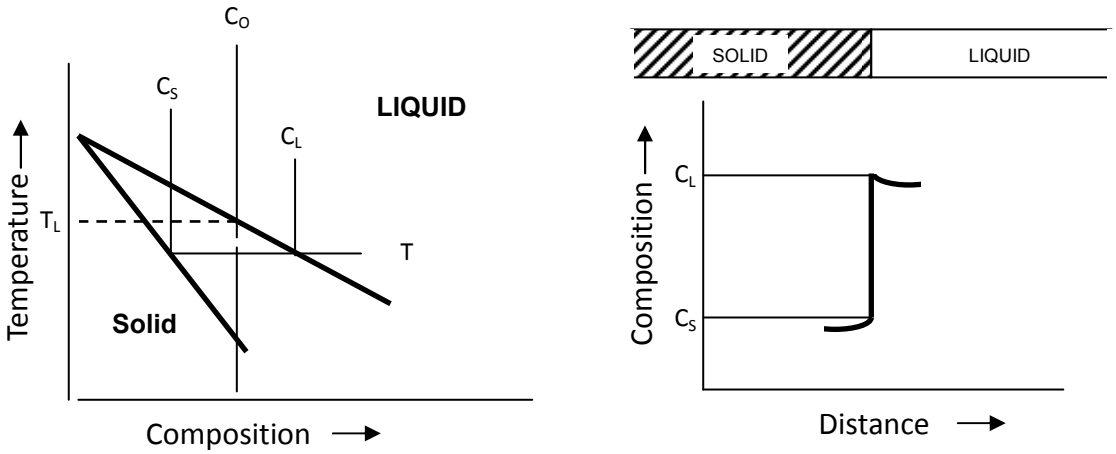

(a) (b)

Figure 4.1 Solidification of an alloy with equilibrium at the liquid-solid interface. (a) Phase diagram; (b) composition profile across the interface [32].

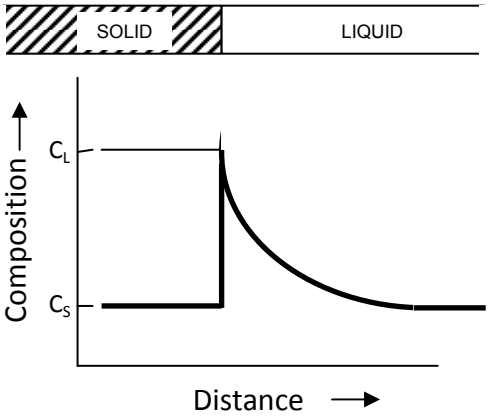

Figure 4.2 Composition profile in solidification with limited liquid diffusion and no convection in solid.

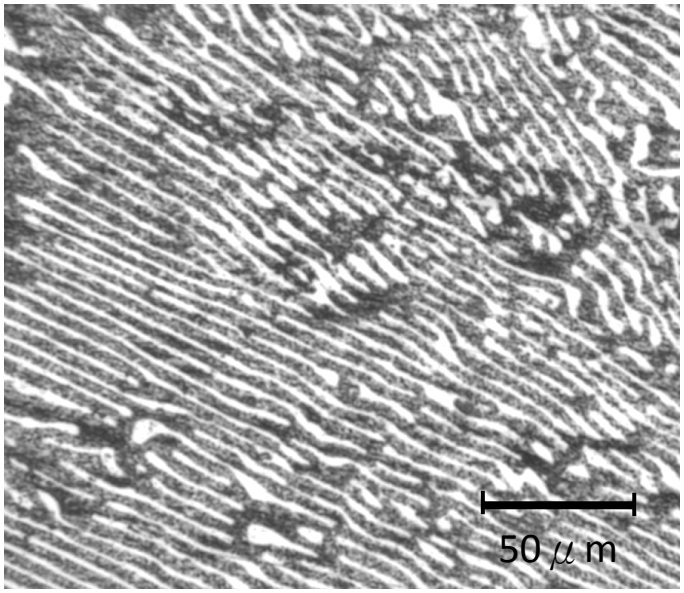

Figure 4.3 Typical OM image of casted bulk Bi-Sn eutectic material with a lamellar microstructure.

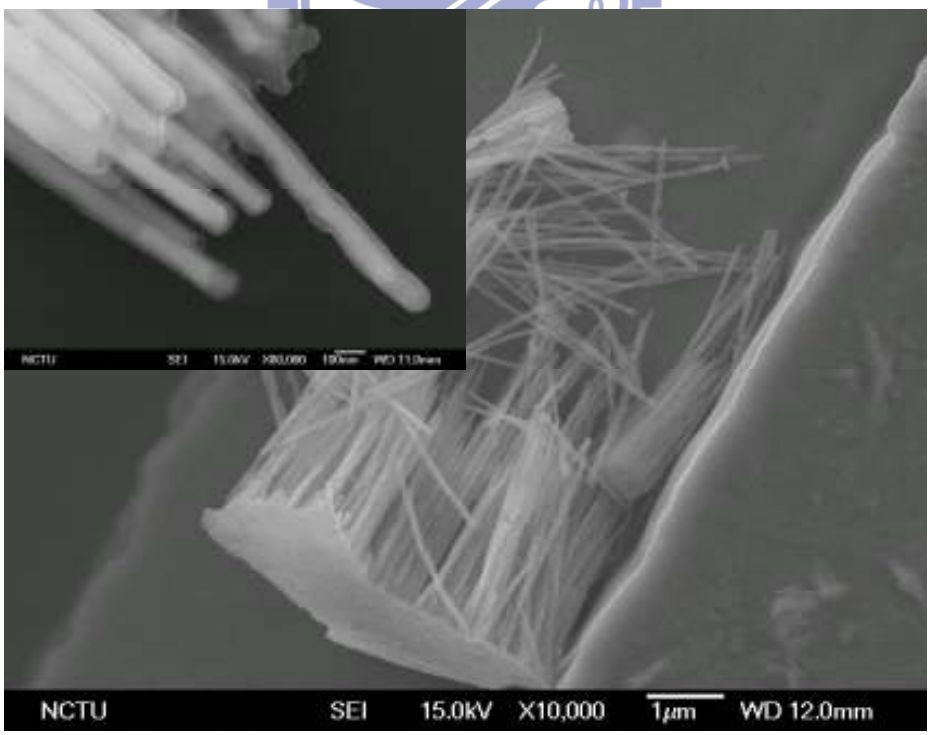

Figure 4.4 SEM images of fabricated Bi-Sn nanowire bundle and magnified image of a part. (Insert)

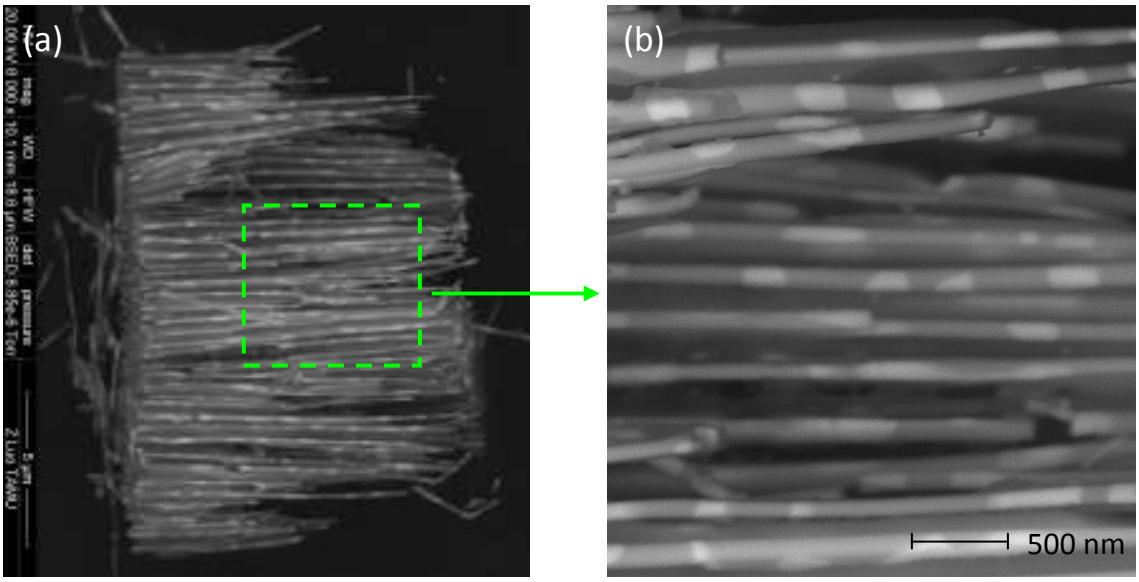

Figure 4.5 High-resolution back-scattered SEM images of Bi-Sn eutectic nanowire (a) a large overview of a nanowire bundle; (b) magnified image showing the banded eutectic structure.

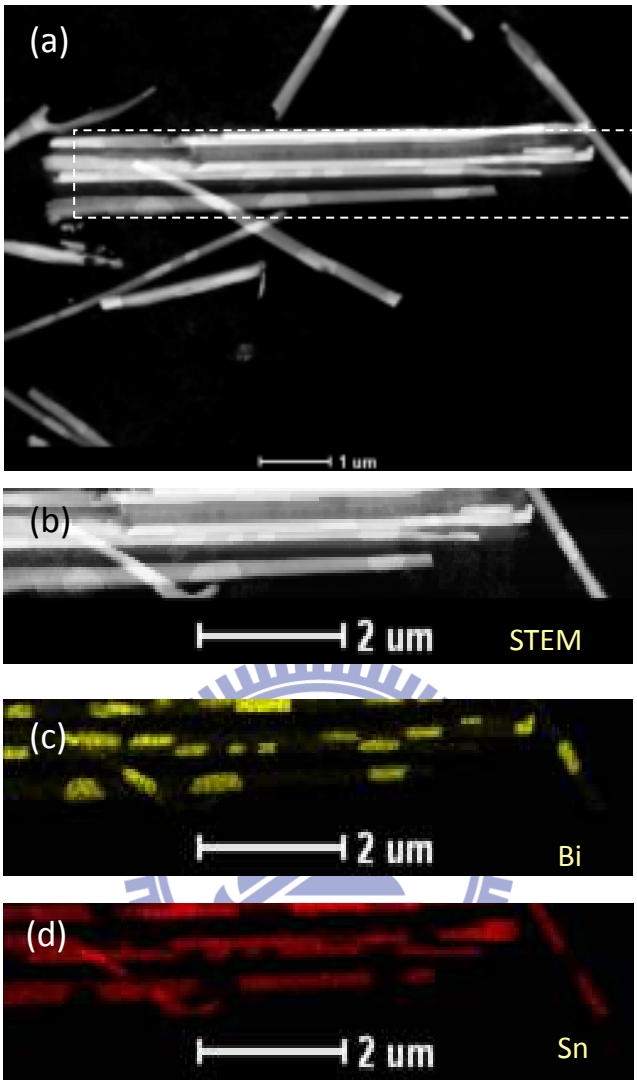

Figure 4.6 STEM image and the element mapping from the framed area of the 220 nm Bi-Sn eutectic nanowires.

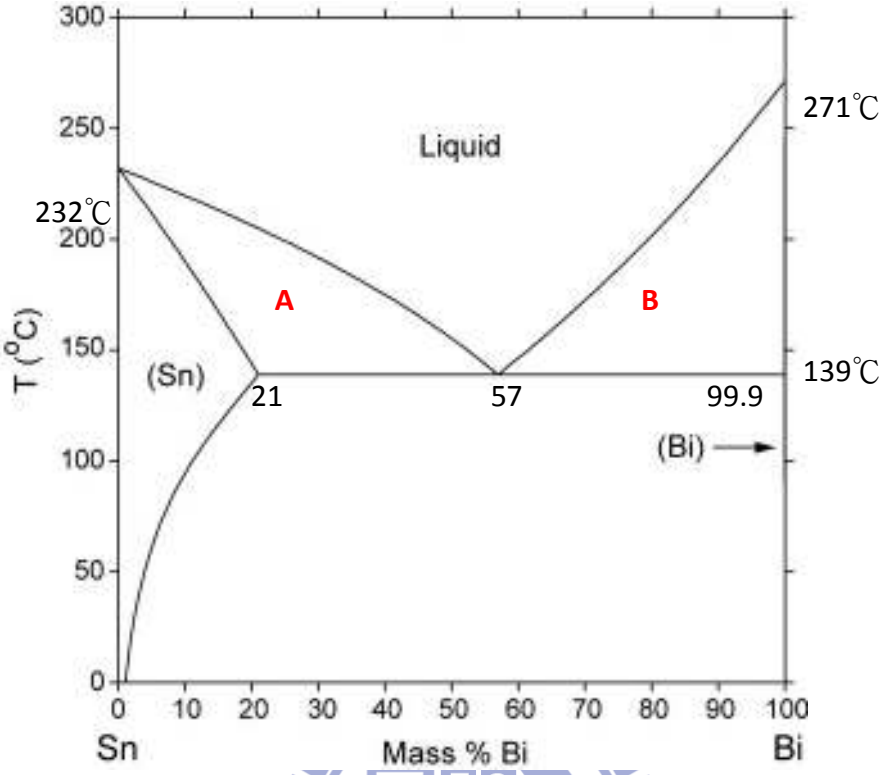

Figure 4.7 Example of hypoeutectic, *A*, and hypereutectic, *B*, composition points in a binary Bi-Sn phase diagram [38].

Chapter 5 The size effect on solidification in eutectic bismuth-tin (Bi-Sn) nanowires by in-situ reheating processes

5.1 Background and Motivation

The manufacturing of one-dimensional nano-materials via the template-assisted methods has been widely combined with various synthesis processes [1-6]. Among these methods, the vacuum hydraulic pressure injection method has been used with metal and alloy casting processes, a method that has been studied and applied practically macroscopically for several centuries. When casting is introduced to a new field, previous efforts on fundamental understanding can help us clarify the formation mechanism and shorten the consolidation stage. In our laboratory, the anodic aluminum oxide (AAO) template-assisted casting processes, especially the recent hydraulic pressure injection method [7-9], have been under development for several years [10-12]. Unlike vapor deposition processes or chemosynthesis, when a stoichiometric bulk material is produced, the casting does not change the composition ratio of alloys.

One-dimensional nanostructured materials exhibit distinctive properties differ from their bulk materials counterparts in electric, magnetic, optical, physical and chemical aspects [13-15]. In addition to the above-mentioned characteristics, it is recently found a novel microstructure of bismuth-tin (57 wt.% Bi-43 wt.% Sn) eutectic alloy nanowires produced by the vacuum hydraulic pressure injection process [8, 9]. A bulk Bi-Sn eutectic alloy is of a lamellar structure [16]. As the Bi-Sn eutectic melt was injected into the AAO nanochannels, the lamellar microstructure forms along the wire axes in a confined space during the solidification process.

Hunt, an author of the JH model [17], reported that “in the physical sciences, the details of pattern formation are not well understood [18].” That is, the observed solidification structures are never perfectly regular, and only a small range of spacing is always present on a directionally grown lamellar structure because of the fluctuation in growth conditions. We have also attempted to present a model to explain a particular solidification condition during the injection process [9]. Understanding the solidification behavior and the formation of alloys can help us to recognize the mechanical properties of cast products and to gain the expected properties through particular processes. To gather more information on the axial-arranged eutectic nanostructure, the re-melting and solidification procedures were investigated by *in situ* high-resolution transmission electron microscopy (TEM). The size effects including the differences in solidification and diffusion behaviors are investigated.

5.2 Experimental Procedure

Bulk eutectic Bi-Sn alloy was prepared by a vacuum smelting process using highly pure (99.999 wt. %) raw bismuth and tin [8], and synthesized into eutectic Bi-Sn nanowires via the AAO template-assisted casting process. The Bi-Sn nanowires had diameters of 70 nm and 200 nm, and lengths of a few microns. The details of the vacuum hydraulic pressure injection process have been previously disclosed [3, 19].

The Bi-Sn nanowires were stored in alcohol after they were removed from AAO template by immersing in the chromic acid solution. Individual nanowires were then deposited onto Cu grids coated with carbon support film for TEM studies. The in situ reheating experiments were performed in a JEOL 2010 TEM attached with an energy dispersive spectrometer (EDS) and a Gatan 652 double tilt heating holder that can be heated at an adjustable rate The vacuum in the sample area was below 1×10^{-6} Torr during the reheating [20-22].

An outline of the fabrication and solidification procedure of the Bi-Sn nanowires in AAO membranes is presented in Figs. 5.1(a)-(c). A schematic illustration of the reheating process is shown in Figs. 5.2(a)-(c) to describe the distinction between these solidification processes, including the heating, holding and cooling processes. In the injection process, the cooling results in a directional solidification along the wire axis. On the other hand, in the reheating process, the heating source is located at the bottom of the sample. Those figures illustrate the distinct features of the two systems used in our experiments.

5.3 Results and discussion

In the solidification of a metal, the growth of a single crystal requires a planar liquid-solid interface and a solidification direction anti-parallel to the heat flow. In other words, a sufficiently high thermal gradient and a sufficiently low growth rate can both prevent the formation of cells and dendrites and result in planar front growth. The values of specific ratio G/V represent a constancy of microstructure (planar, cellular, columnar, and equiaxed dendritic), where G is the temperature gradient at the interface, and V, the growth rate, represents the speed of movement of the solid/liquid interface. The product of G and V is equivalent to the cooling rate, which controls the scale of microstructures [16].

The Reynolds number (Re) can help determining the type of flow in a tube. If the Re is below 2100, the fluid will have a laminar flow. At a Re above 2100, the fluid will have a transitional or a turbulent flow. Within a nanotube, the dimension will confine the fluid to a laminar flow only [23]. Since the melting fluid in Bi-Sn nanowires has a laminar flow, the convectional variables can be evaluated by the following formula:

$$V = \frac{D^2 \Delta P}{32 \mu l} \tag{1}$$

where V is the velocity of flow; D is the diameter of tube; $\triangle P$ is the pressure difference;

l is the length, and μ is viscosity of the fluid. In these reheating experiments, the environment and fluid are fixed, so the velocity is only proportional to the square of the nanotube diameter. When the eutectic Bi-Sn alloys are melted within a 200 nm nanowire, the effect of convection is about 8 times stronger than that in a 70 nm nanowire.

In this case, it is applicable to assume that the temperature gradient throughout the wires is in the steady stable condition. The temperature difference between the two ends of the injected wires is about 200 K. The length of the wire is 10 μm and the total cooling time is 5 min. Hence, G and V could be estimated to be 2×10^{7} K/m and 3.33×10^{-8} m/s, respectively. The high G/V value ($\sim 6 \times 10^{14}$) and the directional solidification along wire axes demonstrates that the solidification has a planar interface, and the nanowires are observed to be of single crystal structures, similar to the results of Pb nanowires [24].

Comparing with our previous results [8], porous AAO membranes with two average pore diameters of 80 and 200 nm were used as templates to produce Bi-Sn eutectic nanowires. These nano-scaled materials showed a similar phenomenon in that the two phases of eutectic Bi-Sn were arranged alternatively along their wire axes and the cooling direction. On the other hand, the lamellar arrangement of bulk alloys is perpendicular to the solid/liquid interface. In addition, each segment of nanowire was a single crystal.

Figure 5.3 shows a series of *in situ* TEM images capturing the diffusion motion within a 70 nm eutectic Bi-Sn nanowire at temperatures from room temperature to 150 ℃ (12 ℃ higher than the melting point). In Figs. 5.3(a) and (b), each segment of eutectic microstructure maintained the appearance with distinct interfaces, but defects in the segments underwent changes at the temperatures lower than the melting point. The selected electron diffraction patterns of the segments in this nanowire showed a single crystal structure, which agreed with the single crystal structures evaluated by GV value. At the melting point, the diffusion still did not occur evidently, as shown in Fig. 5.3(c). When the reheating temperature was higher than 138 ℃, the diffusion would proceed due to fluid convection. Figure 5.3(d) presents an image

of the nanowire annealed at 150 ℃, showing the disappearance of the phase boundaries. When the temperature continued to increase, the appearances of the nanowires did not change further, even at 200 ℃.

Figure 5.4 shows a TEM image and EDS spectra of Bi-Sn eutectic nanowire at 150 ℃. In this figure, an oxide layer could be observed in Sn segments. The oxide of Sn formed during the removal of the AAO membranes in a mixed acid solution. Similarly, Bi was also oxidized in that solution, but not quite so deeply because of its high stability at room temperature. [25, 26] These oxide layers are a distinctive characteristic of this system and form a core-shell structure enclosing melted alloys in the following reheating processes. When the reheating was performed in TEM, Sn was not oxidized at an oxygen pressure below 5.0×10^{-6} Torr [27]. The phase diagram of bismuth-oxygen also shows that no stable oxide forms in a low-pressure environment [28]. Thus, the oxidation will not continue to consume eutectic alloys during the reheating process in a vacuum environment. The EDS results in Fig. 5.4 show that the composition of Bi-Sn nanowires was fully mixed to the eutectic ratio at 150 ℃, in both Bi and Sn segments. A higher content of Sn in Sn segments resulted in the formation of tin oxides, which did not melt and move during the reheating process.

A series of TEM images of 200 nm eutectic Bi-Sn nanowires during *in situ* reheating is shown in Fig. 5.5. Below the melting point, the appearance exhibited a segmental microstructure. When the temperature reached 138 ℃ or higher, the TEM elemental image contrast of Bi and Sn became blurred. The transition occurred faster than that of 70 nm nanowires, according to the composition profiles. For the diffusion behaviors in a fluid, convection should also be considered. In solidification, convection is usually neglected because in solid only the solute redistribution is of concern, and this convection is neglected in a solid. However, the high mobility and low viscosity of a liquid would influence the solidification and results in such a solid-to-liquid transition during the reheating.

Figure 5.6 is the distribution of compositions with increasing temperature from the local

regions of a nanowire, like the marked locations in Fig. 5.4. According to the Bi-Sn phase diagram [29], Sn will dissolve some of the Bi, but no Sn can be dissolved in Bi. Figure 5.6 (a) shows that the Bi segment maintained a pure Bi composition below 138 ℃, and would reach the eutectic ratio beyond the melting point. The Sn segment exhibited the same behavior, except for the soluble Bi at temperatures below the eutectic point. Furthermore, these phenomena were observed both within the local regions of 70 nm and 200 nm. Although the Bi-Sn eutectic alloys were introduced into nano-scaled sections, each segment still retained the properties of the bulk material in some respects, such as the melting point and solubility, as the result shown in Fig. 5.6(b).

In order to examine the variation of diffusion behaviors, Bi segment at one end of the Bi-Sn nanowires was further selected. Bi regions are represented by a higher contrast under EM and larger differences of composition ratios around the melting point. Figures 5.7(a) and (b) indicate the analyzed positions at the ends of nanowires. The tips of a 200 nm nanowire produced a result which was similar to that in Fig. 5.6(a); the 70 nm nanowire produced a diffusionless phenomenon, shown in Fig. 5.7(c), which is collected from the marked points in Fig. 5.7(a).

Figure 5.8 can be used to illustrate the different diffusion results for those two situations. Figure 5.8(a) and (b) shows the sketch of a single nanowire and the diffusion direction of solutes within it respectively. This schema represents the basis of diffusion from one side or two sides; in other words, these phenomena are the diffusion behaviors of semi-infinite and infinite diffusion system [30]. Depending only on the diffusion effects within a nanochannel, the concentration distribution would be similar to the plots in Fig. 5.8(c). That is, the one-sided diffusion leads to an exponentially decreasing distribution from the solid/liquid interface, while two-sided diffusion makes the distribution well mixed. Compared with the previous results, the difference of composition profiles at the tips in 70 and 200 nm nanowires appears to have resulted from convection. In a 70 nm nanowire, its dimensions will not only

make the movement of solutes difficult, but also reduce the convection effect such that the diffusion behavior at the end tips is limited. With the diameter increased to 200 nm, the restriction lessens.

The results of cooling after *in situ* reheating were recorded. The composition ratios of two nanowires at specific temperatures are shown in Table 1. Up to 170 ℃, the two distinct segments of the 200 nm nanowire revealed results close to the eutectic composition. While cooling to R.T., the two segments were restored to their initial states; that is, some Bi dissolved in the Sn segment, and no Sn dissolved in the Bi. On the contrary, the 70 nm nanowire kept the characteristics of high temperature in both Bi and Sn segments while cooling from the liquid state. In Fig. 5.9, the TEM image, EDS spectra and the selected area electron diffraction patterns show the polycrystalline microstructure within the 70 nm nanowire, which confirms the eutectic composition.

From the illustrations in Figs. 5.1 and 5.2, diffusion along the wire axis appears to cause the enrichment and the ejection of solutes in turn [31]; in this way, nanowire with a segmental microstructure is obtained. The reheating process on the hot plate in TEM would not only eliminate the order of precipitation but also cause the formation of a polycrystalline nanowire due to rapid solidification, as shown in Fig. 5.2(c).

5.4 Summary

In summary, the solidification behaviors of a segmented microstructure within the Bi-Sn eutectic nanowires fabricated by a vacuum hydraulic pressure injection method have been illustrated and clarified. The as-cast nanowires with single-crystalline segments mix well in the eutectic ratio at the temperatures higher than the eutectic point. In 70 nm nanowires, the small size confines the convection in liquid, which results in differences in the microstructure

and composition profiles between 70 and 200 nm nanowires. Moreover, the formation of polycrystalline microstructure within the 70 nm nanowires was not observed in 200 nm wire due to the convection and the diffusion. The directional solidification and the unique core-shell structure produced by this AAO template-assisted method can provide a specific way to synthesize one-dimensional nano-materials.

References

[1] N.I. Kovtyukhov, B.R. Martin, *Mater. Sci. Eng. C* **2002**, 19, 255..

[2] Z. Zhang, J.Y. Ying, M.S. Dresselhaus, *J. Mater. Res.* **1998**, 13, 1745 (1998).

[3] C.C. Chen, C.G. Kuo, J.H. Chen, C.G. Chao, *Jpn. J. Appl. Phys.* **2004**, 43, 8354.

[4] J.W. Elam, D. Routkevitch, P.P. Mardilovich, S.M. George, *Chem. Mater.* **2003**, 15, 3507.

[5] C.A. Huber, T.E. Huber, M. Sadoqi, J.A. Lubin, S. Manalis, C.B. Prater, *Science* **1994**, 26, 800.

[6] A.B.F. Martinson, J.W. Elam, J. Liu, M.J. Pellin, T.J. Marks, J.T. Hupp, *Nano Lett.* **2008**, 8, 2862.

[7] J.H. Chen, C.G. Chao, J.C. Ou, T.F. Liu, *Surface Science* **2007**, 601, 5142.

[8] J.H. Chen, S.C. Lo, C.G. Chao, T.F. Liu, *J. Nanosci. Nanotechnol.* **2008**, 8, 967.

[9] S.H. Chen, C.C. Chen, Z.P. Luo, C.G. Chao, *Mater. Lett.* **2009**, 63, 1165.

[10] S.H Chen, C.C. Chen, C.G. Chao, *J. Alloys Compd.* **2009**, 481, 270.

[11] C.C. Chen, Y. Bisrat, Z.P. Luo, R.E. Schaak, C.G. Chao, D.C. Lagoudas, *Nanotechnology* **2006**, 17, 367.

[12] C.C. Chen, C.G. Kuo, C.G. Chao, *Jpn. J. Appl. Phys.* **2005**, 44, 1524.

[13] X. Duan, Y. Huang, Y. Gui, J. Wang, C.M. Lieber, *Nature* **2001**, 409, 66.

[14] H. Pettersson, L. Bååth, N. Carlsson, W. Seifert, L. Samuelson, *Appl. Phys. Lett.* **2001**, 79, 78.

[15] J.C. Johnson, H. Yan, R.D Schaller, P.B. Petersen, P. Yang, R.J. Saykally, *Nano Lett.* **2002**, 2, 279.

[16] W. Kurz, D.J. Fisher, "*Fundamentals of Solidification*", Trans Tech Publication, Aedermannsdorf, Switzerland, **1992**.

[17] K.A. Jackson, J.D. Hunt, *Trans. Met. Soc. AIME* **1996**, 236, 1129.

[18] J. D. Hunt, *Science and Technology of Advanced Materials* **2001**, 2, 147.

[19] Y. Bisrat, Z.P. Luo, D. Davis, D. Lagoudas, *Nanotechnology* **2007**, 18, 395601.

[20] N.W. Gong, M.Y. Lu, C.Y. Wang, Y. Chen, L.J. Chen, *Appl. Phys. Lett.* **2008**, 92, 073101.

[21] C.Y. Wang, M.Y. Lu, H.C. Chen, L.J. Chen, *J. Phys. Chem. C* **2007**, 111, 6215.

[22] C.Y. Wang, N.W. Gong, L.J. Chen, *Adv. Mater.* **2008**, 20, 4789.

[23] B.R. Munson, D.F. Young, T.H. Okiishi, "*Fundamentals of Fluid Mechanics*", 3rd edition, New York **2003**.

[24] J.H. Chen, S.C. Lo, C.G. Chao, T.F. Liu, *Jpn. J. Appl. Phys.* **2008**, 47, 4815.

[25] B. Isecke, J. Osterwald, *Z. Phys. Chem. NF* **1979**, 115, 17.

[26] D. Risold, B. Hallstedt, L.J. Gauckler, H.L. Lukas, S.G. Fries, *J. Phase Equilibria* **1995**, 16, 223.

[27] A. Grigoriev, O. Shpyrko, C. Steimer, P.S. Pershan, B.M. Ocko, M. Deutsch, B. Lin, M. Meron, T. Graber, J. Gebhardt, *Surface Science* **2005**, 575, 223.

[28] Landolt-Börnstein, "*Binary systems. Part 2: Elements and Binary Systems from B – C to Cr – Zr Phase Diagrams, Phase Transition Data, Integral and Partial Quantities of Alloys"*, Springer Berlin Heidelberg **2004**.

[29] Metallurgy Division, *National Institute of Standards and Technology* (http://www.metallurgy.nist.gov/phase/solder/bisn.html).

[30] B. Chalmers, "*Principles of Solidification"*, John Wiley & Sons Inc., New York **1964**.

[31] G. Tammann, "*Text Book of Metallography"*, Chemical Catalogue Co., New York **1925**.

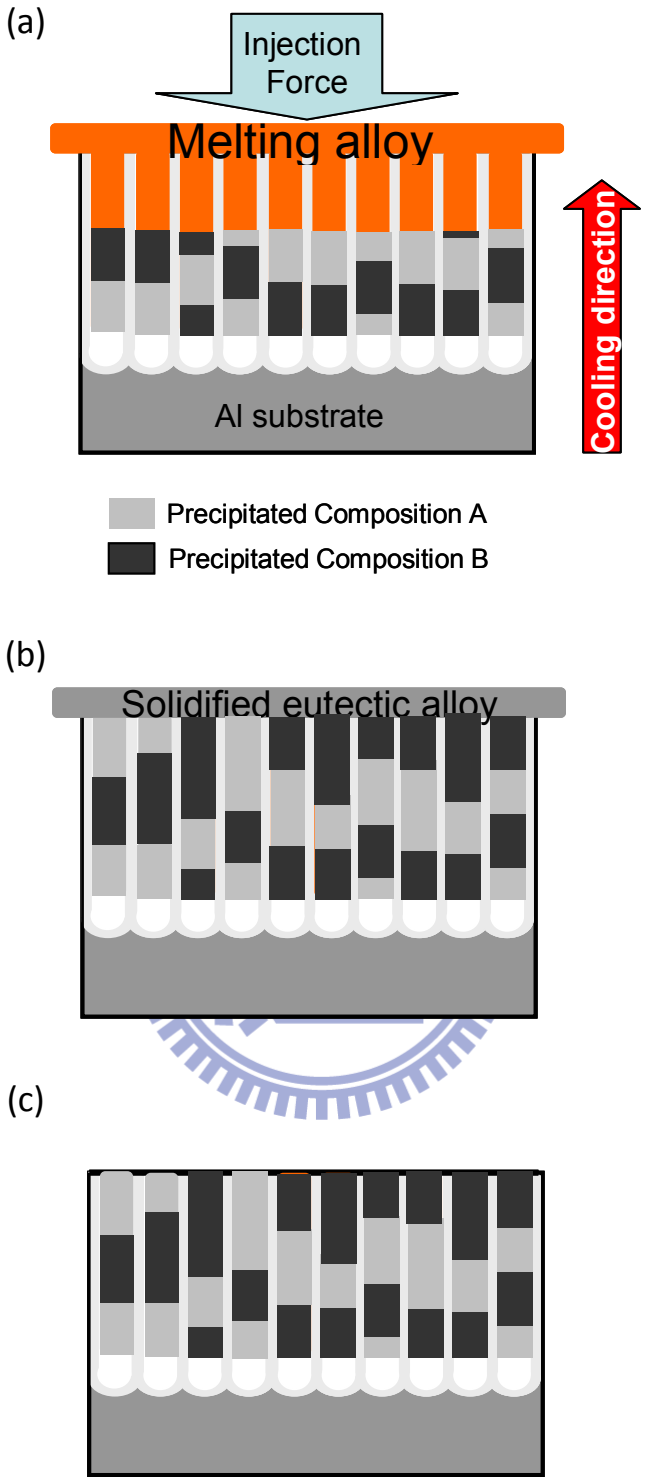

Figure 5.1 Schematic illustration of the solidification processes during the vacuum hydraulic pressure process within AAO membrane: (a) injection of the melted alloy into AAO membrane under steady pressure, (b) complete solidification of the nano-materials, (c) removal the residual alloy.

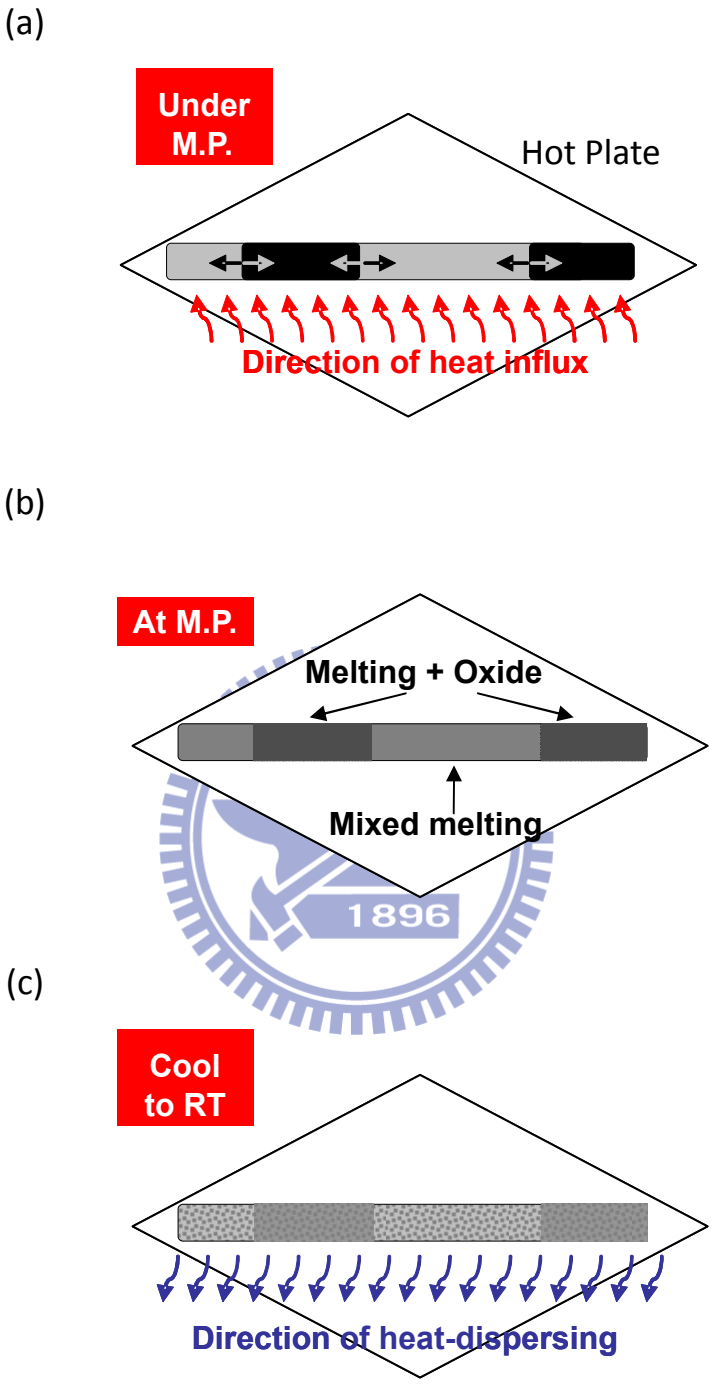

Figure 5.2 Schematic illustrations of the (a) heating, (b) holding and (c) cooling processes of a 70 nm nanowires within the in situ reheating setup.

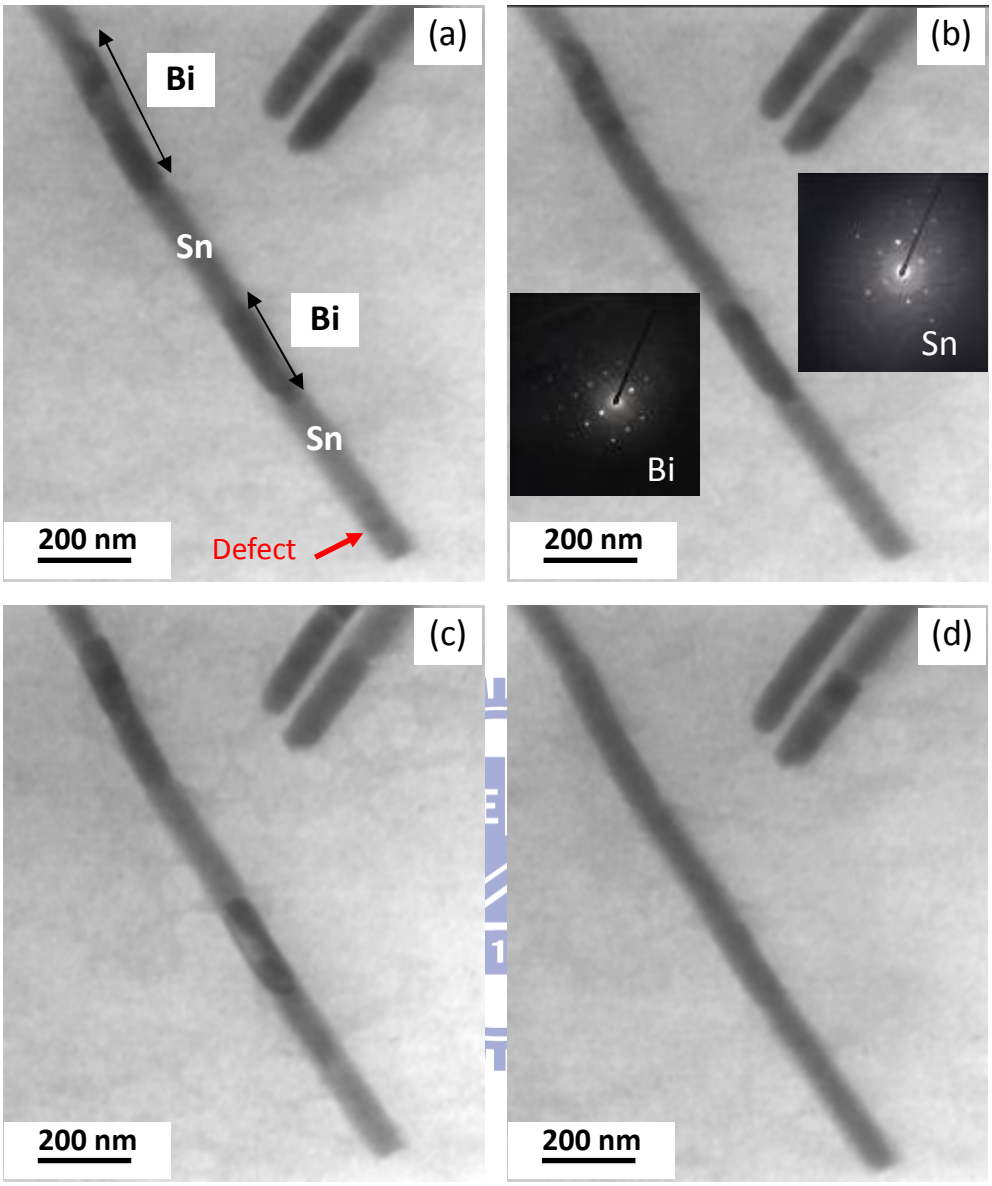

Figure 5.3 *In situ* TEM image sequences of the diffusion behavior during the reheating process within 70 nm eutectic Bi-Sn nanowires at (a) room temperature, (b) 80 ℃, (c) 138 ℃, (d) 150 ℃. The bright area is Sn, and the dark area is Bi, and the insets in (b) show the selective area electron diffraction pattern of Bi and Sn segments. The heating rate is 50℃/min.

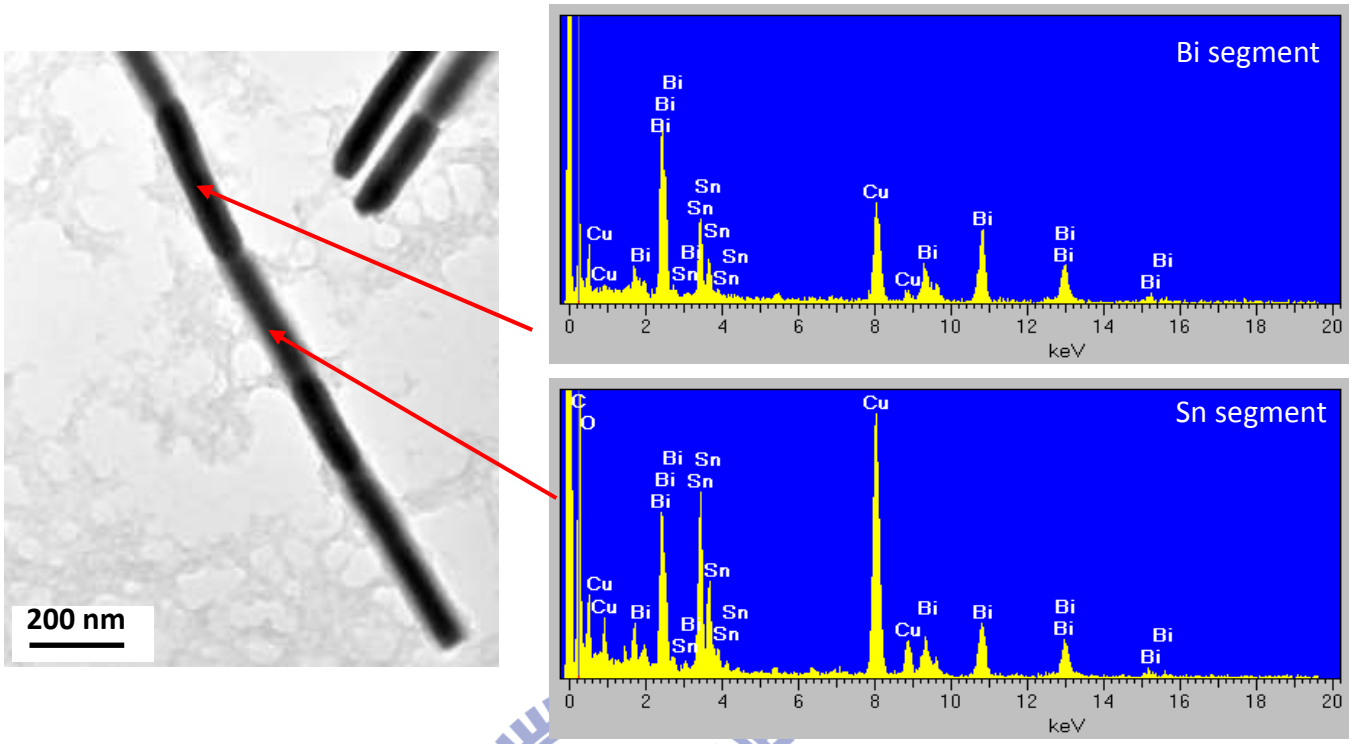

Figure 5.4 The fine TEM image of 70 nm eutectic Bi-Sn nanowire at 150 ℃ and the EDS spectrums from two distinct segments.

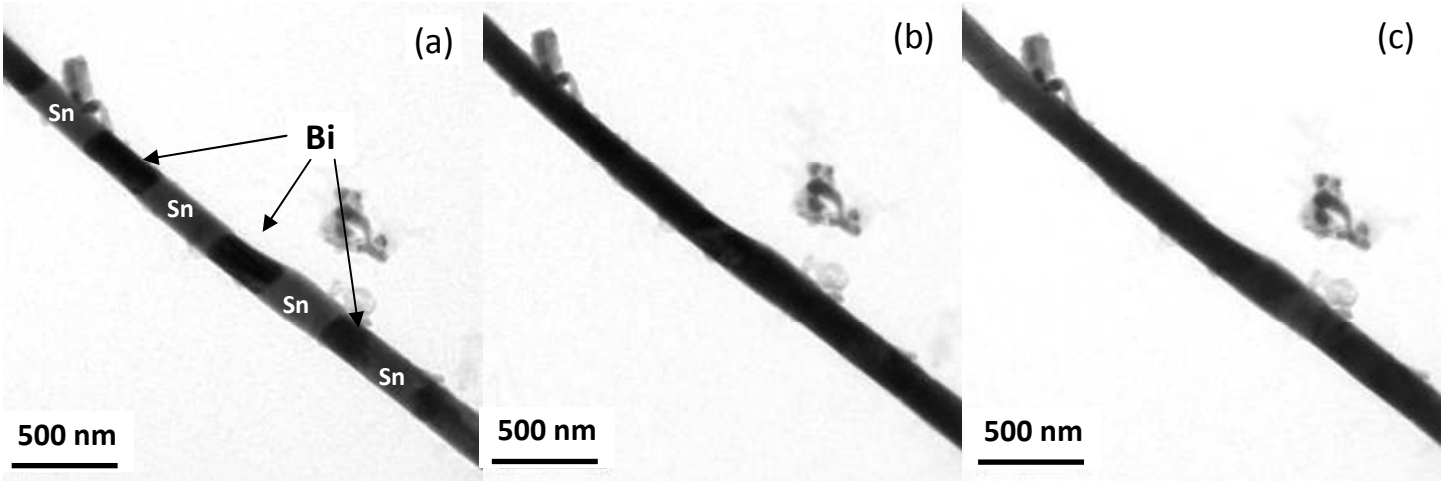

Figure 5.5 *In situ* TEM image sequences of a 200 nm eutectic Bi-Sn nanowire at (a) room temperature, (b) 138 ℃, (d) 150 ℃. The bright area is Sn, and the dark area is Bi. The heating rate is 50℃/min.

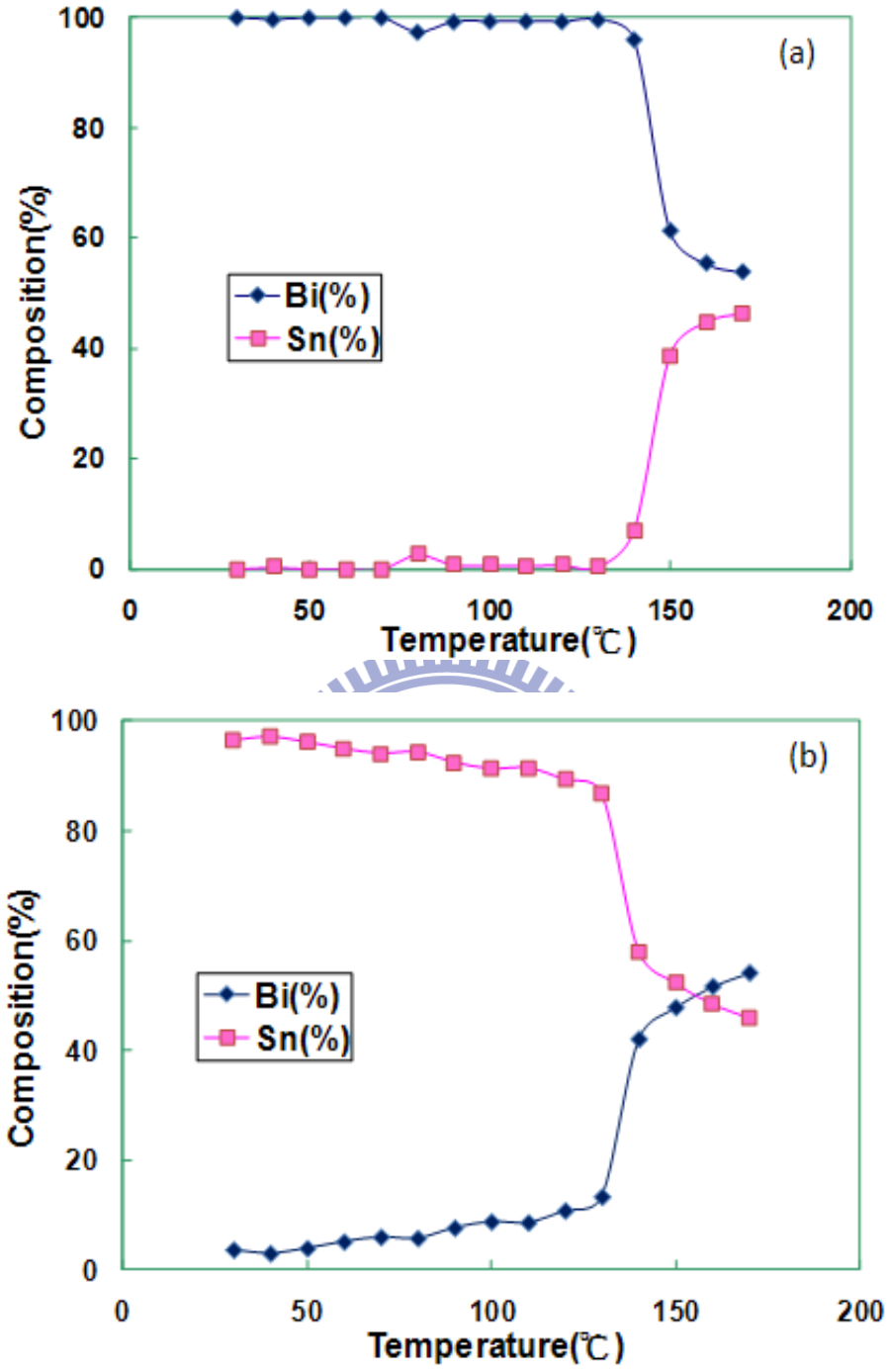

Figure 5.6 Relationship between compositions and temperatures for the individual (a) Bi and (b) Sn segments inside nanowires of both 70 nm and 200 nm during the reheating process.

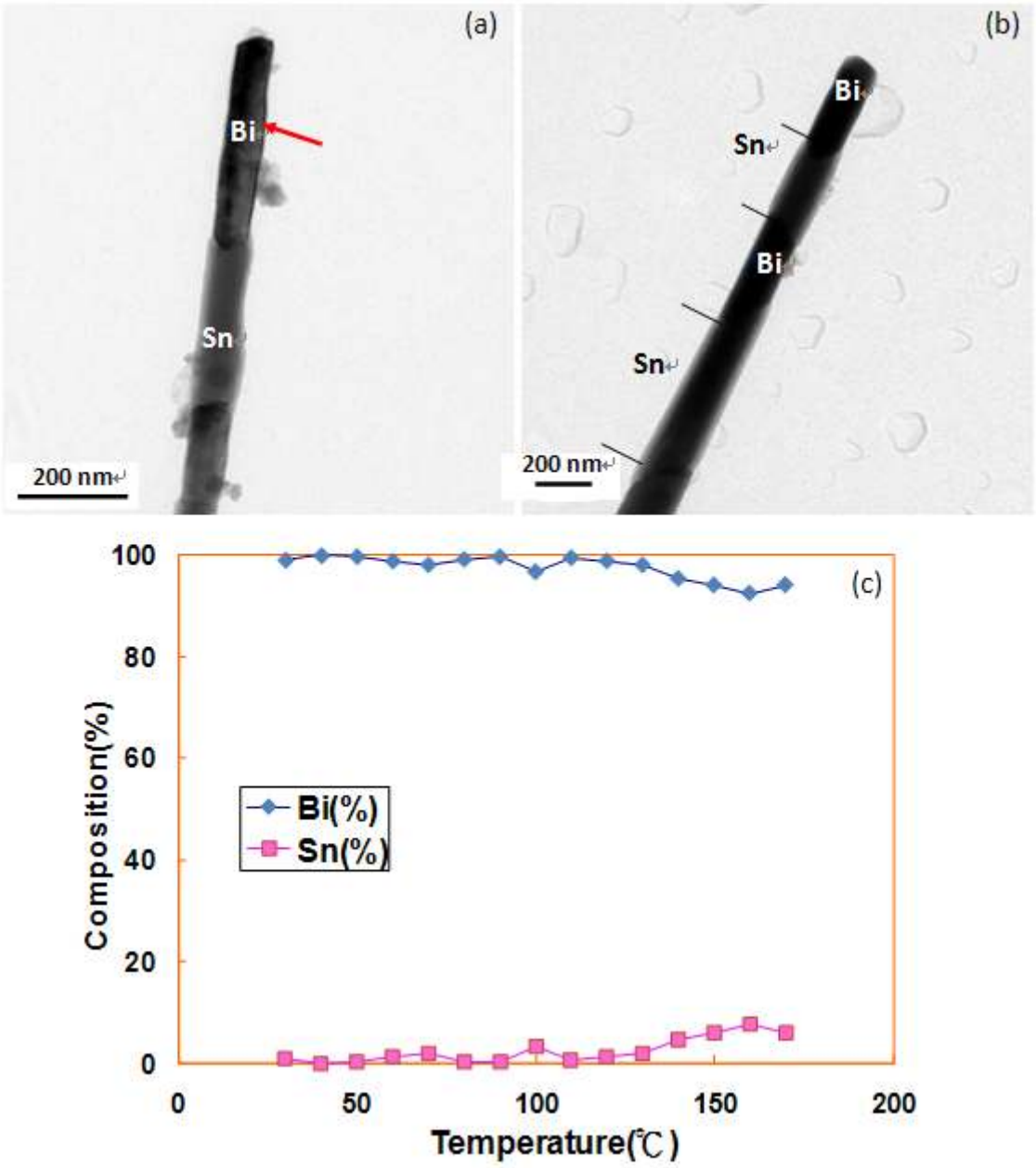
(a)
Bi
Sn
200 nm
(b)
Bi
Sn
Bi
Sn
200 nm
(c)
Composition(%)
Bi(%)
Sn(%)
Temperature(℃)
0
20
40
60
80
100
0
50
100
150
200

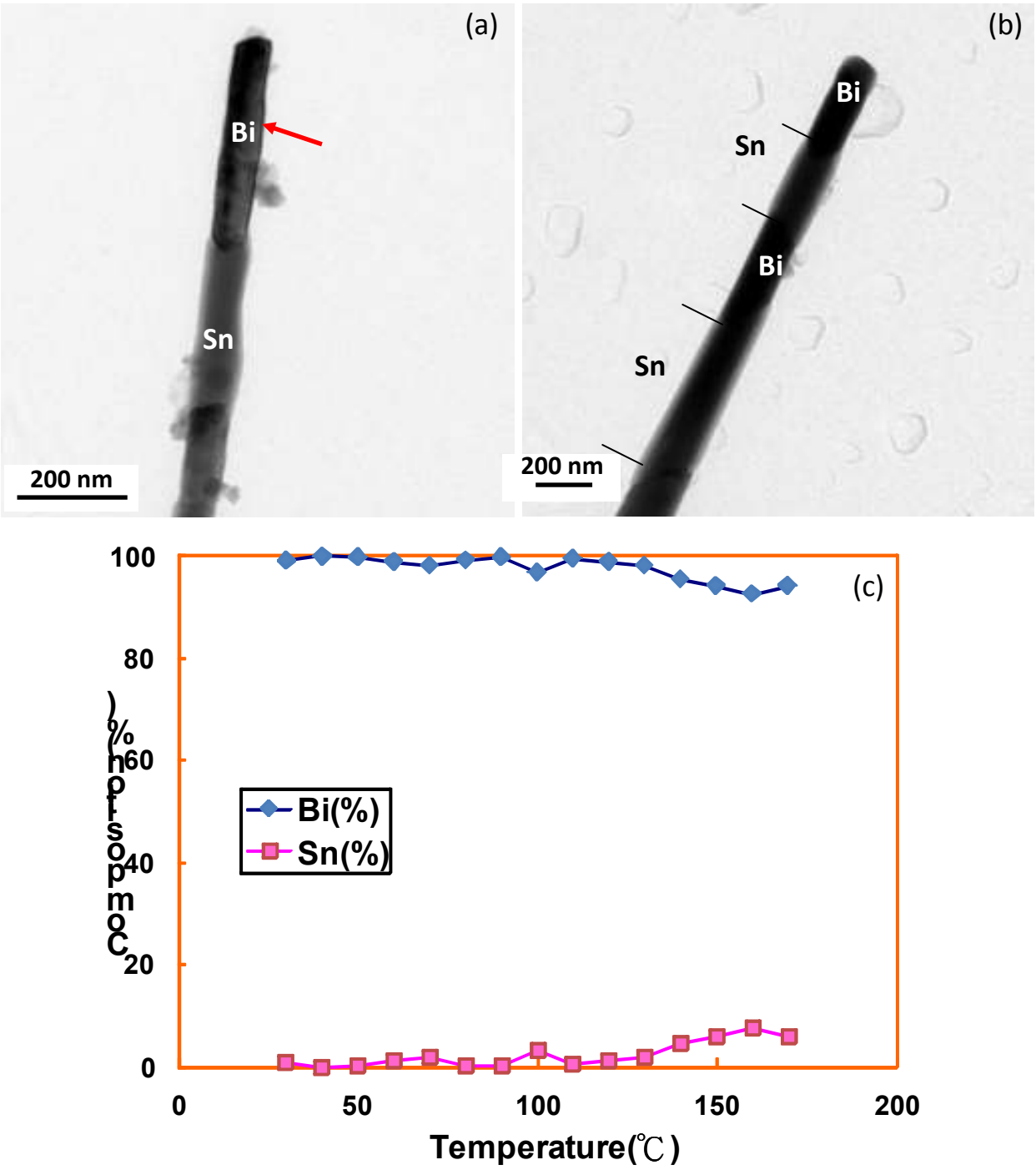

Figure 5.7 TEM images of the end tip of an individual Bi-Sn nanowire with average diameters of (a) 70 nm and (b) 200 nm. (c) Relationship between compositions and temperatures taken from the arrowed position in (a).

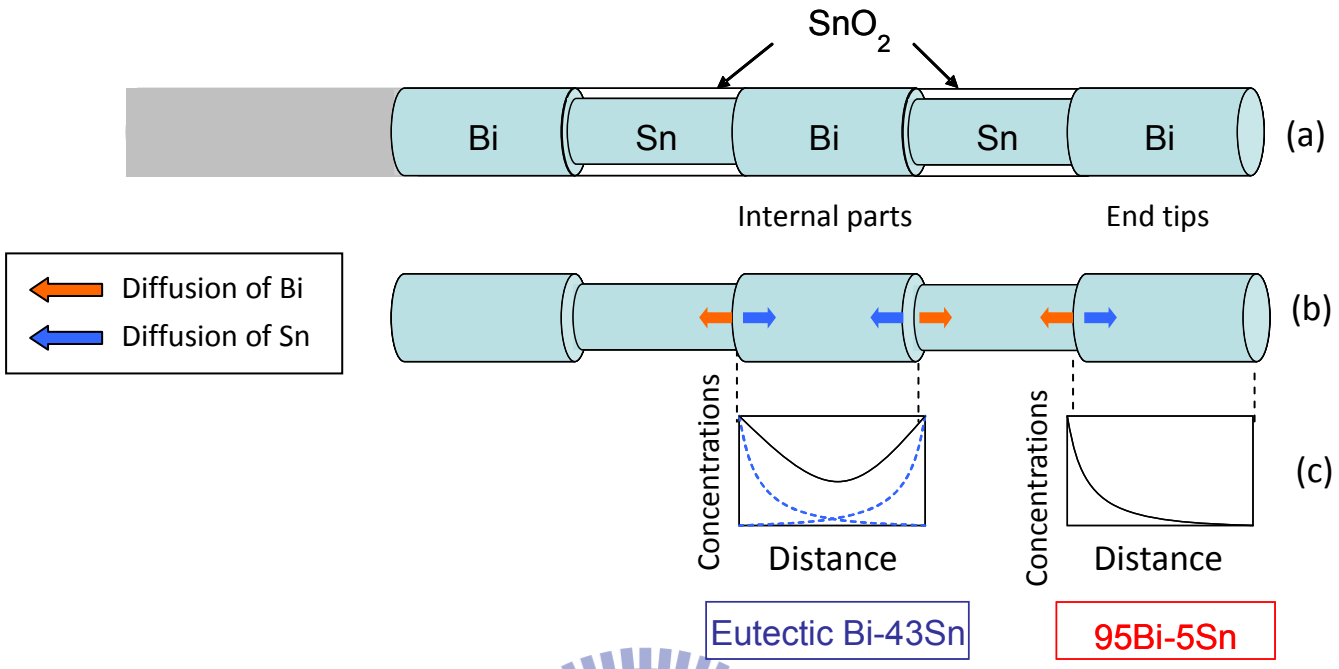

Figure 5.8 Schematic illustrations of the diffusion behaviors in different positions within a single eutectic Bi-Sn nanowire of 70 nm. From top, they present (a) the sketch of a single wire, (b) the diffusion directions within each segment, and (c) the concentration profiles along the wire axis (in weight percentage).

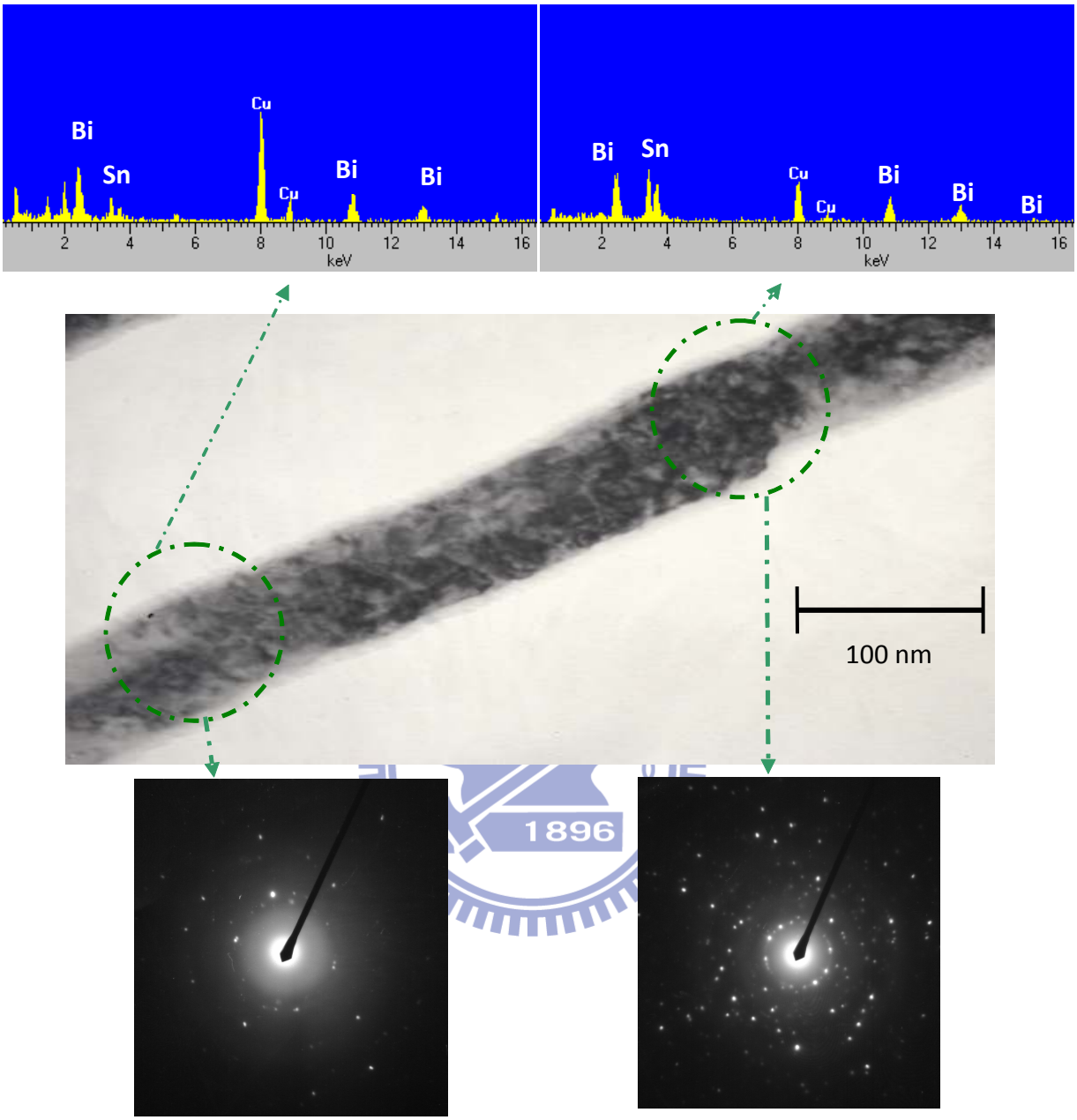

Figure 5.9 TEM image, EDS spectrum, and SAED patterns of a 70 nm Sn-Bi eutectic nanowire with polycrystalline microstructure after *in situ* reheating.

Table 5.1 Experimental heating conditions and the results of compositions for eutectic Bi-Sn nanowires.

	70 nm NWs				200 nm NWs			
	Bi segment		Sn segment		Bi segment		Sn segment	
(wt-%)	Bi	Sn	Bi	Sn	Bi	Sn	Bi	Sn
R.T. → 70℃	98.2	1.8	4.0	96.0	99.3	0.7	8.7	91.3
R.T. → 170℃	94.2	5.8	40.1	59.9	61.3	38.7	54.1	45.9
170℃ → R.T.	94.1	5.9	34.3	65.7	98.7	1.3	10.5	89.5

PART III: Application –

Chapter 6 Fabrication of Bi_2O_3-SnO_2 nanowires by the direct thermal oxidation of Bi-Sn eutectic nanowires

6.1 Background and Motivation

Functional metal oxides have unique physical properties, which are valuable in many applications. Among them, tin oxide (SnO_2) and bismuth oxide (Bi_2O_3) are two important strategic materials of use in modern solid-state technology. As semiconductors with large and wide energy band gaps, they are extensively applied in gas sensors [1, 2], optoelectronic devices [3, 4], photovoltaic cells [5, 6], and transparent conduction electrodes [7]. However, the dimensions of these materials affect the chemical and physical properties of these materials. One-dimensional materials, such as nanowires, nanorods and nanotubes, are very useful in both fundamental and applied research.

Because of the scientific and technological importance of SnO_2 and Bi_2O_3, many studies have been published on the synthesis of one-dimensional nanostructures of these compounds. Chemical vapor deposition (CVD) [8, 9], chemical method [10, 11], laser ablation [12], and thermal evaporation [13] are common bottom-up approaches for preparing one-dimensional self-assembly materials. However, a simpler, cheaper, and more stable process for industrial applications is urgently sought.

This chapter describes the fabrication of BiO_x-SnO_x nanowires by directly oxidizing Bi-Sn eutectic nanowires in an air furnace. The Bi-Sn eutectic nanowires have a segmental microstructure, and are synthesized by a template-assisted casting process [14]. As-injected nanowires have a regular structure; thus, the BiO_x-SnO_x nanowires are obtained by a thermal

oxidation process to retain their segmental microstructure. The optical properties are evaluated to derive evidence of the existence of both oxides.

6.2 Experimental Procedures

The segmental Bi-Sn eutectic nanowires were synthesized using the vacuum hydraulic pressure injection process [14]; the as-injected nanowires had an average diameter of 70 nm and lengths of several microns. Details of the injection process have been presented elsewhere [15, 16].The prepared materials were put into an air furnace and directly annealed at 700 ℃ for 1 hour. After cooling to room temperature, the BiO_x-SnO_x nanowires were obtained.

The morphology and appearance of metal and oxide nanowires were characterized by field-emission scanning electron microscope (FESEM, JSM-6500) and transmission electron microscope (TEM, JEM-2010) that was combined with energy-dispersive X-ray spectrometry (EDS).

Oxide nanowires were spectroscopically analyzed using SEM-cathodoluminescence (CL) at room temperature with a commercial Gatan MonoCL2 system and an alkali halide photomultiplier detector, attached to the SEM. To determine the photocurrent, an ultraviolet (UV) lamp (λ=325 nm) was used as a light source; the power density of the light was 10 mW/cm^2. The photocurrent was measured using a two-probe I-V system with a Keithley 237 source measurement unit.

6.3 Results and Discussion

The nanostructure materials that were synthesized by this injection process formed an oxide shell upon the removal of AAO template. This spontaneous oxide shell was stable and served as a container to preserve the alloys inside during the annealing process [17]. To prevent the formation of a metastable phase, the annealing temperature must be no higher than

729 ℃ [18], but was set to 700 ℃.

Figure 6.1(a) shows an SEM image of as-injected Bi-Sn nanowires after the AAO template was removed using the etching solution (0.4 M H_3PO_4 + 0.2 M CrO_3) at 60 ℃ for 2 h, and washing with ethanol and deionized water. A thin oxide layer was observed on the products. These spontaneous oxides formed a core-shell structure and enclosed the alloys within the nanowires for the next annealing treatment. However, the initial oxides were not dense enough for rapid expansion of liquid alloys. If the heating rate would have exceeded 100 ℃/ min, the alloys would not have converted to oxides within the shell and would have leaked out. In Fig. 6.1(b), the SEM image shows the residual oxide shells after annealing at an excessive heating rate. Liquid alloys escaped from the fragile locations, defects or interfaces, and so the shell had a broken segmental structure.

Figure 6.2 shows TEM images of annealed nanowires at the excessive and proper annealing conditions respectively. In Fig. 6.2(a), most alloys leaked out, and only fractured oxide nanowires remained after the annealing process at an excessive rate. Some complete segmental oxide nanowires were nevertheless found. This was due to the remaining AAO, which served as dense oxide shells of Bi-Sn nanowires and restrained the alloys from leaking. When the heating rate was reduced to a proper value of 50℃/ min, the morphology of the oxide nanowires was that of solid rods with a segmental structure, as shown in Fig. 6.2(b). The differences between the segments originally resulted from the sequential precipitation of bismuth and tin. Accordingly, the morphology of oxide nanowires followed the array of Bi-Sn eutectic nanowires.

When Bi-Sn eutectic nanowires were annealed at 700 ℃ for 1 h at a heating rate of 50 ℃/ min, one-dimensional nano-compounds of bismuth oxide and tin oxide were produced as straight wires. The TEM image in Fig. 6.3(a) shows that the morphology of well-annealed nanowires that retain the segmental structure. The compositions of nanowires were also determined by EDS analysis, as presented in Fig. 6.3(b). BiO_x-SnO_x nanowires were

successfully formed by annealing. The Mo and Ta peaks arose from the TEM grid and heating holder, respectively.

To ensure the species of oxide nanowires, an SEM-CL spectrum was obtained to elucidate the radiative property of the oxides at room temperature. In Fig. 6.4, the pulsating line, from 200 nm to 800 nm, represents the raw CL spectrum of oxide nanowires; its fitting curve is also shown. According to previous studies [8, 13, 19], the curve could be decomposed into two sub-curves. One is sharper than the other and ranges from 300 nm to 530 nm. Leonite [13] reported that the absorption curve of Bi-O system resulted mainly from the band gaps of α–Bi_2O_3 and Bi_2O_3 (E_g = 2.29-3.31 eV). The other sub-curve is consistent with the hypothesis that the transition is caused by deep levels in the band gap that associated with surface states, induced by oxygen vacancies of the SnO_2 nanowire, as elsewhere presented by the present authors [8, 19]. Therefore, the CL spectrum clarifies the species of oxides and supports the existence of BiO_x-SnO_x nanowires.

Figure 6.5 plots the photoresponse of BiO_x-SnO_x nanowires at a bias voltage of 0.8 V in air under modulated illumination by light with a wavelength of 325 nm. The photocurrent of the oxide nanowires increased rapidly when the light was switched on, and saturated. After the light was switched off, the current decayed to one-tenth of the saturated value within 300 s. This phenomenon indicates that the photoresponse of an n-type oxide semiconductor is controlled by surface effects, such as oxygen absorption by trapping electrons ($O^2_{(g)} + e^- = O_2^-{}_{(ad)}$) under dark conditions and the photodesorption of oxygen ions by the capture of photogenerated holes ($h^+ + O_2^-{}_{(ad)} = O_{2(g)}$) [20, 21]. Recent studies [22, 23] have also focused on such functional oxides; and identified them with this optical mechanism.

6.4 Summary

This work demonstrates that compound nanowires of bismuth oxide and tin oxide were

generated by directly annealing Bi-Sn eutectic nanowires, synthesized by vacuum hydraulic pressure injection. The well-annealed oxide nanowires were straight and solid, and retained their segmental structure. CL spectrum and photoresponse analyses confirmed that the oxides were BiO_x-SnO_x nanowires. This fabrication methodology is a simple means of forming one-dimensional oxide nanomaterials.

References

[1] A. Khanna, R. Kumar, S.S. Bhatti, *Appl. Phys. Lett.* **2003**, 82, 4388.

[2] E. Kanazawa, G. Sakai, K. Shimanoe, Y. Kanmura, Y. Teraoka, N. Miura, N. Yamazoe, *Sensors Actuators B* **2001**, 77, 72.

[3] C. Tatsuyama, S. Ichimura, *Jpn. J. Appl. Phys.* **1976**, 15, 843.

[4] L. Leontie, M. Caraman, A. Visinoiu, G.I. Rusu, *Thin Solid Films* **2005**, 473, 230.

[5] M. Turrion, J. Bisquert, P. Salvador, *J. Phys. Chem. B* **2003**, 107, 9397.

[6] J. George, B. Pradeep, K.S. Joseph, *Phys. Stat. Sol. (a)* **1987**, 100, 513.

[7] Y.S. He, J.C. Campbell, R.C. Murphy, M.F. Arendt, J.S. Swinnea, *J. Mater. Res.* **1993**, 8, 3131.

[8] D. Calestani, M. Zha, A. Zappettini, L. Lazzarini, G. Salviati, L. Zanotti, G. Sberveglieri, *Mater. Sci. Eng. C* **2005**, 25, 625.

[9] H.W. Kim, J.H. Myung, S.H. Shim, *Solid State Commun.* **2006**, 137, 196.

[10] T.P. Gujar, V.R. Shinde, C.D. Lokhande, S.H. Han, *Mater. Sci. Eng. B* **2006**, 133, 177.

[11] A. Kolmakov, Y. Zhang, G. Cheng, M. Moskovits, *Adv. Mater.* **2003**, 15, 997.

[12] Z. Liu, D. Zhang, S. Han, C. Li, T. Tang, W. Jin, X. Liu, B. Lei, C. Zhou, *Adv. Mater.* **2003**, 15, 1754.

[13] L. Leontie, M. Caraman, M. Alexe, C. Harnagea, *Surf. Sci.* **2002**, 507-10, 480.

[14] S.H. Chen, C.C. Chen, Z.P. Luo, C.G. Chao, *Mater. Lett.* **2009**, 63, 1165.

[15] C.C. Chen, C.G. Kuo, J.H Chen, C.G. Chao, *Jpn. J. Appl. Phys.* **2004**, 43, 8354.

[16] S.H. Chen, C.Y. Wang, L.J. Chen, T.F. Liu, C.G. Chao, *J. Nanosci. Nanotechnol.* **2010**, 10, 1.

[17] A. Kolmakov, Y. Zhang, M. Moskovits, *Nano Lett.* **2003**, 3, 1125.

[18] L. Li, Y.W. Yang, G.H. Li, L.D. Zhang, *Small* **2006**, 2, 548.

[19] J.D. Prades, J. Arbiol, A. Cirera, J.R. Morante, M. Avella, L. Zanotti, E. Comoni, G. Faglia, G. Sberveglieri, *Sensors Actuators B* **2007**, 126, 6.

[20] D.A. Melnick, *J. Chem. Phys.* **1957**, 26, 1136.

[21] R. Keezer, *J. Appl. Phys.* **1961**, 35, 1866.

[22] J.S. Lee, S.K. Sim, B. Min, K. Cho, S.W. Kim, S. Kim. *J. Cryst. Growth.* **2004**, 267, 145.

[23] Y. Wang, I. Ramos, J.J. Santiago-Aviles, *J. Appl. Phys.* **2007**, 102, 093517.

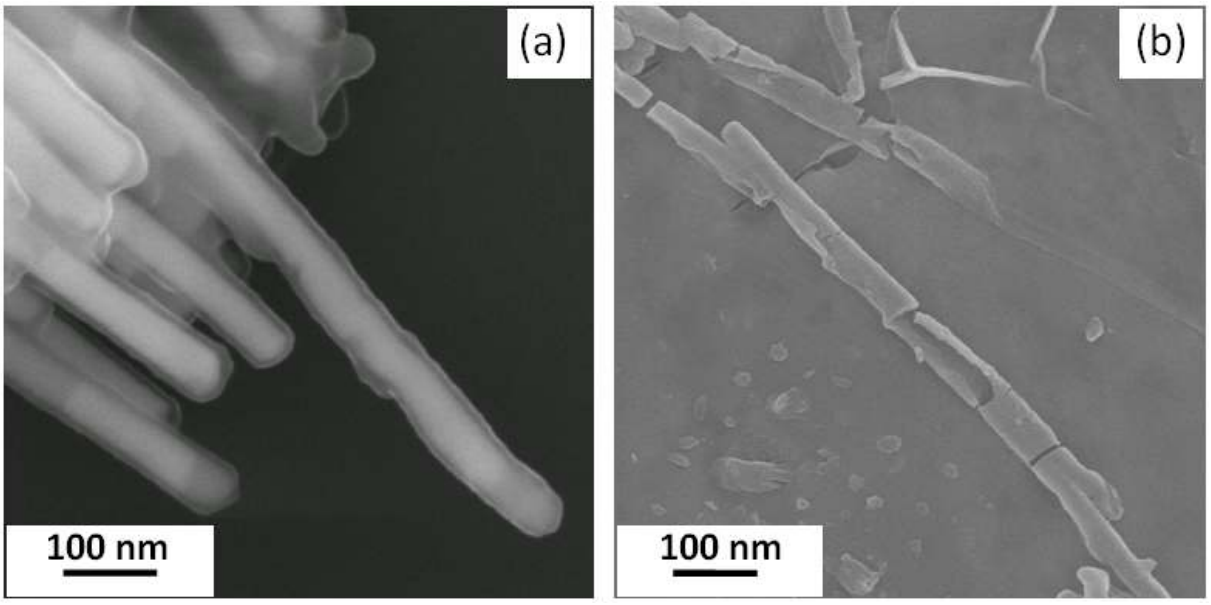

Figure 6.1 (a) SEM image of as-injected Bi-Sn eutectic nanowires after removal of AAO template with etching solution. The core-shell of the segmental structure was observed. (b) SEM image of nanowires annealed at an excessive heating rate.

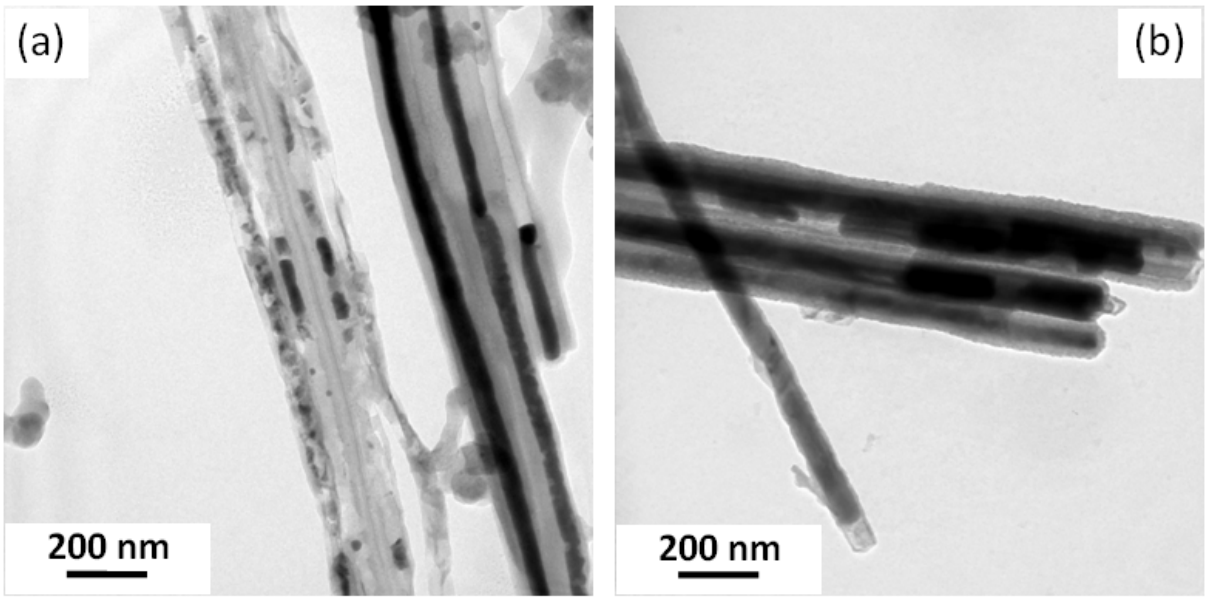

Figure 6.2 TEM images of Bi-Sn eutectic nanowires annealed at (a) an excessive and (b) the proper heating rates. The oxides were not dense enough to confine the melting alloys when the heating rate was excessive; proper annealing conditions resulted in stiff and complete nanowires. Residual AAO helped to maintain the integrity of the molten alloys.

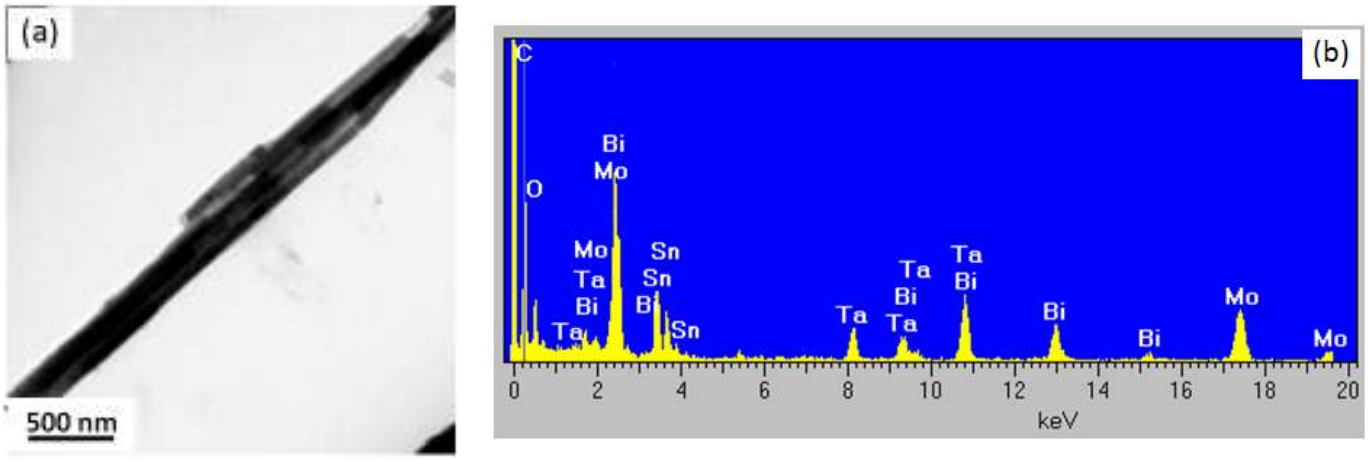

Figure 6.3 (a) TEM image of well-annealed Bi-Sn eutectic nanowires. (b) EDS was used to determine the composition of nanowires. Mo and Ta peaks arose from TEM grid and heating holder, respectively.

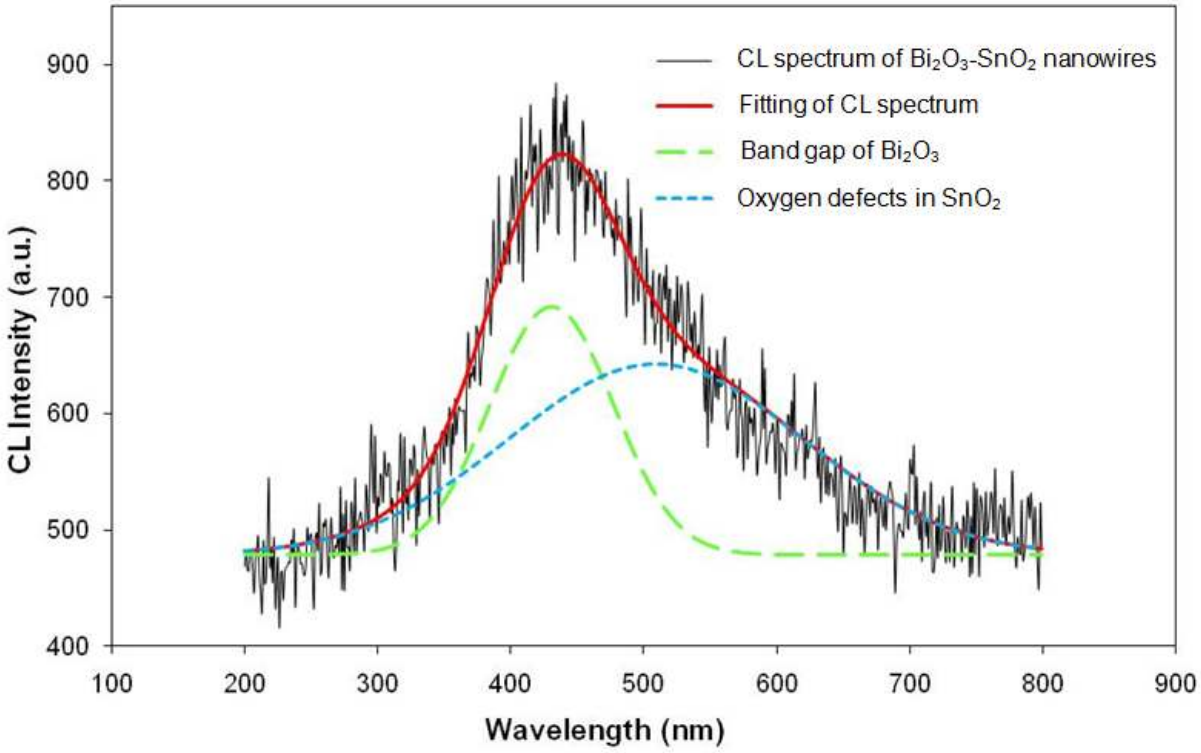

Figure 6.4 CL spectrum of BiO_x-SnO_x nanowires with an average diameter of 70 nm. The curve comprised two emissions - band gap of Bi_2O_3 and oxygen vacancies in SnO_2 [8, 13, 19].

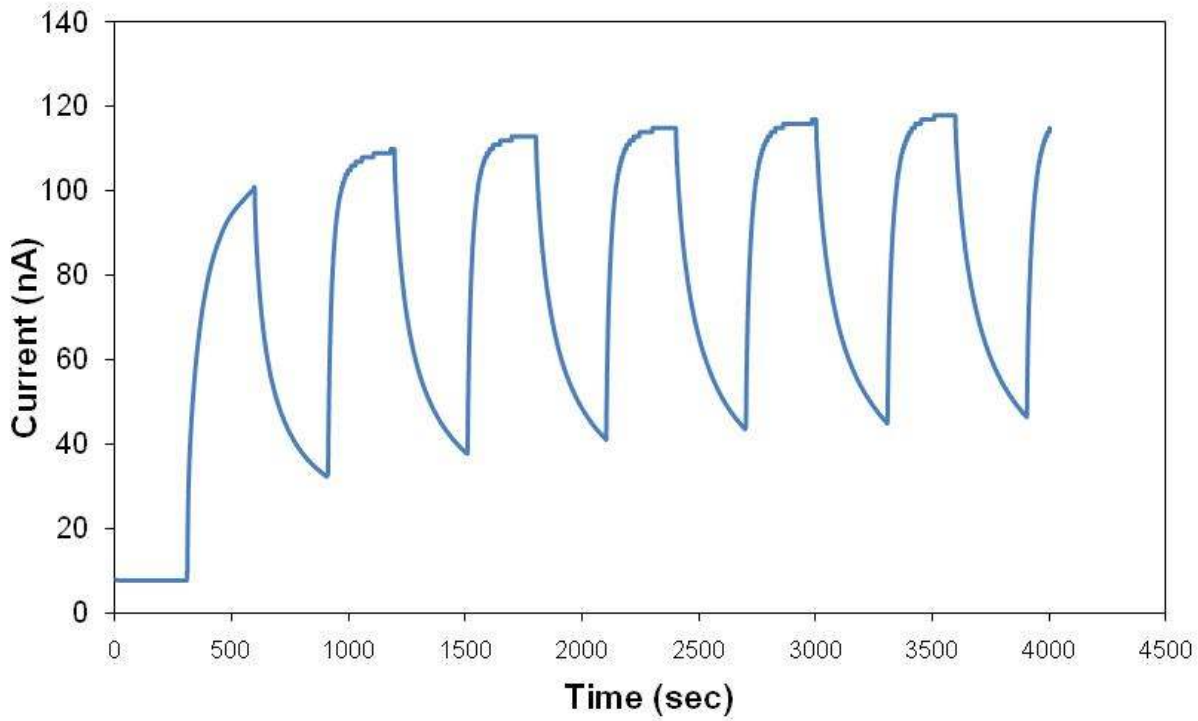

Figure 6.5 Photoresponse of Bi_2O_3-SnO_2 nanotubes with periodic irradiation at 325 nm in air at bias voltage of 0.8 V.

Chapter 7 Conclusions and Suggestions for Future work

7.1 Conclusions

The methodology, combining the characteristics of anodic template with the mold casting process, to one-dimensional nanowires was successfully addressed. Also, the solidification mechanism of its products was presented and well accepted. The details are concluded as bellow:

1. In chapter 3, attempts have been made to prepare nanowires using this Bi-43Sn alloy. The nanowires, with diameters of 20 nm, 70 nm and 220 nm respectively, were fabricated by a hydraulic pressure injection process using anodic aluminum oxide (AAO) as templates. The 20 nm AAO template, with 7 nm pore wall thickness and ~ 8×10^{11} pore · cm^{-2} density, was fabricated by using 10 vol-% sulfuric acid; and the 70 nm diameter AAO, with 20 nm pore wall thickness and ~ 3×10^{10} pore · cm^{-2} density, was fabricated by using 3 vol-% oxalic acid; and finally the 220 nm AAO, with 100 nm pore wall thickness and ~ 1×10^{9} pore · cm^{-2} density, was fabricated by using 1 vol-% phosphoric acid. The fabricated nanowires exhibited novel eutectic microstructure, which composed of alternating single Bi and Sn segments along their wire axes. Within the segments, the electron diffraction analysis revealed single crystalline structures of Bi and Sn elements respectively. Therefore, it was found that the as the wire diameter reduced, longer Bi and Sn segments formed.
2. In chapter 4, the Bi-Sn eutectic nanowires of 200 nm diameter and several tens of μm in length is taken as an example to describe why and how the segments sequentially precipitate. That the one-dimension nano-structure of the AAO template limited the

banded wire morphology to an arrangement along its axis might result from the alternate enrichments between bismuth and tin in the liquid phase. The distribution coefficient and lever rule were utilized to describe the approximately three-fold difference in length. Consequently, when the binary lamellar eutectic was trapped in a nano-scaled structure, the different solidification behavior and the enrichment alternations between hypereutectic and hypoeutectic would bring about this particular appearance.

3. In chapter 5, the size effects on solidification and the formation mechanism of the segmented eutectic Bi-43Sn nanowires during in situ annealing have been investigated. A directional solidification along the wire axis limits the segmented eutectic nanowire to arrange axially during the in situ annealing processes due to directional solidification. In 70 nm nanowires, the small size confines the convection in liquid, which results in differences in the microstructure and composition profiles between 70 and 200 nm nanowires. In the vacuum hydraulic pressure injection process, the directional cooling helps the formation of single crystal, and the isotropic solidification leads to polycrystalline microstructure.
4. In chapter 6, bismuth oxide-tin oxide (BiO_x-SnO_x) heterostructure nanowires with a diameter of 70 nm were fabricated by directly annealing Bi-Sn eutectic nanowires. After removal of AAO template with etching solution, a spontaneous oxide was formed on the nanowires, enclosing the Bi-Sn eutectic alloys. While these nanowires went through the annealing process at a heating rate of 50 ℃/ min, the well-annealed oxide nanowires remained solid, straight and segmental. The results of cathodoluminescence (CL) spectrum and photoresponse proved that the products comprised bismuth oxide and tin oxide. This fabrication methodology is a simple way to fabricate one-dimensional oxide nanomaterials.

7.2 Suggestions for Future Work

Generally, this fabrication approach, like a traditional mold casting, can be utilized to synthesize nanowires of most meltable metals and alloys, but the aluminum bottom limits its usage to only 660 ℃. In addition, most functional metals or alloys have a high melting point. If the temperature is higher than 660 ℃, the AAO template will float onto the melting alloys and not be injected with liquid materials correctly. Therefore, the application of this process is restricted.

In order to develop this method, a topic, substituting the supporting aluminum with metals of a high melting point, is under way. Changing the aluminum substrate with copper or nickel enhances this template-assisted injection process to around 1000℃. Lately, a substitution experiment was successfully achieved in our laboratory. Some functional alloys, such as Bi-Te-Sb system (585 ℃), Cu-Ge system (644 ℃), and Ag-Ge system (651 ℃), were put in practice as well. The preliminary results show that the high-temperature applications are workable. Consequently, the following works are suggested undertaking the substrate-substitution approach for the synthesis of high-temperature functional nanowires.

學經歷資料表

姓名：陳士勛　　**生日**：西元 1979 年 6 月 9 日

性別：男　　**籍貫**：台灣省南投縣

住址：高雄市三民區建興路 99 巷 28 號

學經歷：

高雄市立正興國民小學

高雄市立民族國民中學

高雄市立高雄高級中學
1994 年 9 月 ～ 1997 年 6 月

國立清華大學工程與系統科學系
1997 年 9 月 ～ 2001 年 6 月

國立交通大學材料學與工程研究所(碩士班)
2001 年 9 月～ 2003 年 6 月

國立交通大學材料學與工程研究所(博士班)
2004 年 9 月～ 2010 年 8 月

博士論文題目：

錫鉍共晶奈米線材之製備、生成機制與應用

Fabrication, Solidification Mechanism and Application of Eutectic Bi-Sn Nanowires